Metal Particles on Thin MgO Films: Morphological and Optical Properties

vorgelegt von
Diplom Physiker
Philipp Myrach
aus Greifswald

Von der Fakultät II - Mathematik und Naturwissenschaften
der Technischen Universität Berlin
zur Erlangung des akademischen Grades
Doktor der Naturwissenschaften
Dr. rer. nat.

genehmigte Dissertation

Promotionsausschuss:

Vorsitzender:	Prof. Dr. Michael Lehmann
Gutachter:	Prof. Dr. Hans-Joachim Freund
Gutachter:	Prof. Dr. Mario Dähne
Gutachter:	Prof. Dr. Thomas Risse

Tag der wissenschaftlichen Aussprache: 30.11.2010

Berlin 2011
D83

Diese Dissertation wurde vom Oktober 2006 bis November 2010 in der Abteilung Chemische Physik am Fritz-Haber-Institut der Max-Planck-Gesellschaft unter der Anleitung von Herrn Professor Dr. Hans-Joachim Freund angefertigt.

Abstract

Metal Particles on thin oxide films are a well established model system in heterogeneous catalysis and promising candidates for photo-catalytic applications. Since usual industrial catalysts are complex and the working conditions prohibit the application of most surface science techniques, investigations focus on well defined model systems in controlled environmental conditions in order to gain a detailed understanding of the fundamental catalytic processes. In particular Scanning Tunneling Microscopy allows investigation with high spatial resolution. According to photo-catalytic applications it is necessary to extract the optical properties of these systems, that can be done by usual optical methods. Since these techniques average over a large surface area it is however not possible to directly draw correlations between the specific particle properties and the respective optical response. This drawback is counteracted in this work by the use of a Photon Emission Scanning Tunneling Microscope, which allows to probe the optical properties on a local scale.

By this means, the growth behavior and the optical properties of Mg, Ca, Ni, Au and Ag on thin MgO films on Mo(001) was studied systematically. Hereby it turned out, that the observed particle shapes and orientations can be explained by expanding the Young-Duprè approach to account for the tendency of the metal atoms to occupy the MgO oxygen sites and the lattice distortions, that are connected with the lattice mismatch between metal and substrate. Considering both contributions allowed to rationalize the observed growth behavior for all metal particles with the exception of Au. The optical properties of single metal particles were studies spectroscopically, as well as spatially resolved. Whereas the optical response is determined by exciton decay at higher bias, it is rationalized by the decay of metal particles plasmons, which are excited via inelastically tunneling electrons at lower bias values. The spatially resolved investigation revealed geometrical restrictions on the excitation of different plasmon modes and the development of so called "hot-spots" on the surface. In addition also the MgO substrate was characterized by means of PSTM, LEED and GIXD, leading to a comprehensive description of the relaxation mechanisms at the different thicknesses initiated by the lattice mismatch of 5.4% between MgO and Mo(001).

Furthermore the particle-substrate interactions can influence the physical and chemical properties of the metal particles. As a starting point for its investigation two approaches were established within this work. The preparation of other oxide films(CaO, Li_2O) and the lithium doping of MgO. Li-doped MgO hereby is of particular interest, since it is a potential catalyst for the oxidative coupling of methane and therefore represents a model system to unravel the underlaying reaction mechanisms.

Zusammenfassung

Metallpartikel auf dünnen Oxidoberflächen stellen etablierte Modellsysteme für die heterogene Katalyse und darüber hinaus aussichtsreiche Kandidaten für photokatalytische Anwendungen dar. Aufgrund der hohen Komplexität industrieller Katalysatoren und deren Betriebsbedingungen, welche eine oberflächenphysikalische Untersuchung häufig unmöglich machen, ist die Fokussierung auf definierte Modellsysteme in kontrollierten Umgebungen ein wichtiger Schritt um das Verständnis wichtiger katalytischer Prozesse zu ermöglichen. Vor allem die Raster Tunnel Mikroskopie erlaubt es hierbei Untersuchungen mit hoher räumlicher Auflösung durchzuführen. Insbesondere für Fragestellungen der Photokatalyse ist die Kenntnis der optischen Eigenschaften wichtig, wie sie mit einer Vielzahl optischer Methoden gewonnen werden können. Hierbei verbietet allerdings die Tatsache, dass diese Messungen über große Oberflächenbereiche mitteln, eine direkte Zuordnung von spezifischen Eigenschaften der Partikel mit dem optischen Verhalten. Diesem Umstand wird in dieser Arbeit Rechnung getragen, indem die optischen Untersuchungen mit Hilfe eines Photonen Emissions STM unternommen werden, welches die Untersuchung der optischen Eigenschaften auf lokaler Ebene erlaubt.

Dabei wurde das Wachstumsverhalten als auch die optischen Eigenschaften von Mg, Ca, Ni, Au und Ag auf MgO systematisch untersucht. Dabei zeigte sich, dass sowohl die Partikelform als auch deren Orientierung durch einen erweiterten Young Dupré Ansatz erklärt werden können, in welchem zum einen der Tendenz der Metallatome auf Sauerstoffplätzen zu binden und zu anderen die Deformierung des Gitters berücksichtigt wird. Eine solche Erweiterung ermöglicht es, dass beobachtete Wachstumsverhalten, mit Ausnahme von Gold, zu beschreiben. Die optischen Eigenschaften der Metallpartikel wurden spektroskopisch als auch räumlich aufgelöst untersucht. Lässt sich das optische Verhalten bei höheren Spannungen mit dem Zerfall von Exzitonen erklären, so ist bei niedrigeren Spannungen der Einfluss von zwei Beiträgen zu beobachten. In diesem Fall ist die Lichtemission zurückzuführen auf den Zerfall von Plasmonen in den Metallpartikeln und deren Anregung durch inelastische Tunnelprozesse, die auf spezifische, quantisierte Übergänge beschränkt sind. Die räumlich aufgelösten Untersuchungen machten geometrische Einschränkungen für die Anregung verschiedener Plasmonenmoden sichtbar und erlaubten außerdem die Beobachtung von sogenannten "Hot-Spots". Des Weiteren wurde das MgO Substrat mit Hilfe von STM, LEED und GIXD charakterisiert. Dabei ergab sich eine Beschreibung der verschiedenen Relaxationsmechanismen für unterschiedliche Schichtdicken, welche ihre Ursache in den unterschiedlichen Gitterkonstanten des MgO und des Mo(001) finden.

Die physikalischen und chemischen Eigenschaften von Metallpartikeln werden auch durch die Wechselwirkungen zwischen Partikel und Substrat beeinflusst. Für eine weitere Untersuchung solcher Beitrage, wurden in dieser Arbeit zwei Ansätze gewählt. Zum einen die Präparation von anderen Substraten(CaO, Li_2O) und zum anderen die Dotierung von MgO mit Lithium. Lithium dotiertes MgO ist dabei von besonderem Interesse, da es als potentieller Katalysator für die oxidative Kopplung von Methan diskutiert wird und deshalb als Modellsystem zur Klärung elementarer Reaktionsmechanismen dient.

Contents

Chapter 1

Introduction and Motivation

"More is different" is the title of an often quoted paper[1] by the 1977's Nobel laureate P. W. Anderson, where he discusses the emergent behavior of physical systems. The main statement is that some complex phenomena can not be understood only in terms of the laws governing their microscopic constituents. One of the most popular examples illustrating this, is the powerful concept of temperature, which is a physically precise value for macroscopic systems, but almost meaningless for atoms. Such scaling problems are in particular important in solid state physics, where the transition from elementary particles to solid bulk materials often leads to new physical and chemical properties and phenomena, which require other concepts for their description. Examples are superconductivity, magnetism, but also many processes in heterogeneous catalysis, which only occur in mesoscopic systems e.g. nano-particles, but not on bulk materials[2, 3, 4].

Besides very abrupt changes of the physical properties, also gradual changes can be found in solid state physics. The transition from an atom to a bulk material for instance involves changes of the electronic properties between the two limiting cases. This transition from sharp energy levels of the atom to the band-structure of the bulk metal leads to size dependent physical and chemical properties in metal particles[5]. This opens an interesting field of applications, since control of the particle dimensions in principle enables the tailoring of those electronic, optical and chemical properties within wide ranges.

For the optical properties this was used already in the middle age, where colored glasses were produced by the incorporation of small metal particles into silica matrices. The optical response of such particles is hereby governed by the excitation of the free electron gas in the metal. As shown by G. Mie[6] in 1908, the optical properties are hereby determined among other parameter, by the actual size and shape of the particle. Therefore the optical response can be varied over the entire visible spectral range by changes on the particle geometry. This tunability of the optical properties is not only important for optical, but might also have strong impact for photo-catalytic applications[7].The fact that metal particles crucially influence the catalytic performance in heterogeneous catalysis is known already for some decades. The underlying mechanisms for this activity are hereby often investigated on model systems, that simplify the very complex situation found in industrial catalysts[8, 9, 10, 11]. Such model system often consist of a thin, crystalline metal oxide film and metal particles deposited onto these surface. This approach allows a systematic characterization of the different constituents and its combination by well established surface science techniques[12]. The use of surface science techniques and in particular of Scanning Probe Microscopy allows to perform these investigations on an atomic level and under very controlled experimental conditions.

Within this work in particular a system consisting of a thin magnesium oxide film covered by number of different metal particles is studied. The MgO films are a commonly used model system to study processes related to heterogeneous catalysis[13, 14, 4]. MgO is a wide-gap insulator, which in principle restricts its optical activity to UV energies and therefore makes the material less important for photo-catalytic applications. However, the optical properties of the oxide can be strongly influenced by imperfections in the crystal lattice, as F-centers and low-coordinated sites[15, 16, 17], for instance. The optical properties of these sites are usually probed with non-local optical techniques, as diffuse reflectance spectroscopy or absorption measurements. These investigations always have to face the problem, that the detected optical response is obtained from a rather large area. That means, the optical response is an average over all different single species sites present on the surface. However, substantial differences can be expected depending on the actual defect-type, the geometric surrounding and interactions with other species, which can hardly be extracted from this averaged signal.

In order to analyze the correlation between these parameters and the local optical properties one has to probe the single species individually. Hereby light emission spectroscopy with a STM offers the possibility to locally probe the optical response of such model systems with nm-resolution. Besides the investigation of the bare oxide films, this is especially interesting for deposited metal particles, because it allows to connect geometric particle properties(size, shape) with the emitted light. This opens the possibility to address questions, which are of relevance for photo-catalytic applications, e.g. on the influence of particle-particle or particle-interface interaction. These investigations also provide additional insights into the mechanisms, that govern the light emission from tunnel junctions.

The experiments presented in this work therefore present a contribution to unreveal the interplay between the morphology of a metal-particle/oxide system on the one hand and its electronic, optical and finally chemical behavior on the other. For this propose a number of different metal particles were deposited onto the MgO film. In order to extract general conclusions on the optical response and the growth of the metals, the MgO film was kept unchanged. This allows us to dedicate the observed changes exclusively to the metal properties and thereby to draw relations between these properties and the observed phenomena.

First of all, the morphological and optical properties of bare MgO films were investigated. Hereby the work of Benia[18], who first developed the preparation procedure for the MgO/Mo(001) system could be continued. These investigations are discussed in chapter(4.1). In addition a preparation procedure for CaO and LiO films was established(section (4.3)), which enables more studies on the influence of the support on the optical response of the metal particles in the future. These systems are however not only interesting as potential support for the particles, but might show intrinsic optical properties by their own, that can be studied by means Photon-Emission STM. Changes on the electronic and optical properties could also be induced by the incorporation of Li into the MgO film, as discussed in section(4.2). Li-doped MgO is hereby of particular importance for catalytic applications, as it is discussed as one potential model system for the oxidative coupling of methane[19, 20, 21].

In the second part of this work investigations on metal-particle systems are discussed. Hereby the growth of the different metals on the MgO film is presented first.

Furthermore the optical properties on single metal particles are investigated. This investigation gives rise to a general model for the light emission from different particles, which turned out to be influenced by tip interactions, as well as by properties of the MgO film. The spatial distribution of the optical response could be studied in addition, which allows to identify interactions between different particles and their interactions with the STM tip.

The experimental chapters are presented after the introduction of the theoretical background

of STM and the mechanisms, that govern the light emission from a tunnel junction. Furthermore the Photon-Emission STM setup is introduced, as well as the experimental techniques used in addition(LEED, GIXD).

Finally the work is summarized, by collecting the main conclusions and sketching future prospectives.

Chapter 2

Theoretical Background

The model systems mainly discussed in this work are consisting of a metal substrate, an oxide film and different metal particles covering the surface. Besides the topographic properties of this system, studied by means of Scanning Tunneling Microscopy(STM), the optical properties are of particular interest. This interest emerges for instance from future perspectives in photo-catalytic applications, where especially the combination of particles and band-gap materials is expected to be promising[22]. Thereby the possibility of tuning the optical response of these systems by the respective geometric properties of the metal particles is particularly important. However the overall optical properties are moreover influenced by the characteristics of the oxide film and the interactions between the different components. Whereas the optical response of a metal particle usually emerges from plasmon excitations; it is the excitation of excitons which is the crucial mechanism for band-gap materials. Referring to this distinction the following discussion is separated into two sections, dealing with *Plasmon Excitations* and *Exciton Excitations*, respectively. Furthermore a third section introduces the main effects, that might be important for the use of these systems in photo-catalytic applications.

2.1 Plasmonic Excitation

If the electron gas of a metal is exposed to an external electromagnetic field, the electrons can respond in a collective motion. Since the electrons are free to move, but the ionic lattice is not, a restoring Coulomb force evolves, which counteracts the influence of the electromagnetic field. Thus an oscillation of the electrons emerges. This collective electron motion is called plasma oscillation and can be found in many metal, whereas it is most pronounced for noble and alkali metals[5]. The quasi-particle associated with these quantized electron oscillations is called a plasmon. Although a plasmon is a quantum mechanical object, most of the physical aspects can be understood also in a classical picture of an oscillating electron gas. The electrons hereby oscillate in the potential formed by the ionic lattice of the crystal. According to this interpretation a stringent description can be derived from Maxwell's equations.

A reason that makes plasmon excitations important for optical properties, is their strong interaction with photons. Of particular importance hereby is the dependence of the actual plasmon energy on the geometric dimensions of the metal object. Thus, control of the geometry allows to alter the optical properties of a specific system basically over the whole visible spectral range. This can be impressively seen, comparing Ag colloids in solution(figure (2.1)) with bulk silver for example. The silvery shine of Ag bulk material is due to the high reflectivity, resulting from the ability of the electrons to efficiently screen the incoming electric field. Only at distinct frequencies(eigenfrequency) the electron gas can be excited to collective oscillations. This plasma frequency ω_p is given by:

$$\omega_p = \sqrt{\frac{n\,e^2}{\epsilon_0\,m}}\;, \tag{2.1}$$

with n the electron density, e the electron charge, m the electron mass and ϵ_0 the electric field constant. Above this plasmon resonance the electrons are not able to respond fast enough to an external electric field anymore and the material would become transparent. This is of course only true, if no inter-band transitions are present. Such inter-band absorptions are however an additional, crucial contribution determining the optical response of a material.

The optical response reflected by the silvery shine of the bulk material undergoes quiet dramatic changes, if the dimensions of the metallic object are in the range of the wavelength of light. Thereby the optical properties are governed by scattering and absorption, whereas

Figure 2.1: Colloidal solutions of silver, gold and bimetallic nano-particles(Au-Ag)[23]. Depending on the actual size or composition, the energy position of the plasmonic excitation can be tuned within a large spectral range.

scattering is dominating down to particles sizes of $\sim 10nm$, whereas absorption becomes more important for smaller particles. By preparing mono- and bi-metallic Au and Ag particles of varying size for example, the absorption characteristics of a colloidal solution can be tuned over the entire visible spectral range, as shown in figure (2.1)[23]. In this case the distinct optical properties are attributed to the excitations of so called Mie plasmons[24, 25]. Meaning the excitation of a collective motion of the free electron gas within the geometric restrictions of the particle dimensions.

In addition to plasmon excitations in a bulk material and a metallic particle, these excitations are also found at surfaces. These surface plasmons again show different properties, that are related to the special symmetry of a surface. In this case the oscillation of the electron density is perpendicular to the surface normal and restricted to the metal/vacuum interface. The resonance position for the surface plasmon is given by:

$$\omega_{sp} = \frac{\omega_p}{\sqrt{2}} \qquad (2.2)$$

Unlike the Mie-plasmons, the surface plasmon is in principle not able to couple to light. This results from the dispersion relation for a surface plasmon[26]:

$$k_x(\omega) = \frac{\omega}{c} \sqrt{\frac{\epsilon(\omega)\epsilon_m}{\epsilon(\omega) + \epsilon_m}} \ . \qquad (2.3)$$

In order get a coupling to photons, the dispersion curve has to cross with the one of the photon: $k_{ph} = \sqrt{\epsilon_m}\omega/c$. Since this is not the case, a coupling is prohibited by momentum- and energy conservation[26]. Consequently, the first observation of surface plasmons were not done optically, but by energy loss experiments[27]. However for rough or stepped surfaces a coupling could be observed, since the symmetry of the surface is broken for these cases and therefore a transfer of parallel momentum $k_{||}$ is possible[26, 28, 29].

However, for the optical phenomena discussed within this work, the bulk and surface plasmon excitations were not considered for the description of the experimental results. In particular for the metal particles deposited onto the thin oxide films the discussion has to involve Mie-plasmon excitations, which are described theoretically in the framework of the Mie-theory.

2.1.1 Mie theory

The theory was introduced by Gustav Mie[6] in 1908 and describes the electro-magnetic response of an isolated spherical nano-particle in a homogeneous dielectric surrounding by using classical electrodynamics. Both, the metal particle as well as the surrounding are described by their dielectric functions. In order to get the optical response of a complete system, a summation over all particles and their mutual interactions is done. Using the di-

electric function as the crucial input parameter, the implementation of various effects, as for example changes of material, temperature or structure can be done. For example, if particle sizes are smaller than $\sim 10 nm$ and thus electromagnetic properties are no longer approximated by the bulk dielectric function, a size dependent correction term can be introduced. On the other hand the Mie theory does not provide the possibility to do ab-initio calculations of optical properties, unless the indirect way of calculating the dielectric function first. This is however difficult in most cases and only possible for rather simplified structures. Usually, and particular for this work, dielectric functions extracted from experimental data is used in the calculations.

The calculation is done in a quasi static regime, which restricts the wavelength to values larger than the particles diameter. Otherwise retardation effects have to be taken into account, that are not included in the classical Mie-theory[5, 30]. If the particles are larger than the wavelength of the light, the electric field is modulated inside the particle, which gives rise to multi-polar excitation in addition to the dipolar excitations that govern the quasi static case. This can be described only with more elaborate, expanded theories[31, 32], such as the generalized Mie-theory. However, the Mie-theory provides reliable results for a large variety of different ensembles and can be relatively easy adapted to various particle sizes, shapes and environments[6, 5, 33].

The calculation provides the polarizability of a particle. It is calculated by solving the Laplace equation for the different media with step like boundary conditions at the particle/surrounding interface. Here the electronic potentials are approximated by a multi-pole expansion. For the simplest case of a spherical particle with diameter R this results in[5]:

$$\alpha(\omega) = 4\pi\epsilon_0 R^3 \frac{\epsilon(\omega) - \epsilon_m}{\epsilon(\omega) + 2\epsilon_m} \ , \tag{2.4}$$

where $\epsilon(\omega)$ is the dielectric function of the metal and ϵ_m the one of the surrounding medium. A resonance occurs, if $|\epsilon + 2\epsilon_m|$ gets minimal, giving rise to an almost Lorentzian shaped peak in the respective extinction spectra. Using the optical theorem the respective extinctions can be calculated[5]:

$$\sigma(\omega) \propto \text{Im}\,\alpha(\omega) \tag{2.5}$$

Figure (2.2) shows an example of calculated extinction spectra for different particle materials(Au, Ag, Cu) and diameters in a matrix with $\epsilon_m = 1$. The relatively sharp peak is due to the plasmon resonance of the respective materials and shows up at $\hbar\omega_p = 3.0\ eV$ for Au, at $3.5\ eV$ for Ag and at $2.3\ eV$ in the case of Cu. In addition a broad band is visible that overlaps with the plasmon in the case of Au and Cu. This band gives rise to a step-like increase in the extinction. Only in the case of Ag the two bands are distinctly separated. The second band is hereby attributed to the inter-band transition between the metal d-states and the empty p-band above E_F. For Ag this band sets in at energies higher than $\hbar\omega = 4eV$[34] and therefore it is well isolated from the plasmon peak.
The effect of the increasing particle diameter is most obvious for Ag and leads to a shift to lower energies, accompanied by an increased width of the corresponding peak.

A more realistic description of the experimental situation is achieved, if the actual shape of the metal particle is considered more precisely. This can be done using an ellipsoidal model geometry, instead of the spherical one. Such a problem can still be treated analytically. The polarizability is then given by[35]:
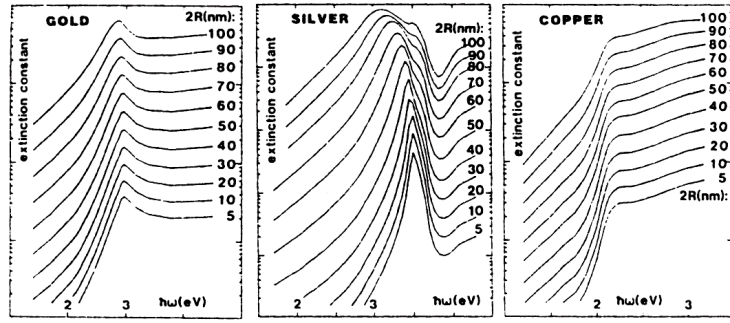
Figure 2.2: Extinction spectra for mono disperse spherical particles of gold(**a**), silver(**b**) and copper(**c**) with increasing particle diameter[5].

$$\alpha(\omega)_{x,y,z} = \frac{4\pi}{3} \, xyz \, \frac{\epsilon(\omega) - \epsilon_m}{\epsilon_m + L_{x,y,z}(\epsilon(\omega) - \epsilon_m)} \, , \qquad (2.6)$$

with $L_{x,y,z}$ being the so called geometric depolarization factor, that determines the electric polarizability along the corresponding axes x, y, z. The actual geometry is then expressed by the choice of $L_{x,y,z}$ at the constrain that $\sum L_{x,y,z} = 1$. Where $L_x \neq L_y \neq L_z$ for an ellipsoidal particle with three independent axes and $L_x = L_y = L_z = 1/3$ in the case of a spherical particle. From equation (2.6) it becomes clear, that the three Mie-modes for the x-, y- and z- axes are at the same energy in the latter case. This degeneration is lifted, if the axes are not equal anymore. Thus the single peak in the extinction spectra of a sphere split into three energetically separated peaks for the ellipsoid(figure (2.3.a)). Because the polarizability is smallest in the case of the shortest axis, the corresponding peak is the most blue-shifted one.
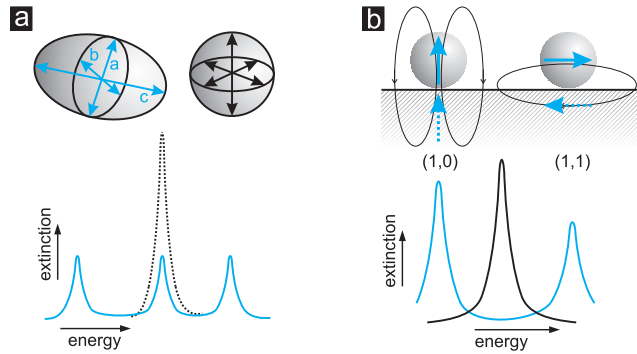

Figure 2.3: (**a**) Schematic representation for the emergence of the plasmon resonances in the case of an ellipsoidal particles, where the degeneration is lifted and the spherical particle exhibiting only one peak. (**b**) Influence of an polarizable substrate on the plasmon energy. Whereas perpendicular to the surface the induced image dipole increases, it decreases parallel to the surface, which leads to a energy separation of the modes compared to the isolated sphere.

Changes of the polarizibility can also be induced by interactions with the dielectric substrate. As illustrated in Figure (2.3.b) a spherical particle does only show one single degenerated peak. In contrast, for the supported particles two peaks emerge. The splitting is due to the induced dipoles in the underlying substrate, which increase the polarizability in the case of the $(1,0)$-mode(perpendicular to surface) and decreases it for the $(1,1)$-mode(parallel to surface). Furthermore it should be noted, that also interparticle interactions may lead to shifts of the plasmon modes. Whereby the in-plane modes are usually more affected, leading to a larger red-shift.

The effects sketched here are usually sufficient to describe the experimental data with a reasonable good agreement. The calculations shown in this work are hereby done with the Granfilm software by R. Lazzari and I. Simonsen, available in the web[36] and documented in Ref. [37].

2.2 Exciton Excitation

Photon irradiation of a band-gap material, can lead to an electron transfer from the valence band into the conduction band, if only the photon energy is larger than the band-gap E_{gap}. Such an electron leaves a hole with the opposite charge behind. The electron, as well as the hole can now run through inelastic scattering processes and release energy. On a time scale of typically some $100ns$[38] the attractive Coulomb interaction between electron and hole leads to the formation of a bound state(figure (2.4)). This bound electron-hole pair is called an exciton. In addition to this "indirect" excitation, electrons can also be transfered directly into excitonic states below the conduction band edge by absorption of photons of sub-gap energies[39]. Since excitons are unstable against recombination of the electrons with a hole, they are responsible for light emission from many semiconductors, oxides or molecules.

The wavefunction of an exciton is often referred to as hydrogen like, although the binding energies are much smaller and the respective particle sizes are larger[39]. This can be understood on the one hand by the presence of additional charges in the solid, which are able to screen the Coulomb forces efficiently. On the other hand, the effective mass of the excited electron-hole pair is much smaller compared to the hydrogen atom.
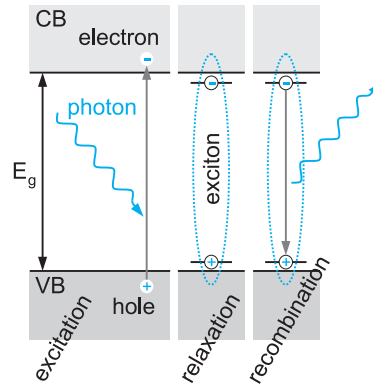

Figure 2.4: Schematic representation of the light emission mechanism involving the excitation of an exciton. First an electron-hole pair in created by irradiation with light. After relaxation an exciton is formed, which than recombines by emitting a photon. Whereby the excitation energy is usually higher than the actual energy of the emitted photon.

The system of an electron in the potential of a positively charged particle(hole) is usually treated similar to the hydrogen problem, although the Positronium, consisting of an electron and a positron, would be the even better association[39]. However, applying some changes to the hydrogen problem, its solution can be adopted to the exciton case.

Since the exciton is an excited state in the solid, the respective dielectric function of the crystal material ϵ has to be taken into account. Therefore the dielectric permittivity ϵ_0 changes to ϵ_m and the reduced effective masses are introduced for the electron m_e^* and the hole m_h^*. This leads to the exciton mass given by:

$$\frac{1}{\mu^*} = \frac{1}{m_e^*} + \frac{1}{m_h^*} \tag{2.7}$$

Hence, an exciton with the momentum $\vec{p} = \hbar\vec{k}$ has a total energy of:

$$E_{exc} = E_{gap} - \frac{\mu^* e^4}{2(4\pi\epsilon_0)^2 \epsilon^2 \hbar^2} \cdot \frac{1}{n^2} + \frac{\hbar^2 \vec{k}^2}{2(m_e^* + m_h^*)} \,, \tag{2.8}$$

where n is the quantum number and:

$$\frac{\mu^* e^4}{2(4\pi\epsilon_0)^2 \epsilon^2 \hbar^2} = \left(\frac{\mu^*}{m_e^* \epsilon^2}\right) \cdot 13,6\, eV = Ry^* \ , \tag{2.9}$$

is the excitonic Rydberg constant. Thus the second term in equation (2.8) represents the binding energy of the exciton and the third term gives the kinetic energy $E(\vec{k})$, or the dispersion relation, respectively.

Generally two types of excitons can be distinguished, as the limiting cases. Primarily found in semi-conductors with high dielectric constants are the so called Mott Wannier excitons[40, 41, 42]. Typical binding energies are in the range of a few to some hundred meV and thus the associated Bohr radius is relatively large(≈ 100Å).

Si	14,7	BaO	56	RbCl	440
Ge	4,15	InP	4,0	LiF	1000
GaAs	4,2	InSb	0,4	AgBr	20
GaP	3,5	KI	480	AgCl	30
CdS	29	KCl	400	TlCl	11
CdSe	15	KBr	400	TlBr	6

Table 2.1: Exciton binding energies in meV. Taken from [39].

As shown in table (2.1), there are materials that exhibit excitons with much larger binding energies, exceeding 1 eV. This type is usually referred to as Frenkel excitons[43, 44]. Contrary to the loosly bound Mott-Wannier exciton, the stronger bonding in this case leads to a much smaller electron-hole separation. Essentially it can be seen as an excitation, localized in the proximity of an atom, where in an oxide usually the hole is localized at the oxygen, whereas the electron is at the cation. In contrast to the Mott-Wannier excitons, which acts as a free moving particle in the crystal, the movement of a Frenkel exciton is considered as "hopping" of the atomic excitation from one atom to another.

Bound excitons A crystal always exhibits impurities, that can be either neutral or charged. Those impurities are foreign atoms or vacancies. Most defects are not able to move through the crystal at moderate temperatures or they are restricted to diffusion on rather long time scales. These immobile defects can act as traps for excitons. If the exciton is trapped at such defects it also becomes immobile. Therefore these trapped excitons are called bound exciton. The energy of the bound exciton is given by the energy of the free exciton reduced by the amount of the exciton/trap binding energy. In a rough approximation this binding energy shows a linear relation with the ionization energy of the respective defect[45], as found for example on zinc oxide[46].

2.2.1 Excitons in Magnesium Oxide

Magnesium oxide is an insulating material with a band gap of $7.8eV$[47, 48, 49, 50, 51]. Assuming Frenkel-type excitons with binding energies of ≈ 1 eV, one would expect light emission from such crystals in the ultra violet range, e.g. at energies of $6 - 7$ eV. Interestingly, light emission is observed also for energies well below this value. This behavior is explained by the presence of low-coordinated sites in the surface. Since the surface is never perfectly flat, it can exhibit atomic positions, that differ from the usual five-fold coordinated surface sites.

One can think of various kinds of low-coordinated sites, classified by the number of neighboring atoms. Corner atoms for example only have three nearest neighbors compared to an edge position with four and the atom on a terrace with five neighbors. Theoretical considerations show, that not only the number of the nearest neighbors is important, but also the next nearest neighbor can effect the electronic structure of a low-coordinated site. Accounting also for the next nearest neighbors, additional sites have to be distinguished, for example 3-fold coordinated kink sites or 4-fold-coordinated step sites(figure (2.5)).
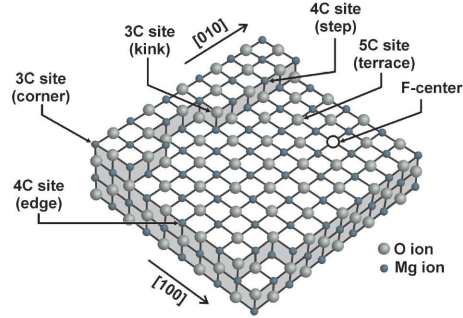

Figure 2.5: Scheme of different types of low-coordinated sites on the MgO surface[18].

Exciton mediated light emission with energies below the MgO gap value is usually assigned to those low-coordinated sites. Their electronic properties are different because of the reduction of the Madelung potential at these sites. The Madelung potential[52, 53] hereby gives a measure of the electrostatic energy for the respective site, introduced by the other ions of the lattice. Since this is mainly depended on the nearest neighbors, significant changes can be expected, if such neighbors are missing. Nonetheless, a reduced Madelung potential is not always sufficient to explain the experimental findings for excitonic energies[54]. The different excitation characteristic of the different sites are especially important for MgO. For this reason it is discussed in more detail in the following.

Many studies have been performed for MgO single crystals, powders and smokes, which show excitations energies much lower than the band-gap, being explained by exciton deactivation at low-coordinated sites[55, 54]. It was suggested that the light emission from MgO is caused exclusively by 3-fold coordinated sites, in particular by oxygen terminated corners O_{3C}^{2-}, irrespective of the excited surface site. This is however only possible, if the excitons are mobile and would deactivate by photon emission only at these O_{3C}^{2-} sites[56, 57], after the diffusion steps.
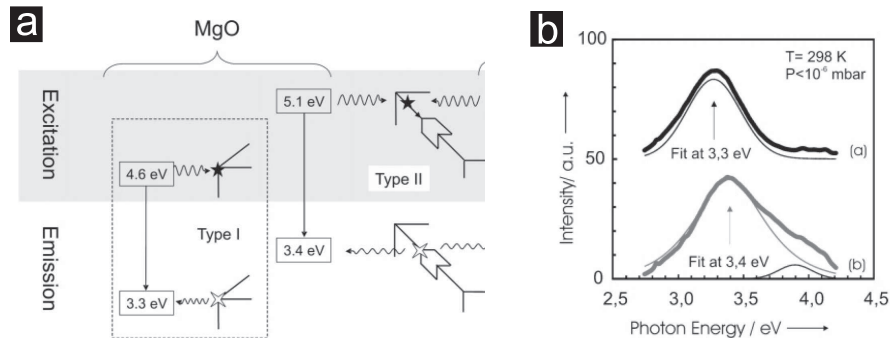

Figure 2.6: Room-temperature photoluminescence emission spectra of MgO nanocubes after excitation at (a) 4.6 and (b) 5.4 eV.[55]

Figure (2.6) shows a scheme of the excitation and deactivation of excitons on MgO, as

reported by Knözinger *et al.*[55]. The emission spectra were obtained from diffuse reflectance spectroscopy on MgO cubes and could be explained by accounting for two types of low-coordinated sites in the surface. The first one is the oxygen-terminated regular corner site, where the next neighbors are edge Mg^{2+}. Second the less regular, oxygen terminated corner sites, meaning sites, where some of the next neighbors are more than 4-fold coordinated, which is the case at kink positions. The third site taking part in the light emission mechanism are regular edge site, that are 4-fold coordinated. The observed two emission bands at 3.3 $eV(\hbar\omega_{excitation} = 4.6\ eV)$ and 3.4 $eV(5.4\ eV)$ could thus be explained by the following scheme.

An excitation at 4.6 eV is sufficient to activate the O_{3C}^{2-} corner site, which deactivates by the emission of photons with an energy of 3.3 eV. This assignment is confirmed by DFT calculation from Shluger *et al.*[58, 59], who first demonstrated the importance of this site for photo induced processes. Furthermore, this emission is enhanced for MgO cubes of small size($< 10nm$), where the fraction of corner to other sites is expected to be larger[60].

On the other hand the emission band at 3,4 eV is attributed to excitons initially created at the O_{4C}^{2-} edge sites. These excitons are mobile[57, 61, 62] and able to diffuse to sites with lower coordination. The detected emission at 3.4 eV corresponds to a deactivation at the less regular O-terminated corner and kink site[63, 64, 62, 65].

2.3 Aspects of Heterogeneous Photo-Catalysis

The systems studied in this work is particular interesting as a starting point to establish model systems, which allow the investigation of important aspects of photo-catalysis. Oxide films, as well as their combination with metal particles are supposed to open new photo-catalytic applications. The concept of photo-catalysis itself was first introduced by Fujishima and Honda in 1972, who observed water splitting on TiO_2 electrodes, if irradiated with UV-light[66]. The overall reaction hereby sums up to:

$$H_2O + 2h\nu \xrightarrow[TiO_2]{photo-catalyst} \frac{1}{2}O_2 + H_2 \tag{2.10}$$
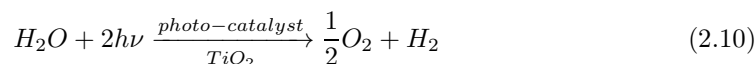
and represents a typical example for the concept of photo-catalysis, namely the acceleration of a reaction in the presence of a catalyst, being activated by the absorption of light. The water splitting on TiO_2 can be seen as the starting point for the ongoing research in this field. Since then, researchers have improved the understanding of the underlying physical and chemical processes[67, 68, 69]. The field of photo-catalysis has become particularly interesting in connection with energy renewal, energy storage and applications to environmental cleanup[70, 71, 72, 73, 74, 75, 76]. This is inspired by the potential of TiO_2-based photo-catalysts for the decomposition of organic compounds in polluted air or wastewater. The general interest on heterogeneous photo-catalysis is furthermore related to two aspects. First of all, the excitation by light irradiation can lead to electronic excitations of the respective molecules, which are not accessible by usual thermal activation. If however different excited states are involved, the available reactions pathways can be very different to common catalytic reactions. On the other hand the use of solid substrates and metal particles can alter the electronic structure of the adsorbed molecules. Since the bonding between molecule and substrate does not only affect the ground state of the adsorbate, but also the excited states, unique reaction pathway can emerge. Furthermore the complexity of photo-catalytic systems allows to tune the chemical performance as the interactions between adsorbate and substrate depends on a variety of different parameters. Therefore control of substrate and metal particle properties enables new catalytic applications.
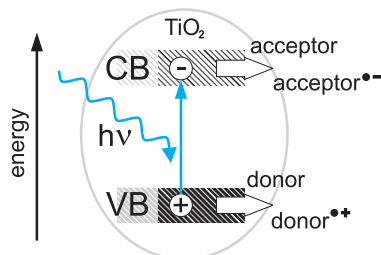

Figure 2.7: Schematic representation of the photo catalytic reaction principle. The electron(hole) generated by the absorption of photons is able to transfer to adsorpted acceptor(donor) molecules forming radicals.

TiO_2 is one of the most extensively studied photo-catalyst and often used as a material for photo-oxidation. Hereby the decomposition of organic molecules can lead to an almost complete reaction of the educts to water and carbon dioxide. The mechanism can be sketched as following. Upon photon irradiation, electrons in the valence band transfered into the conduction band. In the case of TiO_2 an energy of $3.2 - 3.4\ eV$ for rutile and $3.0 - 3.1\ eV$ for anastase is needed for this excitation. These energies correspond to the band-gap values of the respective oxide phases. The electron-hole pairs generated by the absorbed photons can recombine again in a photon emission process. Electrons as well as holes can however also interact with adsorbates on the surface. In the simplified scheme of figure (2.7) the
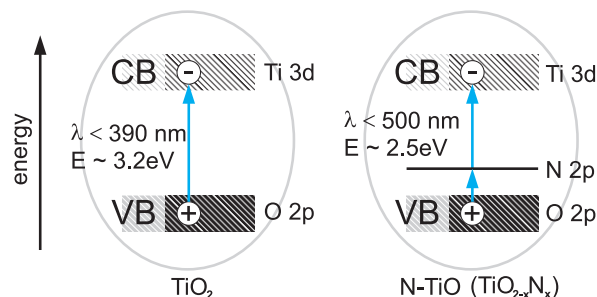
Figure 2.8: On the left side the Ti_2O band-gap of 3.2 eV is show. This band-gap energy can be reduced by the incorporation of nitrogen, that results in the development of a state in the gap and hence to a reduced excitation energy of 2.5 eV.

electrons can be catched by adsorbed O, leading to O-radicals. Furthermore the holes have a high oxidative potential and therefore possibly activate water, if present on the surface. The resulting hydroxyl-radicals can now oxidise organic species as well.

However, this simple model already shows some drawbacks of using these band-gap materials. The energy required for the separation of the charges is given by the energy difference of valence and conduction band. For TiO_2 this energy corresponds to UV light, that amounts to only 5% of the sun light used for the activation. Therefore research focused on ways to expand the window of "usable" light for the photo-catalytic reactions.

This can for instance be done by introducing foreign atoms into the oxide matrix. This idea is well known from semi-conductor physics, where the electronic properties are changed by the insertion of different amounts of atoms of different valence. In the case of TiO_2 this could be successfully established by doping with Nitrogen[77]. The N-doped TiO_2 showed a significantly enhanced absorbance in the visible spectral range(resulting in its yellow color), that leads to an increase in the photo-catalytic performance. The enhanced absorbance was explained by the narrowing of the band-gap[77] and later by the existence of an occupied mid-gap level[78, 79], which also reduces the energy, required for the charge separation(figure (2.8)).

Furthermore the photo-catalytic performance of oxides is reduced by the recombination of electron-hole pairs without taking part in the oxidation steps. In order to counteract this mechanism the incorporation of metal nano-particles was established. For TiO_2 this was done for example with noble metal particles(Au, Ag). The photo-catalytic performance can be enhanced, if the amount of metal is in the range of $1 - 5\%$. In a simple picture this effect can be understood by the fact, that the Fermi level of the noble metal is closely below the conduction band of the oxide. If the electron-hole pair is generated, the electron in the conduction band is now easily trapped by the metal(figure (2.9)). Therefore it is missing for the recombination with holes. Hence oxidation is enhanced by the quenching of the recombination channel.

Besides the photo-catalytic performance of band-gap materials, e.g. semi-conductor or oxides, the role of metal nano particles is rarely investigated. Nevertheless metal nano particles deposited onto band-gap materials might lead to completely new phenomena. The photo-chemistry hereby can be influenced by the morphology of the particle ensembles and their specific optical properties. Especially the optical properties of such particles are tunable within wide limits by controlling the shape, size and environmental parameter. One usual model system for the investigation consists of a metal substrate, a band-gap material(MgO in this work) and the metal particles. Besides the metal particle approach, also the deposition of molecules on oxide is a common photo-catalytic system. An important application is for instance the Grätzel cell, which uses dye molecules to transfer the photon energy into the
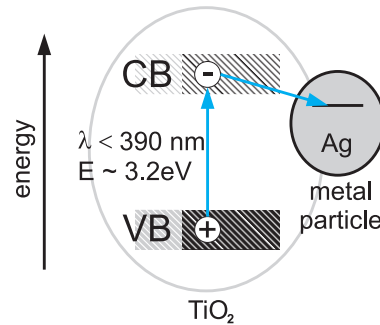
Figure 2.9: Embedded metal particles provide states closely below the Ti_2O conduction band edge. Electrons that transfer into these states are no longer available for the recombination with the holes in the valence band.

oxide[80, 81, 82]. Thereby photo-catalytic performance is driven by the complex interactions and energy exchange mechanisms between the different constituents.

Recent attempts focused on nanometer-sized metal particles supported by thin oxide films[83, 84, 11, 4]. Chemical reaction for such systems were studied for example on size selected metal particles soft landed on solid surfaces[85], where also catalytic cycles could be observed[86, 87, 88, 89]. However, studies on photo-catalytic properties of particles on surface are almost not present in the literature.

Metal particles on oxide surfaces open a wide field of new phenomena, which is due to the unique optical response. First the electronic structure of small particles can be very different to bulk materials and shows moreover a strong size dependence. Furthermore their absorption properties are governed by collective electronic excitations, tunable over the entire UV/VIS spectral range. And also effects of particle-particle interactions might influence the optical performance. Therefore some of the effects, which might influence the photo-catalytic properties of such system shall be sketched in the following.

Catalytic activity also refers to the ability of a catalyst to induces dissociation or desorption processes. In the case of photo-catalysis, the energy introduced into the system via the photon has to bring the molecule to a position on the Frank-Condon curve, where the slope is sufficient to result in a nuclear motion. Such mechanisms are well described in the frame work of Desorption Induced by Electronic Transitions(DIET[90, 91, 92]). Depending of the electron energies involved, different processes are possible. At higher energies($40\ eV$) molecules can be directly excited. The cross-section for the generation of high energetic electrons by the absorption of light is however small. Therefore mainly low energetic electrons have to be considered. This is especially true for metal particles, where the initial excitation of a plasmon leads to the creation of hot electrons and electron-hole pairs(via Landau damping[93, 94]). Those hot carriers cool down in the following by electron-electron interaction and at lower temperatures also via electron-phonon coupling. The hot electron distribution hereby contains electrons of energies which match the negative ion resonance of adsorbed molecules. In this case the electrons can transfer to the molecule and induce desorption via an electron-attachment process[95, 96, 97, 98]. Such a process is however restricted to specific energies and therefore the process of redistributing the energy is crucial to provide electrons with energies of the transient molecular state.

In addition metal particles might also contribute to the photo catalytic performance by effects, that are related to their specific geometry. Compared to single crystal surfaces, where electron-hole pairs easily penetrate into the bulk, the excitons confinement in a small particles might result in a higher electron temperature[99]. The confinement of the electron-hole pairs also leads to enhanced densities of available hot electrons. This effect might be further

increased by the enhanced interface scattering, which leaves the energy inside the particle, as well as possible changes on the hot electron transfer dynamics at specific sites of the particle. The use of the supported metal particles may also result in an enhancement of thermal desorption contributions. Since an oxide film separates the metal particle from the metallic substrate, the actual heat conduction can be dramatically decreased. Thus the particles could reach higher temperatures and stay hot longer. The respective heat conductivity is however strongly dependent on the supporting material and therefore represents a further parameter for rendering the photo-catalytic activity.

In general for metal particle systems non linear processes could be more important compared to single crystal surfaces. This is due to the antenna effect, resulting in a concentration of the absorbed energy at the relatively small and confined positions of the particles and thus strongly increased electron densities. Under such conditions, transient transfer into negative ion resonances as well as direct molecular excitations might become enhanced. This effect might also be further increased by the creation of so called "hot spots"[100]. This centers of strongly enhanced electromagnetic field are generated by a non-linear coupling of the plasmonic field of individual particles. These strong energy localizations are found for specific particles arrangements and might possibly created by artificial networks.

However most of the suggested mechanisms governing the photo-catalytic performance of supported metal particles systems are not yet studied. Many aspects are still unclear and experimental as well as theoretical work is only rarely found in the literature. Nevertheless, the great potential of rendering the photo-catalytic properties or even to access new catalytic pathway makes the investigation of such systems very promising.

Chapter 3

Experimental Background

3.1 Photon Scanning Tunneling Microscopy

In order to access optical properties on a local scale, a Scanning Tunneling Microscope (STM) with an optical readout is used in this work. To account for this combination of an optical measurement and the STM, this section is divided into three parts. The first part reviews the general principle, as well as theoretical aspects of STM. The second part concentrates on the Field-Enhancement in the tip/sample cavity and the Tip Induced Plasmon(TIP), as the mechanisms that strongly influence the light emission from a tunnel junction. Finally the experimental setup of the Photon Emission Scanning Tunneling Microscope(PSTM) is presented.

3.1.1 Principle and Theory of STM

The method of scanning tunneling microscopy was introduced by Binnig and Rohrer [101] in 1982 and awarded with the Nobel prize in 1986, together with Ernst Ruska(electron optics and first electron microscope). Since this years the technique has undergo many advancements and developed into a well-established tool in surface science to provide real space geometric and electronic informations. Nowadays a variety of different implementations of STM exist, which give insight into a large number of different sample properties. Despite of the topographic information, which for example enables the investigation of atomic arrangements or the identification of adsorption sites[102, 103], the method of scanning tunneling spectroscopy(STS)[104, 105, 106] offers the opportunity to locally probe the conductance of the surface or of adsorbed species. Furthermore the vibrational properties of molecules on surfaces or the surfaces itself can be probed by Inelastic Electron Tunneling Spectroscopy(IETS)[107, 108, 109, 110]. By applying magnetic fields and the use of magnetically polarized tips, the STM(Spin Polarized STM)[111, 112, 113, 114] can be used to visualize magnetic domains, study Kondo systems and even manipulate the spin orientation of surface atoms. Not only the spin state can be manipulated with the STM tip, but also the conformation of molecules or the lateral arrangement of surface atoms. Thereby the possibility to manipulate the position of adsorbates can be used to build artificial structures to get insight into the quantum-mechanic nature of such systems or to create electronic devices on the nm scale.

It has been shown, that the STM can be used in various environments, e.g. in Ultra High Vacuum(UHV), air or solutions. Furthermore, they operate in different temperatures regimes, from $1300K$[115] to liquid nitrogen, liquid Helium temperatures, down to a few mK[116, 117]. This variability makes the STM a perfect tool to be widely used in all kinds of scientific disciplines, as in surface science, material science, biology or nano-electronics.
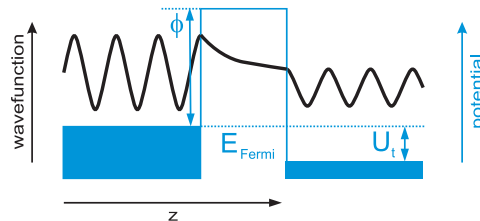

Figure 3.1: Schematic representation of the situation for an electron tunneling through a classical forbidden barrier. On the left side the electron is reflected at the potential step, but the corresponding wavefunction shows an exponential decay within the barrier, which leads to the existence of a non zero wavefunction on the right side of the barrier.

The working principle of STM is hereby based on the quantum-mechanical effect of electron
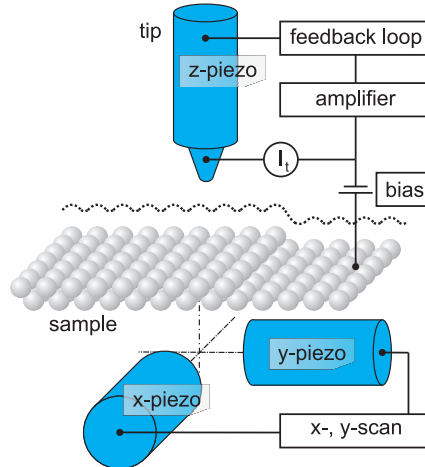
Figure 3.2: Representation of the basic working principle of an STM setup. The line-by-line scanning is done by the x- and y-piezo's, for this case. Whereas simultaneously the tip, carried by the z-piezo, retraces the sample topography, changing the distance. The tip-sample separation is controlled by a feedback-loop.

tunneling, which was first described by Gurney/Condon[118] in 1928. The one dimensional tunnel effect is sketched in figure (3.1), where the electron, described by its wavefunction, penetrates an energy barrier of the height ϕ. In contrast to the classical case, in which the electron is reflected as long as its energy E is smaller than the barrier height, the quantum-mechanical wavefunction decays exponentially into the barrier and the electron therefore has a non-zero probability to be transmitted even for $E < \phi$. This effect is used by STM in the way, that an atomically sharp metal tip is approached to a conductive or semi-conductive surface to distances, where tunneling becomes feasible. A voltage is applied to this junction, which leads to a measurable tunnel current in the range of pA to nA for distances of a few Å.

The tunneling current can be written in a first and simple consideration, as being proportional to the exponent of the distance d:

$$I_t \propto U_t \, \exp\left(-2\,\sqrt{\frac{2m\Phi}{\hbar^2}}\,d\right) \tag{3.1}$$

with U_t the bias and Φ the work-function. This exponential dependence explains the high sensitivity of STM in the z-direction(according to figure (3.2)). In order to produce a three dimensional image of the surface, the sharp tip is scanned line by line, with the help of piezo electric crystals(piezo's). Commonly two different modes of operation are used to acquire topographic data. In the *constant height mode* the I_t-signal is plotted versus the x- and y-coordinates. Since the height of the tip is not changed in this mode, scanning can be rather fast, reaching video frequencies[119]. This is used for instance to study dynamic processes, as film growth or diffusion on surfaces[120, 121]. The scanning of heavily corrugated samples is certainly not possible, because this would cause tip damages. However, corrugated surfaces can be investigated in the *constant current mode*, because here the tip is prevented from damages at the price of larger acquisition times. The information to create the image, is the z-displacement, meaning the distance between tip and sample. This distance changes while scanning, because a feedback loop controls the z-piezo in the way, that the current signal always equals a pre-set value. The tip therefore follows the topography of the surface. In this work exclusively the *constant current mode* was used.

Theoretical Aspects of STM

As mentioned above, the contrast mechanism in STM can be viewed as a consequence of the exponential dependence of the tunneling current on the tip/sample separation, as described by equation (3.1). This approach however, is not adequate for an exact representation of the real experimental situation, because it doesn't include important parameters, such as the electronic states in tip and sample, the geometry of the tip or the presence of inelastic tunnel processes. Therefore a number of different models have been developed to account for this parameters. But still an exact theoretical description is extremely difficult and requires a permanent refinement of these models.

One of the first and widely used approaches to describe tunnel processes was given by Bardeen[122]. Here a layer system of two metal electrodes separated by an insulator is treated with one dimensional perturbation theory. The two independent electrodes on both sides of the barrier(insulator) are described by their overlapping eigenfunctions. The transition probability from an initial states $|i\rangle$ on one side to a final state $|f\rangle$ on the other, is calculated in the presence of a small perturbation of the potential. The transition probability is given by Fermi´s Golden Rule:

$$w_{i,f} = \frac{2\pi}{\hbar} \ |M_{i,f}|^2 \ \delta(E_i - E_f) \qquad (3.2)$$

with the transition matrix:

$$M_{i,f} = -\frac{\hbar^2}{2m} \int (\psi_f^* \nabla \psi_i - \psi_i \nabla \psi_f^*) \, d\vec{S} \qquad (3.3)$$

where the integration is done over an area between tip and sample electrode and ψ_i and ψ_f are the wavefunctions of initial and final state in tip and sample. With the assumption of small voltages and a temperature of $0K$, where the Fermi-Dirac distribution $f(E)$ (energy distribution at temperature T) is a step function, the tunnel current is expressed by:

$$I_t = \frac{2\pi}{\hbar} e^2 U_t \ \sum_{i,f} |M_{i,f}|^2 \, \delta(E_i - E_F) \, \delta(E_f - E_F) \qquad (3.4)$$

with the energy of the initial E_i and final state E_f, the Fermi energy E_F and $\delta(E)$ the Dirac´s delta function.

The first comprehensive theory of STM was done by Tersoff and Hamann[123, 124]. Adapting the approach of Bardeen, here the three dimensional case is treated by modeling the STM tip with a spherical potential with only s-like eigenfunctions. The tunnel current is then proportional to the convolution of the local density of states(LDOS) of the sample at the position of the tip. According to the Wentzel-Kramers-Brillouin(WKB)-approximation I_t is given by:

$$I_t \propto \int_{-\infty}^{\infty} \rho_s(E)\rho_t(E - eV_s)T(d, E, eV_s)\left[f(E - eV_s, T) - f(E, T)\right] dE \ . \qquad (3.5)$$

With ρ_s and ρ_t the density of states of sample and tip, respectively and the transition probability:

$$T = \exp\left(-2d\frac{\sqrt{2m}}{\hbar}\sqrt{\frac{\Phi_s + \Phi_t}{2} + \frac{eV_s}{2} - E}\right) \tag{3.6}$$

depending on the tip/sample separation d, the workfunctions of tip Φ_t and sample Φ_s and the applied potential eV_s. Following the same assumption mentioned above(small bias and $0K$), formula (3.5) simplifies to:

$$I_t \propto \int_0^{eV_s} \rho_s(E)\, \rho_t(E - eV_s)\, T(d, E, eV_s)\, dE \tag{3.7}$$

This implies, that in the case of the *constant current mode* the observed corrugation is the plane of constant integrated LDOS on the surface. This is the usual starting point for the interpretation of STM data and emphasises again the fact, that the observed topography is a convolution of geometric and electronic contributions.

3.1.2   Light Emission in STM

The investigations described in this work are based on the combination of the topographic information provided by STM and a system, which allows to extract optical properties of the respective samples. The technique, that is introduced in detail below, provides light emission data by an electro-luminescence experiment. Hereby the tip serves the electrons for the excitation of luminescence light. Using this specific applications of STM, it is possible to study the optical properties of surfaces[125, 126], single adsorbate[127, 128] or metal particles[129]. Whereas the main advantage is the high lateral resolution, which allows to address the optical response of nano-sized objects.

Adding this optical probe hereby allows to counteract the lack of chemical sensitivity of STM in some cases. Although Scanning Tunneling Spectroscopy(STS) can probe the LDOS, as one possible way to obtain chemical information, the optical measurement allows to probe the unique optical properties of a chemical species. Instead of the electronic structure, which is often not known for an adsorbed species, the optical transition can be compared to a broad amount of optical data present in the literature. This is due to the fact, that the correlation of the energy of emitted photons with the intrinsic electronic transitions of specific elements or compounds was known in principle already in the nineteenth century. A more systematic use however, came up in the 1950's by chemical analysis techniques like Atomic Absorption Spectroscopy(AAS) [79,80].

PSTM furthermore allows to overcome the limit of spatial resolution given by Abbe's law, simply by using the confined electron beam of the tunneling tip to stimulated the light emission. Indeed, light emission from a STM junction could be observed in a number of different experiments[125, 126, 130]. And especially if molecules are considered for the light emission, the above mentioned correlation of the chemical identity and the observed emission lines was verified[131, 132]. However in many experiments it has been realized, that the actual optical response does not only depend on the properties of the species probed by the STM tip. But the spectral distribution, as well as the intensity is often strongly affected by the material and shape of the tip and the conditions of operation; the applied bias and the respective tip-sample separation. Some of these relations are discussed here.

Light emission from a tunnel junction(metal-oxide-metal) was first observed by Lambe and Mc Carthy in 1976[133]. The first light emission from STM was obtained by Gimzewski *et al.* in 1988 using a Ta tip on a Si(111) surface[130].
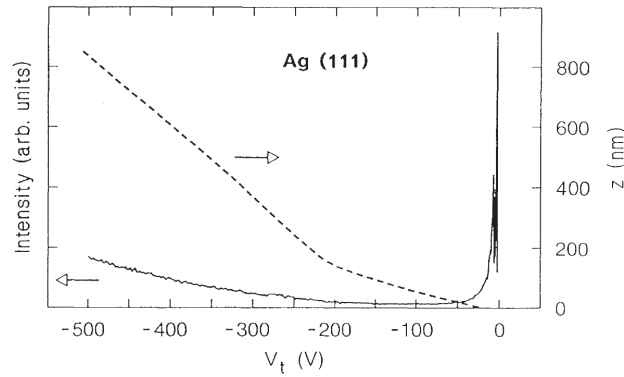
Figure 3.3: Light emission intensity(left - bold line) versus the voltage applied to the STM tip. The dashed curve indicated the associated tip-sample separation(right side) for the bias. Evident from this data is the sudden increase of the measured photon yield for tip-sample distances smaller than the wavelength of the emitted light(VIS).

This experiments can be seen as a starting point for a more strict investigation of the mechanisms, which are responsible for the light creation. Figure (3.3) shows the bias dependence of the integrated photon intensity for a typical STM junction. Evident from this data is the fact, that not only the applied bias, but also the associated tip-sample separation is of great importance for the observed light emission. At smaller distances(smaller bias) the photon intensity shows a sudden and drastic increase. The fact that this happens at the point, where the distances are in the range of the emitted wavelength points already to the significance of the interactions between tip and sample.

Electrons that hit the surface can produce radiation in principle by three processes: (1) initiation of radiative inter-band transitions, (2) excitation of plasmons and (3) bremsstrahlung. Since the cross section for bremsstrahlung is small for the voltages used in this experimental work, its contribution is neglected.

The remaining two mechanisms have been identified in the last 20 years to have strong influence on the light emission in a tunnel junction. On the one hand inelastic tunneling between tip and sample can activate optical modes in the junction, whereas the electron energy is transferred to this mode. Furthermore the spatially confined tunneling electron beam can act as a source for electro luminescence, as mentioned before. In this case the optically active mode is located directly at the surface, rather then in the gap.

However, the possibility to get sufficient photon intensities in both situations is not clear from the beginning. The usual quantum efficiency for this processes are in the range of 10^{-11} photon per electron and thereby close to the detection limit, even for classical electro luminescence experiments. Nevertheless Gimzewski *et. al.*[134] observed photon emission from an silver covered Si substrate probed with an Ir tip in 1989. Here two interesting experimental findings could be made. First, a cutoff wavelength $\lambda_c = hc/eV_t$ in the spectral distribution of the emitted light was found by increasing the excitation bias eV_t. And second, the energetic position of the observed peak did not change anymore for voltages $V_t \gtrsim 3V$. Thus Gimzewski *et al.* interpreted the light emission to be caused by an inelastic excitation at exactly this energy. Referring to this work, this idea was confirmed by the theoretical considerations of Johansson *et al.*[135].

If the tip is in close proximity to the surface, likely processes to appear are the excitation of plasmon modes by inelastic tunneling or the radiative decay of hot electrons. Hereby the collective electron excitations(plasmon) are preferentially found for materials of pronounced free electron character, as typical for metals. The recombination of electrons and holes how-

ever, is restricted to band-gap materials, as semiconductor or oxide materials. Nevertheless the rather high photon intensities are not intrinsic to these light emission mechanisms. The observation of quantum efficiencies of 10^{-3} and 10^{-5} photons per electron are therefore rationalized by field enhancement effects, that evolve in the cavity formed of tip and surface. This effects can be captured by the approach of Tip Induced Plasmon(TIP), as introduced by Johansson[135].

Tip Induced Plasmons

The suggested mechanism for light emission before[133, 136] was the radiative decay of surface plasmons, excited by the tunneling electrons. But the conservation of parallel momentum makes radiative de-excitation only possible, if the surface translational symmetry is broken by surface roughness or irregularities. For the model given by Johansson *et al.*[126] the tip itself acts as a symmetry break. In addition the geometry of a tunnel junction is able to provide an electric field enhancement, often also referred to as the antenna effect.

In the Johansson approach the calculation of the emitted light intensity is separated into two problems. First the coupling between tunneling electrons and the electromagnetic field is calculated by the determination of the electric field in the cavity formed by the tip in close proximity to the surface. Secondly the fluctuation in the tunneling current are concerned, that act as the source of excitation. This is done in the non-retarded approach, which is suitable for a basic picture of the mechanism and moreover, the extracted theoretical predictions match with experimental result in many cases. However, where are retardeted models present[137, 138], which show a better agreement for some particular experimental measurements.
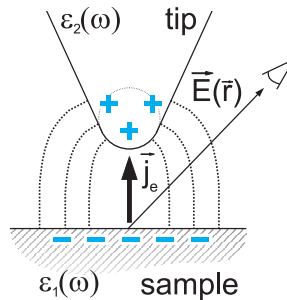

Figure 3.4: Schematic representation of the model geometry used to extract the electro-magnetic field distribution, as introduced by Johnasson *et al.*[126]

Considering the first part in this approach the electric field $E(\vec{r}, \omega)$ in a large distance from the tip, induced by the tunneling current density $j(\vec{r}', \omega)$, is calculated. Applying the reciprocity theorem of electrodynamics the radiated field $E(\vec{r}, \omega)$ can be expressed as:

$$E(\vec{r}, \omega) = \frac{1}{j_0} \int E_{ind}(\vec{r}, \vec{r}', \omega) \, j(\vec{r}', \omega) d^3 r \qquad (3.8)$$

Where the right side of the equation can be viewed as the electric field $E_{ind}(\vec{r}, \vec{r}', \omega)$ at the position of the tip, resulting from a *delta*-shaped current density $j_0 \delta(\vec{x} - \vec{r})$ far away from the tip(figure (3.4)). E_{ind} itself is a product of the plane wave magnitude of the δ-function source and the factor $G(\vec{r}', \omega)$, in which the geometry and material properties of tip and sample are included. The current density $j(\vec{r}', \omega)$ in (3.8) itself can be expressed by:

$$j(\vec{r}',\omega) = -i\frac{e\hbar}{2m}\left(\frac{\partial \psi_f^*}{\partial z'}\psi_i - \psi_f^*\frac{\partial \psi_i}{\partial z'}\right)(\vec{r}') \tag{3.9}$$

where ψ_i and ψ_f are the initial and final states in tip and sample, respectively. With this expression equation (3.8) changes into:

$$E(\vec{r},\omega) = \frac{\omega}{c^2}\frac{e^{ik\vec{r}}}{\vec{r}}\frac{e\hbar}{2m}\int G(\vec{r}',\omega)\left(\frac{\partial \psi_f^*}{\partial z'}\psi_i - \psi_f^*\frac{\partial \psi_i}{\partial z'}\right)d^3\vec{r}' \tag{3.10}$$

In a simple picture the tip induced plasmon can be seen as the coupling between the surface plasmon of the tip with the sample surface, respectively. This coupling is however only sufficient, if the two electrodes are close to each other. For the case of a tunnel junction, where the distances between tip and sample are of 5Å–10Å, these interactions are reasonably strong. More general this field enhancement effects are always observed, if the wavelength of light is in the range of the dimensions of the junction.

3.1.3 Experimental Setup of Photon Emission Scanning Tunneling Microscopy

All experiments presented in this work are done under Ultra High Vacuum(UHV) conditions. The UHV system hereby consists of two chambers. A gate valve allows the separation of the chamber carrying the STM and the chamber used for sample preparation. The preparation chamber is equipped with a sputter gun(argon ion sputtering), two electron beam evaporators and a leak valve to flood the chamber with reactive gases(O_2, H_2O) and has a base pressure of $5\cdot10^{-10}$mbar. To do preparations at different temperatures the sample can be heated while deposition in two ways. A high temperature heating stage offers the possibility to bias the sample up to $2000V$, position a tungsten filament behind the sample and heat the sample by electron bombardment up to $2500K$. The temperature is hereby controlled by a pyrometer readout. This high temperatures are used for instance to prepare the clean Molybdenum surface by sputter/flash cycles. The sample can be also hold at different temperatures by heating(tungsten filament) or cooling the manipulator(LN_2 flow), covering a temperature range from $100K$ to $500K$, measured with a NiCr/NiAl thermocouple. The quality of substrate and the film preparations is checked via a two grid LEED mounted at this chamber.

After preparation the sample is transfered into the second chamber hosting the PSTM. This chamber has a base pressure of $2\cdot10^{-10}$mbar provided by an ion pump, which also supports Titan sublimation. The whole STM is surrounded by copper shields which are attached to a copper base plate, that can be cooled down to liquid nitrogen temperature by a LN_2-flow. For the vibrational damping the STM head itself is suspended to four springs and coupled to an eddy current damping system.

As sketched in figure (3.5) the STM is build in a Besocke design. Thereby the three outer piezos carry the sample plate. This plate is made of molybdenum and contains three ramps at the edges. The approach and the withdrawal are done by a tangential movement of the outer piezos, which is transformed into a movement in the z-direction by the ramps. The outer piezo also provide the movement in the x- and y-direction for the scanning and furthermore allow to move the sample macroscopically to access different sample areas. The z-piezo carries the tip and approaches the sample surface through a hole in the sample plate. This STM set up is build in a very stiff and compact way, in order to provide a high resonance frequency and therefore stable tunneling conditions. However, within this work a passive pneumatic damping system supporting the whole chamber was added to further
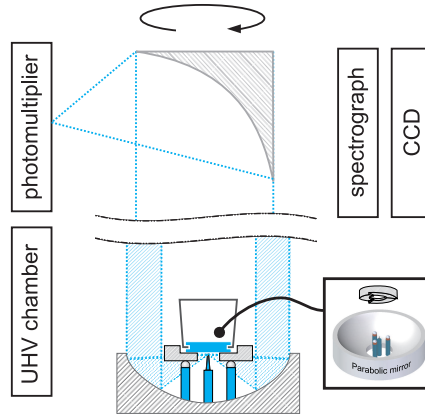
Figure 3.5: Scheme of the STM head(below) inside the UHV system. The Beetle-type head is surrounded by a parabolic mirror, which collects the emitted light from the tunnel junction and guide it through a quartz window out of the chamber. The light is then focused either on the spectrograph/CCD-detector or the photomultiplier.

improve the performance of this microscope. The compact design is also necessary to get access to the tunnel junction by means of an optical measurement. For this propose the STM is surrounded by a parabolic mirror as shown in figure (3.5). The focal length of the mirror is chosen such, that the apex in the tip is at the focal point. This ensures that most of the light emitted from the junction is collected by the mirror. The collection angle is however reduced by the shadows of the outer piezos and the area required by the microscope itself. Thus the parabolic mirror covers a room angle of around $3rad$ and collects emitted photons with angles of $30°$ to $90°$ with respect to the surface normal. The collected light is guided through a quartz window out of the UHV-system as a parallel beam and can therefore be easily analyzed with usual optical instruments. At this set-up two approaches are realized to investigate the emitted light. Either analyzing the light energy resolved or intensity integrated and correlated with the topographic coordinates. Therefore the parallel beam is focused by a second parabolic mirror outside the UHV chamber onto the two different detector systems. In order to investigate the spectral distribution of the light emission the focused light passes a PI/Acton SP-2156 spectrograph with a 1340×100-pixel CCD attached. For the reason of dark current minimization the detector is cooled with liquid nitrogen. Furthermore the spectrograph is equipped with two gratings(150 grooves/mm) with different blazings at $\lambda_{blaze} = 300nm$ and $500nm$. This is necessary to get sufficient intensity over an large spectral range($\sim$200nm(6.2eV) - 1000nm(1.2eV)). The typical measurement in the energy dispersive domain is done by positioning the tip above the nanoscopic object, applying voltages of $1V$ to $10V$ in the tunneling regime and $40V$ to $250V$ in the field emission regime, currents of $0.5nA$ to $5nA$ and using acquisition times of 1 to 10 minutes. The sensitivity curve shown in figure (3.6) is the optical function of the whole optical path and the detector functions.

To correlated topography and optical informations the light can also be focused onto a Hamamatsu R2949 photomultiplier tube. The photomultiplier provides a much higher quantum efficiency and can in principle detect single photons with readout frequencies of some MHz. Therefore the output voltages of the photomultiplier can be read as a second channel simultaneously with the topography channel. However the spectroscopic information is lost at this point, since the photomultiplier only provides a signal proportional to the integrated photon intensity over the spectral range given by the sensitivity curve of the szinsilator material. This disadvantage will be overcome to some extent in the future by the use of band pass filter to restrict the sensitivity curve to small spectral ranges. However in the experiments presented in this work, this approach provides the information of integrated photon inten-
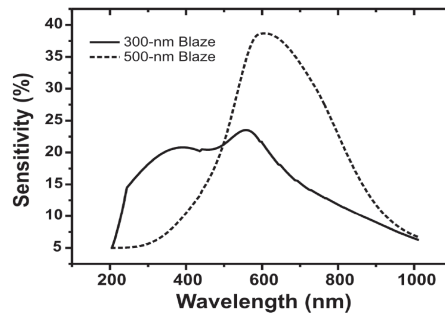
Figure 3.6: Measured sensitivity curves of the optical system of the photon-STM for the two different gratings in the spectrograph.
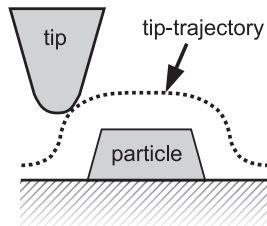

Figure 3.7: Real trajectory of the tip scanning a particle on a surface. This lateral error is usually compensated by a correction factor of 1.5.

sity at one position of the topographic image. For the interpretation of such photon-maps it should be pointed out, that in this experiment only the excitation is spatially limited to the beam of the tunneling electrons. The detection however does not have STM resolution. Thus a point of high intensity in a photon-maps is not necessarily the place of high photon yields emitted, but in principle marks the position, where the excitation of a light emitting process is most efficient. This fact however is important, if exciton diffusion or plasmonic excitations have to be considered.

It should be mentioned at this point, that the measurement of the lateral dimensions in STM is affiliated with a significant error, resulting from the convolution of the tip geometry and the respective surface corrugation, as sketched in figure (3.7). Usually the measured values are corrected with a factor of 1.5 to account for this effect.

Besides STM to acquire real space information, two methods where used to get reciprocal space information and thereby get insight into the symmetry and lattice parameters of the surface. Low Energy Electron Diffraction(LEED) was used to control the preparation process and as an additional tool to clarify the structure of the different oxide films. In the case of the thin MgO films Grazing Incidence X-ray Diffraction was used, as it provides a higher resolution, enhanced surface sensitivity and the possibility to extract out of plane lattice parameters. In the following this two methods will be shortly introduced.

3.2 Low Energy Electron Diffraction

Low Energy Electron Diffraction(LEED) uses the wave-like properties of electrons to provide information on the periodicity and symmetry of surfaces. The relation between momentum p and wavelength λ of an electron is given by the de Broglie equation. Since the momentum p is connected to the kinetic energy by $p = \sqrt{2m_0 E_{kin}}$ the de Broglie wavelength of an electron can be written as:

$$\lambda = \frac{h}{\sqrt{2meV}} \tag{3.11}$$

The accelerating voltages usually applied in LEED are in the range of $20 - 200\ V$. Therefore they correspond to a wavelength for the scattering electron of 3 to 1Å. These values are in the range of the inter-atomic distances for crystal surfaces, which allows to study surfaces by electron scattering. The use of rather low energies hereby restricts the depth of information. Electrons can penetrate the surface only 5 to 50Å at this energies, that leads to the high surface sensitivity of LEED.
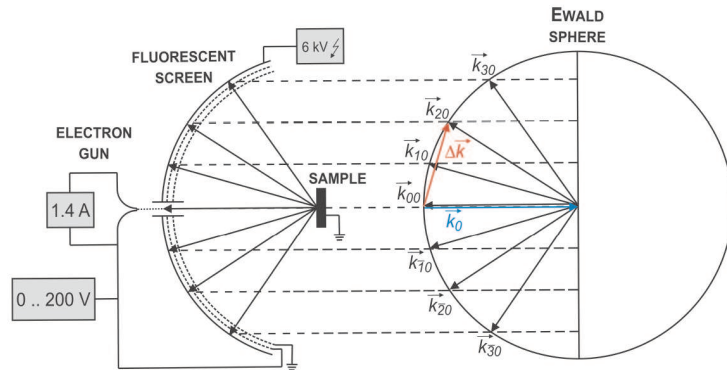

Figure 3.8: Basic principles of LEED. Incident electrons with a wave vector $\vec{k}_0$ are scattered from the surface with a wave vector $\vec{k}_{ij}$ of the same absolute value. Both are radii of the Ewald sphere. Diffraction spots are observed, where the component of the reciprocal space lattice perpendicular to the surface (dashed lines) intersects with the Ewald sphere.

Figure (3.8) shows a scheme of a usual LEED instrument and the principle of constructing the LEED patterns. The sketched construction is called Ewald sphere.

Starting from the incident electron with the wave vector $|\vec{k}_0| = 2\pi/\lambda$, the scattering vector $\Delta\vec{k}$ is calculated as the difference with the vector of the scattered electron $\vec{k}_{i,j}(i,j \in \mathbb{Z})$. A spot in the LEED pattern will appear at positions, at which the reciprocal lattice vector $\vec{G}$ intersects with the Ewalds sphere, given by the radii $\vec{r}_0$ or $\vec{k}_{i,j}$. At this intersection points the Bragg diffraction condition:

$$2d \, \sin\theta = n\lambda \tag{3.12}$$

is fulfilled. In this equation d is the distance between two adjacent lattice layers, θ is the angle between incident beam and surface plane and n is an integer. Hence, the condition for constructive interference can be expressed by:

$$\Delta\vec{k} = \vec{G} \, . \tag{3.13}$$

Thus a LEED pattern is interpreted as a representation of the surface symmetry in reciprocal space. The reciprocal pattern is hereby connected to the lattice parameters in real space by:

$$\exp\left(i\vec{F}\vec{G}\right) = 1 \tag{3.14}$$

where $\vec{F}$ are the atomic vectors of the real space crystal lattice.

The experimental setup of LEED is sketched in the left part of figure (3.8). It consists of an electron gun, that provides the electron beam. The thermal emission from a filament provides the electrons, which are accelerated and focused by electrostatic lenses onto the sample. After scattering at the surface, background electrons are deflected by repelling electrodes, whereas the scattered electrons pass and accelerate in a potential of typically 4 kV. These potentials are necessary to get sufficient intensities at the luminescent screen. A camera is mounted in front of the LEED screen, that allows the recording of the different patterns.

3.3 Grazing Incidence X-ray Diffraction

The method of X-ray Diffraction(XRD) is one of the essential tools to analyze bulk crystal structures, as it has some advantages, compared to other reciprocal space techniques, as LEED for example. First of all, X-rays exhibit only relatively weak interactions with matter, which offers the possibility to neglect multiple scattering in many cases. Furthermore photons with X-ray energies($1keV$ - $250keV$) have a significant penetration depth of 1 to $10\mu m$. Thus the structure information can be gained from large ensemble of atoms or molecules. But this advantages make XRD not an intrinsically surface-sensitive probe. However, some special approaches allow surface investigations with X-rays. One possibility, for example is to look for deviations in the scattering, when going from an ideal single crystal to the reconstructed surface or an ad-layer. This method is certainly restricted to single crystals of good quality, where the scattering is mostly limited to the Bragg peaks. Additionally, the interpretation is only possible by assuming models to fit the observed peaks. Another approach uses thin or transparent substrates or even freestanding films. The lateral structure analysis is done here, by just shining through the sample and a correlation of incident and scattered vector.
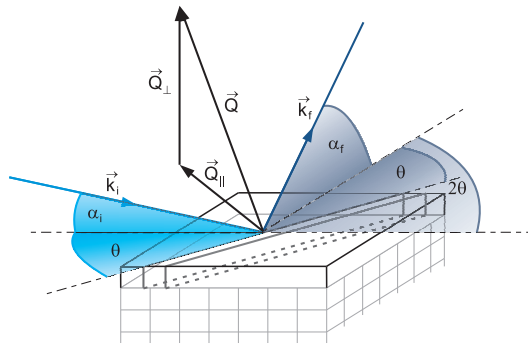

Figure 3.9: Scattering geometry in grazing incidence geometry, with $\vec{k}_i$ the incident and $\vec{k}_f$ the scattered beam vector. $\vec{Q}_\parallel$ and $\vec{Q}_\perp$ are vectors of parallel and perpendicular momentum transfer, respectivly.

A method which doesn't require transparent samples and avoids the scattering from the substrate is the Grazing Incidence X-Ray Diffraction(GIXD). GIXD uses in principle the same setup as an usual XRD experiment. But in its scattering geometry it combines the Bragg condition and the conditions for X-ray total external reflection. The geometry is shown in figure (3.9). In order to decrease bulk scattering the incident beam, of wave vector $\vec{k}_i$, is kept at an angle of α_i close to the critical angle for total reflection. At X-ray energies the refractive index for most materials is slightly smaller than 1 and thus the critical angle is typically in the range of 0.05° to 1.5°, depending on the substrate electron density and the beam energy. For such angles the only information from the substrate comes from the scattering of the evanescent wave, which still penetrates. The scattered beam $\vec{k}_f$ is measured at an angle α_f and 2θ in the plane. The momentum transfer $\vec{Q} = \vec{k}_f - \vec{k}_i$ is decomposed into a component parallel $\vec{Q}_\parallel$ and perpendicular $\vec{Q}_\perp$ to the surface. If α_i and α_f are small, then $\vec{Q}_\parallel$ is nearly parallel to the surface and the diffracting net planes are perpendicular. By rotating the sample the different net plane are brought into diffraction condition, which occurs, if both, incident and scattered beam form an angle of θ with the lattice plane. In this way the long range order parallel to the surface can be probed.

The basic expression for scattering at a three dimensional crystal is:

$$I(\vec{Q}) = AF^2(\vec{Q})\, S_{N_1}^2(\vec{Q} \cdot \vec{a}_1)\, S_{N_2}^2(\vec{Q} \cdot \vec{a}_2)\, S_{N_3}^3(\vec{Q} \cdot \vec{a}_3) \tag{3.15}$$

where A is a constant, N_j is the number of unit cells along the crystal axes, $S_{n_j}^2(\vec{Q} \cdot \vec{a}_j)$ is the interference function of N_j diffracting units and $F(\vec{Q})$ is the structure factor, which is a function of the atomic positions $\vec{r}_j$ within the unit cell. In the limit of $N \to \infty$, S_N is an array of Dirac delta functions and the intensity is only different from zero in the case that $\vec{Q}$ matches a vector of the reciprocal lattice of the basis $\vec{b}_1$, $\vec{b}_2$ and $\vec{b}_3$.

$$\vec{Q} = h\vec{b}_1 + k\vec{b}_2 + l\vec{b}_3 \quad h, k, l \text{ Miller indizes} \tag{3.16}$$

When this Laue condition is fulfilled, the intensity is given by:

$$I_{hkl} = AF_{hkl}^2 N_1^2 N_2^2 N_3^2 \tag{3.17}$$

This condition changes if only one layer is considered, where the basic cell vector a_3 perpendicular to the surface is chosen to a finite layer thickness and $N_3 = 1$, so that now the intensity out of plane is continuous, but still sharply peaked in the directions parallel to the surface. The reciprocal space is not longer a three dimensional spot pattern, but a pattern of rods perpendicular to the surface. Still the intensity along the rod can show some modulations, which are correlated to the z position of the atoms in the unit cell, the thickness of the film or to Bragg peaks of the underlying bulk. This can be modeled with a crystal that is truncated by a sharp surface. The intensity is then described as a product of a step function for the electron density variation in the z direction and an infinite lattice. This convolution of a three dimensional reciprocal lattice with the Fourier transformed step function, yields to a diffraction pattern like the one shown in figure (3.10). The intensity variation along the so called Crystal Truncation Rods(CTR) can now be expressed by replacing $S_{N_3}(Q_3 a_3)$ with $\sum_{n_3=-\infty}^{n_3=\infty} = \exp(iQ_3 a_3 n_3)$ in equation (3.15):

$$I(\vec{Q}) = I_{hkl}^{CTR} = \frac{\sin^2(N_1 a_1 Q_1/2) \ \sin^2(N_2 a_2 Q_2/2)}{\sin^2(a_1 Q_1/2) \sin^2(a_2 Q_2/2)} |F_{hkl}|^2 \underbrace{|F_{CTR}(Q_3)|^2}_{\frac{1}{2\sin(Q_3 a_3/2)}} \tag{3.18}$$

Not going into the details, the experimental situation is usually modeled by the adaptation of the Fourier components, meaning changes in the step function. For example the roughness of a surface layer can be described if the step function is replaced by a less abrupt function, being described with less Fourier components. Thus the intensity between the Bragg peaks is smaller compared to the perfectly truncated surface.

Experimentally, there are various problems to tackle. On the one hand an intensity problem, which arises from the fact that at glazing incidence only a very small fraction of the beam is focused onto the sample. Thus it is favorable to use synchrotron radiation of high intensities, although GIXD is also done with lavatory light sources. Synchrotron radiation additionally provides high brightness, high energy and angular resolution and tunability. Secondly, there high requirements on the precision of the sample movement, that leads to a number of different diffractometer setups[140, 141, 142, 143, 144, 145, 146].

The diffractometer used in this work supports a UHV chamber, which can be rotated to change the incidence angle α of the X-ray beam. A goniometric head inside the chamber allows the alignment of two perpendicular tilts ($X1$ and $X2$) and two translations (X, Z). Furthermore the whole goniometric head can be rotated, changing ω and thus allows the perpendicular and the parallel orientation with respect to the X-ray beam polarization. Two circles of the diffractometer are devoted to the two detector rotations, defining the Bragg angle projections δ parallel to the surface and the outgoing angle β with respect to the surface. To access large perpendicular momentum transfers(45° input and exit angles) the
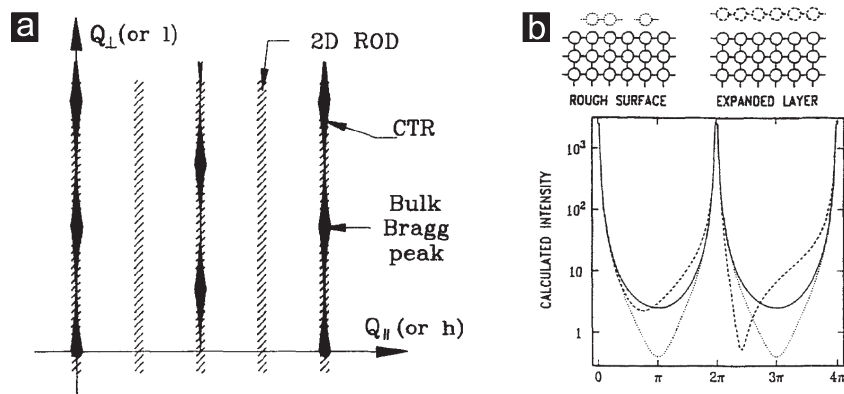
Figure 3.10: **(a)** Scheme of the reciprocal space continuous rods of diffraction(shaded rods) for a quasi-2D crystal and of a 3D crystal truncated by a surface, leading to crystal truncation rods(black filled) with maximum intensity at the Bragg positions. **(b)** Intensity variation along a crystal truncation rod for a perfectly sharp surface(full curve), a rough surface(dotted curve) and a surface with an expansion of 10% of the interplanar distance(broken curve)[139].
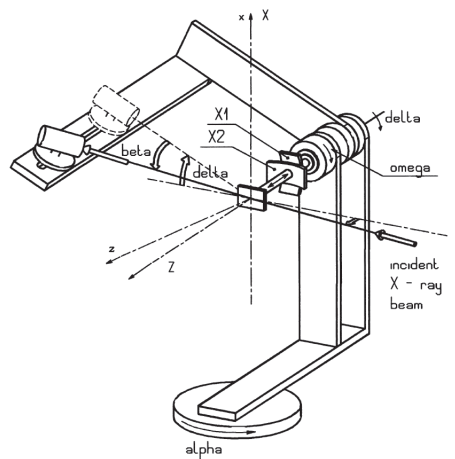

Figure 3.11: Sketch of the goniometric head used in the diffractometer. This setup allows to control two perpendicular tilts ($X1$ and $X2$), two translations (X, Z) and the angles ω, δ, θ.

UHV chamber has large windows made of Beryllium.

The used diffractometer is described in detail in Ref.[147], works at $18keV$ and is mounted to the BM32 beamline at the European Synchrotron Radiation Facility(ESRF) in Grenoble.

Chapter 4

Oxide Films

4.1 Magnesium Oxide Films

The metal oxide material mainly investigated in this work is magnesium oxide(MgO). It was chosen, because it is a well established model system in heterogeneous catalysis[148, 149, 150] and photo-catalysis[151]. This preference for experimental and theoretical studies hereby emerges from its simple crystallographic structure and the interesting chemical and optical properties.

MgO is a wide-gap material, crystallizing in the rather simple rock-salt structure(figure (4.1)) with a lattice constant of $421pm$. The unit cell consists of only two atoms, that makes it particularly suitable for a variety of theoretical approaches. Furthermore the band-gap of 7.8 eV[47, 48, 49] leads to good insulating properties, which are exploited in high-performance magnetic tunnel junctions for spintronic applications[152, 153, 154].

Some of the chemically important properties originate from the presence of different surface defects[14, 155]. The nature of these defects was already studied by many experimental techniques, as electron-energy-loss spectroscopy (EELS)[156, 157], infrared spectroscopy (IR)[158, 159], metastable impact electron spectroscopy (MIES)[160], scanning tunneling microscopy and spectroscopy (STM/STS)[161], electron paramagnetic resonance (EPR)[50], cathodoluminescence and photoluminescence spectroscopy[162, 163, 164].
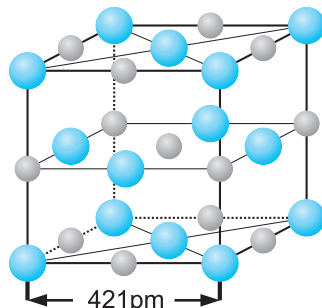

Figure 4.1: Crystallographic structure of bulk MgO. The interstitial octahedral sites of an fcc (facecentered cubic) network of O ions(blue) are occupied by Mg ions(grey) forming the rocksalt structure.

Since the bulk MgO is not conductive, thin MgO films deposited onto a Mo substrate are used in this work. Such an approach avoids charging during the STM measurements and furthermore allows to modify the interactions between the deposited metal particles and the underlaying substrate. The choice of molybdenum as the substrate is accompanied by lattice mismatch of 5.4%. This is a rather large value compared to other substrates used for the preparation of MgO films(3.0% for Ag(001)[165, 166, 167, 161] and 3.7% for Fe(001)[168, 153]). On the other hand the high melting point of the Mo promotes the preparation of well ordered, flat films via high temperature treatments.

4.1.1 Preparation of MgO films on Mo(001)

As mentioned the MgO films were prepared on a Mo(001) substrate. This substrate was chosen, because of its high melting temperature, offering the possibility to anneal the films to rather high temperatures and therefore reach a thermodynamically favorable configuration. The Mo substrate was cleaned by several sputter/anneal cycles before. Sputtering was hereby done at an argon pressure of $2 \cdot 10^{-6}$ mbar, at $2000\,V$ for $30-60$ minutes. Afterwards the sample was flashed to $2300K$ via electron bombardment from the backside of the sample. The quality of the substrate was checked by LEED that indicates a clear (1×1) pattern.

The MgO films were then grown by metal vapor deposition from an electron beam evaporator. The Magnesium is deposited onto the substrate in an oxygen pressure of $2 \cdot 10^{-7}$mbar at room temperature with a deposition rate calibrated to 1ML per minute. The coverage was calibrated by depositing Mg onto a clean metal surface, where a layer by layer growth is observed and the coverage can be determined directly by measuring the covered area by means of STM. After deposition only a diffuse LEED is observed, which indicates the disordered character of the film. Therefore the sample was annealed to $\sim$1000K for 10 minutes to initiate crystallization. In order to prepare MgO films of different thickness, the Mg deposition time was changed in this procedure. It was also possible to add MgO layers to an already prepared film.

4.1.2 Morphology of MgO Films of Different Thickness

Following this preparation procedure, MgO films of different thicknesses were grown. In general the films are rather flat, ordered and crystalline. However, exploring their structure by means of LEED, STM and GIXD, suggests a non pseudo-morphic growth. In fact the films undergo a number of relaxation steps, before an almost fully relaxed MgO lattice is reached at around 30ML coverage.

In the following this relaxation behavior is divided into three different regimes. The *low coverage regime* hereby ranges from sub-monolayer up to 5 – 6ML. The regime of *intermediate coverage* ranges from 6 to 12ML. And the *thick-film regime* starts at around 12ML. Although general properties of the film morphology can be described by the presence of different relaxation mechanisms occurring at different thicknesses, the transition are certainly not sharp, but go through intermediate states.

Low Coverage Regime 0-6ML

Sub-Monolayer Regime At this initial stage the morphology strongly depends on the annealing temperature applied after the deposition. This temperature dependence is summarized in figure (4.2), starting at temperatures above $700K$. For the as-grown and weakly annealed films(below $700K$) only a diffuse, almost featureless LEED pattern appears, that only in some cases shows a faint (1×1) structure. Therefore the film is supposed to be short-range ordered or exhibit even an amorphous structure. This was also confirmed by STM measurements, which only showed a rough surface morphology.

When the annealing temperature reaches $700K$, the film morphology changes into a crystalline structure, indicated by a LEED pattern that now exhibits a clear (1×1) structure. This crystallization seems to be fully completed at around $900K$. In STM the first crystalline features appear as small MgO patches on the surface. Measuring the height of such patches leads to a value of $\sim$(200±20)pm, which is very close to the height of the MgO monolayer(210pm). However STM images still show some disordered areas below $900K$ temperature.

This crystalline MgO patches, which are the dominating structure at this stage, show distinct edges aligned with the [110]- and [$\bar{1}$10]-directions of the Mo(001). Further annealing to $\sim$1000K, leads to an ordering process of the patches, that results in a stripe-like structure on the surface, with again monolayer height.

These stripe-like structures are consisting of equally sized building blocks. The size of these squared MgO islands is $\sim$50Å, similar to the islands formed at lower annealing temperatures. Also these stripes are aligned with the [110]- and the [$\bar{1}$10]-directions. Figure (4.3.b) shows a line scan along such a stripe pattern(indicated in (4.3.a)), where the regular dimensions of
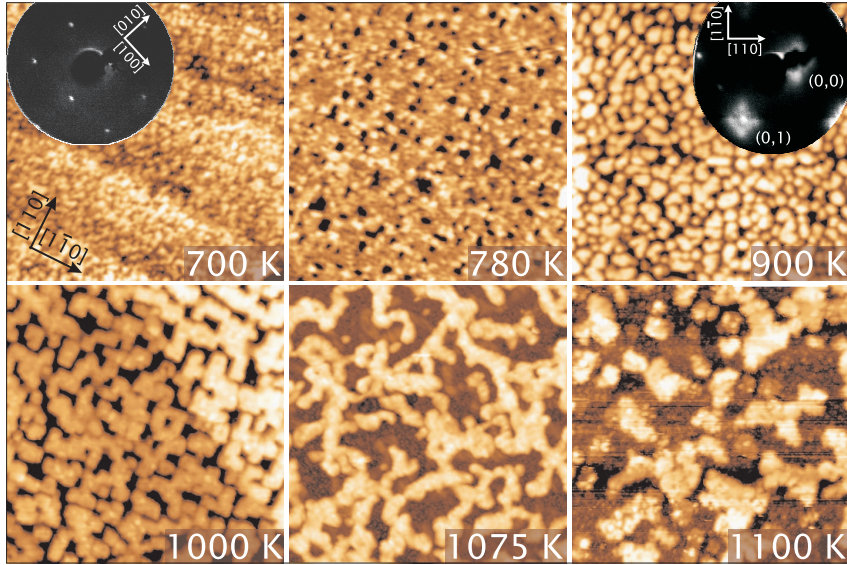
Figure 4.2: STM images($100\times100nm^2$, U =2.5V – 4.0V, 0.05nA) for the sub-monolayer film grown at room temperature and afterwards annealed(10min) to the temperature indicated in the respective image. The LEED pattern of the clean Mo(001)(left, 120eV) shows a sharp 1×1 structure. In the LEED pattern of the MgO film(right, 55eV), an more complex spot structure is evident, that is still 1×1.

the patches can be extracted. In addition the center-to-center distance could be measured and was found to be constant over large distances at the surface. It is interesting to note that this value(55Å±5Å) is almost equal to the periodicity of the dislocation network developing at higher coverages, suggesting a connection between the initial growth of the interface layer and the topography at higher thickness.
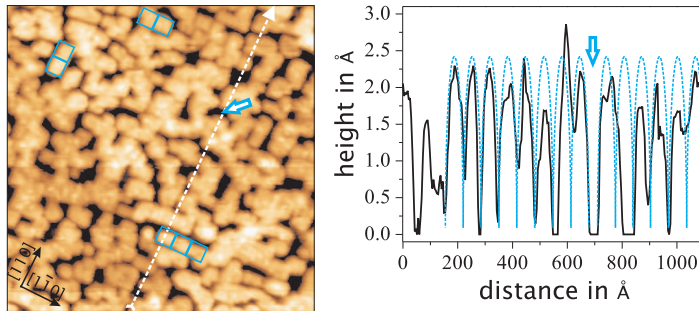

Figure 4.3: **(a)** STM image($90\times90nm^2$, U=4.0V) indicating the formation of a stripe-like structure on the surface, consisting of squared building blocks(black squares) with a size of ∼50Å. **(b)** Linescan across the stripe pattern indicated in (a), showing the periodicity(55Å) of the MgO patches.

The ordered MgO structures are not stable anymore, if a temperature of 1050K is reached, where coalescence and desorption processes of the MgO set in. The surface is dominated now, by irregular, randomly shaped islands and areas that show the bare Mo(001) surface again(figure (4.2)). The emergence of this disordered islands can be understood by increased Ostwald ripening processes, meaning the preferential growth of larger islands at the expense of smaller ones, due to an increased vapor pressure of the latter. This leads either to the formation of larger conglomerates on the surface or to the desorption of MgO from the surface. That desorption at such temperatures is a relevant process was already shown by Goodman *et al.*[169], where a similar value for the desorption temperature was found.

It turned out, that the morphology observed at sub-mono-layer coverage already reflects the growth of MgO films at higher dosage. Hereby the growth behavior of the thicker films can be traced back to the properties of the MgO/Mo interface.

Thicker films : STM The typical morphology of a 2ML thick MgO film is shown in the STM image in figure (4.4.a,b). Annealing to $1000K$ leads to the formation of a flat and closed film on the Mo surface. Only for coverages well below 2ML a number of holes are observed. Their edges align with the polar [110], as well as with the non-polar [100]-directions of the MgO.

The pronounced two-dimensional growth of MgO is expected, from the relatively large difference of the respective surface free energies of MgO($1.16J/m^2$) and Mo($3{,}87J/m^2$).
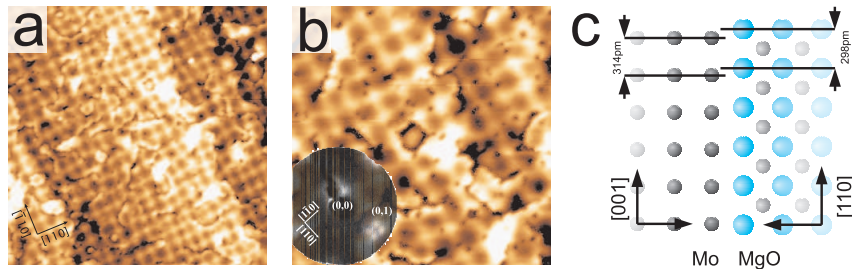

Figure 4.4: Typical STM images of a 2ML thick MgO film on Mo(001). **(a)** $100{\times}100nm^2$, $3.0V$, $0.05nA$; The MgO covers the whole Mo substrate over growing also step edges. **(b)** Similar preparations($50{\times}50nm^2$, $3.4V$, $0.04nA$). Besides dislocation lines and point-like defects a pronounced squared network structure is observed, whose symmetry is also present in LEED(inset). **(c)** Schematic view of the alignment of the MgO film on Mo(001); MgO[110]$\parallel$ Mo[001] and MgO(001)$\parallel$Mo(001)

The assignment of the MgO orientation is done by LEED and confirms the results from the calculation of the lattice mismatch between film and substrate for different alignments. For the lattice parameter of MgO $d_{\text{O-O}} = 298pm$ and Mo $d_{\text{Mo-Mo}} = 314pm$, it turns out that the smallest mismatch is achieved, when orienting the MgO [110]-direction parallel to the Mo [100]-direction, whereby the MgO(001) plane is parallel to the Mo(001)(figure (4.4.c)). The calculated lattice mismatch for this configuration amounts to 5.4%.

Besides the finding of a flat and closed film, the most striking observation at this thickness is however the presence of a well-resolved and long-range ordered network. This network structure consists of bright lines, that align with the [$\bar{1}$10]- and the [110]-directions of the MgO. The apparent corrugation of this lines in the STM amounts to 0.8Å at $3.5V$ and shows a clear square symmetry with a periodicity of 55Å±5Å. The fact, that this structure becomes very pronounced at particular voltages, indicates a certain electronic origin, apart from the topographic one. The network structure covers the whole surface and is even found to overgrow step edges and domain boundaries. It is interpreted as a dislocation network, formed by the introduction of additional planes into the film, in order to reduce misfit-induced lattice strain. This will be discussed in more detail in section (4.1.3).

STM also reveals a variety of defects on the surface, as for instance randomly oriented defect-lines, that seem to have its origin in domain boundaries formed by island growth at sub-monolayer coverages. Furthermore point-like defects are visible, which are associated with missing O or Mg atoms or even small vacancy clusters. This defects are preferentially found on the bright lines of the dislocation network suggesting a decreased MgO bonding for those sites.

LEED   Generally the LEED pattern of the MgO/Mo film for all coverages discussed in this work, shows a (1×1) structure, that indicates a nearly epitaxial growth of the film. True pseudo-morphic growth is however unlikely, due to the substantial mismatch. Relaxation of the film seems to be suitable to reach the bulk MgO lattice constant within the first few layers, at least concerning the LEED measurements. GIXD provides a more precise view into that, as shown below.

Despite of the observation of a (1×1) pattern, the internal structure of the diffraction spots is rather complex. In fact the spots are characterized by a four-fold splitting oriented along the [100]- and [010]-directions, which is 45° rotated with respect to the orientation of the network structure observed in STM.
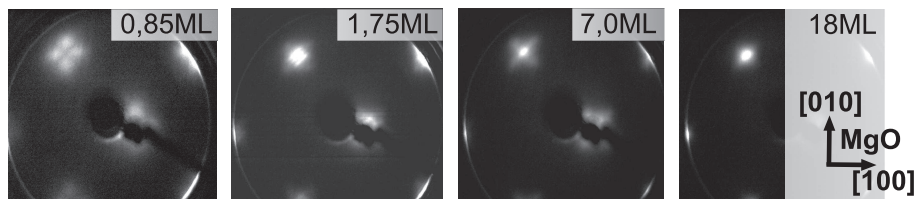

Figure 4.5: LEED pattern for MgO film on Mo(001) for different coverages at an energy of $55eV$. At all coverages a 1×1 structure is observed. Furthermore a distinct satellite structure is found, changing with increasing thickness. The origin of the satellite structure is attributed to the presence of tilted regions on the surface(see text).

Changing the energy, the scattering vector respectively, no change for the distance between satellite and central spot is observed on the screen. Such a behavior was already found for other systems [170, 171, 172] and is known to originate from surface areas which exhibit a certain tilt angle[173]. This satellite structure also depends on the nominal thickness of the film, as the distance between satellite and central spot becomes smaller with increasing MgO film thickness. Actually, the satellites disappear at coverages of around $6 - 7$ML. Since the satellite structure is attributed to the presence of tilted regions on the surface, it implies that the tilt angle becomes smaller for thicker films.

According to the LEED data, the angle decreases from ∼5° for the monolayer film to 1.5° at 6ML thick films. Such a behavior was also found for MgO/Fe(001)[174] and MgO/Ag(001)[175] and is attributed to a progressive flattening of the surface. The fraction of tilted regions on the surface seems to be rather large, since the central LEED spot is found to be almost fully suppressed. However, in some cases the internal structure of the spots undergoes changes, leading to additional splitting of the satellites or to an increased intensity of the central spot. Such dependencies on the electron energy and the film thickness could be caused by interference effects resulting from small height differences on the surface as discussed in the PHD thesis H.M. Benia[18]. No indication in LEED is found however, for the periodicity of the network structure, which might be due to the limited coherence length of the LEED system used in this experiments.

GIXD   Since LEED could not provide detailed information on the lattice parameter, due to the limitations in resolution, Grazing Incidence X-ray Diffraction(GIXD) was applied to this system. The results are shown in figure (4.6) and were reported by Benedetti *et al.*[176]. The scans are done using an angle of 0.166°, which is between the critical angle for total reflection of the Mo(0.19°) and the MgO(0.12°). The reciprocal lattice vectors are given in units of the Mo system, where h, k are the two in-plane parameters and l corresponds to the out of plane direction.

Increasing the thickness of the MgO film leads to the appearance of an additional peak next to the (200) Bragg peak of the Mo. This peak shifts to larger reciprocal lattice values
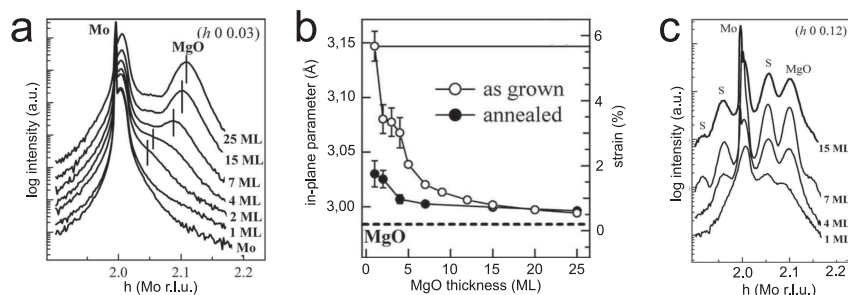
Figure 4.6: **(a)** Radial scan along the (h,0,0.03) direction at the (200) Bragg peak of the Mo for as-grown MgO films of different thickness. **(b)** In-plane lattice parameter as extracted by fitting the GIXD data for the as-grown(unfilled circle) and annealed film(filled circle) at different coverages. **(c)** Radial scan along the (h,0,0.12) direction at the (200) Bragg peak of the Mo for different MgO film thickness after annealing[176].

with increasing MgO coverages. Fitting this data with a set of Gaussian peaks allows to extract the in-plane lattice parameter of the MgO film for different coverages and annealing temperatures. In figure (4.6.b) the results of the fitting are shown for the as-grown and the annealed film. It is clear that annealing has a drastic effect on the relaxation of the film. As the lattice mismatch for the as-grown film is almost equal to the value of the completely un-relaxed film, it decreases to ∼1.5% for the annealed 2ML thick film. Already at this stage the relaxation mechanism is able to reduce the strain between the two materials significantly.

Annealing of the film also leads to the appearance of additional peak in the scans, shown in figure (4.6.c). These satellite peaks are assigned to the presence of the network structure of inserted planes. Extracting the periodicity of this network structure from the GIXD data gives a value of 61Å±1Å for the 25ML thick film. This value is in agreement with the value(55Å±5Å) found in STM.

Intermediate Coverage Regime 5-12ML

STM   Also at this coverage a closed and flat film is found in STM, whose global roughness decreases, due to a good layer by layer growth. However the morphology differs from the thinner films. The periodic network structure has disappeared almost completely and could be observed only in some rare cases in a very faint manner. The topography at this thickness is governed by rather large, flat and defect-poor regions, which are 5–10nm^2 in size. STM also reveals, that the film is still not fully relaxed at this stage, as a number of different defects are found in the surface. For instance, dislocation lines that separate the different flat regions from each other. These features straighten along the [100]- and [010]-directions of the MgO.

Secondly, screw dislocations are found on the surface, (figure (4.7(arrow)). The origin of these defects might be the coalescence of the MgO islands with an out-of-phase crystallographic relation, that nucleate already in the initial growth stage.

Both defects were found to be able to act as electron traps. The presence of trapped electrons could be hereby confirmed by scanning tunneling spectroscopy(STS) and Photon Emission STM, as discussed in section (4.1.4) and (4.1.5).

LEED   The absence of the periodic network structure in STM at this coverage is accompanied by the vanishing satellite structure in LEED. At these coverages the satellites are not distinguishable anymore from the central spot, indicating the flattening of the surface. However, the LEED spots still show a substantial broadening. Indeed a star-like structure
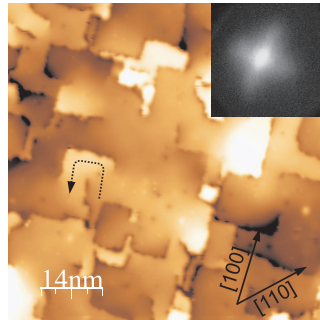
Figure 4.7: STM image of a 7ML thick MgO film. The surface show flat patches of $20nm^2$ to $50nm^2$ in size, edge and screw dislocations(dotted arrow).

with a four-fold symmetry evolves, which is now 45° rotated with respect to the splitting at lower coverages. Similarly to the *low coverage regime*, also in this case a fixed dependence for the spot-to-center distance is found, that suggests the presence of tilted regions induced by the screw dislocation observed in STM. It was not possible to obtain a distinct tilting angle from the LEED data at this coverages. This is explained by the fact that the screw dislocations produce an angular distribution of the surface patches, rather than just one fixed angle. Furthermore the screw dislocations have no long-range order on the surface and can not coherently interfere.

High Coverage Regime >12ML

Thicker films of coverages starting from 12ML were prepared only in a few cases and are therefore only rudimentary studied. The investigation by means of STM becomes more and more difficult for thicker films, since the fully evolved band-gap and hence a dramatically decreased conductivity. In the case of a 18ML thick film, shown in figure (4.8), this effect is visible by the noise and the poor resolution. In principle, only some step edges and dislocation lines remain visible. Those number however has decreased on the surface.
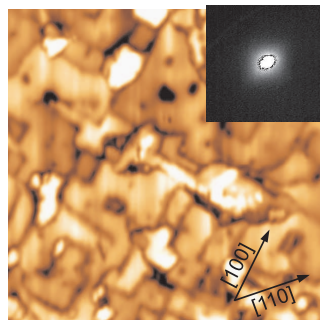

Figure 4.8: STM image of a 18ML thick MgO film. Stabilizing the tunnel junction at this coverages is difficult, because of the decreased conductivity of the film. The LEED pattern indicates an almost flat and defect poor growth of the film since only a simple 1×1 without any internal structure is visible.

The flat and defect poor character of thicker films becomes also evident from the LEED patterns. A purely (1×1) pattern without any satellite structures is observed in LEED, suggesting the absence of tilted regions on the respective surface.
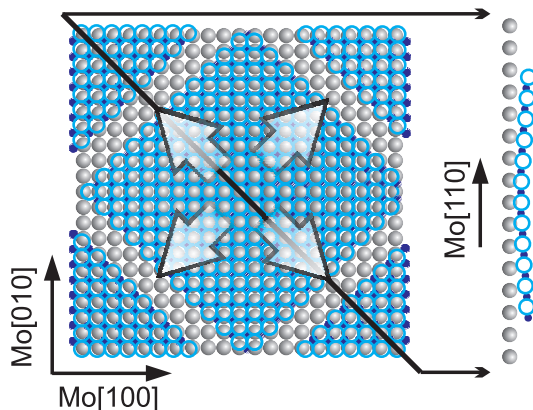
Figure 4.9: Growth model for sub monolayer coverage. The lattice mismatch of 5.4% prevents that atoms on the edges of the island are able to occupy preferred binding sites. As long as the coverage is below 1 ML the atoms avoid unpreferred site and a patched MgO film forms on the surface.

However the film is still not fully relaxed. Even at 25ML thickness, GIXD measurements reveal a residual expansion of the MgO lattice of $\sim$0.5% [176].

4.1.3   Growth Model

The most striking topographic feature of the MgO film is the presence of a pronounced network structure on the surface at lower coverages, that goes in line with a distinct satellite structure in LEED. The network structure disappears at a coverage of $5-6$ML and at the same time also the satellite structure in LEED vanishes. Since both features have a similar thickness dependence, they are likely to be of the same origin. In fact, both observation are explained by the relaxation behavior of the film, induced by the lattice mismatch of 5.4% with respect to the Mo substrate. This relatively large lattice mismatch at the MgO/Mo interface prohibits a pseudomorphic growth by simply expanding the MgO to the Mo value. The mismatch has to be overcome by other mechanisms. Only at the very early stage of growth(*sub-monolayer*), small MgO islands are able to occupy preferred binding sites on the Mo substrate without massive expansion and structural relaxation. The preferential binding sites at the Mo surface are the on-top position for oxygen and the hollow positions for magnesium[177, 178, 179]. Those sites can be occupied only at the beginning of the growth. With increasing island size, the effect of lattice distortion becomes larger and the O and Mg ions are forced to occupy alternative sites of the surface. This means, that the O is forced to move closer to unfavorable bridge and hollow sites. The same holds for the Mg ions, which have to occupy top and bridge sites with increasing distance from the perfect binding configuration in the center. Of course, one has to take into account the slightly expanded MgO lattice constant for thin films, as found in the GIXD investigations. Still a displacement of roughly 1,5Å is calculated for the atoms, that are 20Å away from the center. This, in fact is responsible for the growth of MgO patches of unique size(~ 50Å^2). The atoms in the MgO try to avoid unfavorable binding sites and the islands stop growing, leaving some space open.

However, increasing the coverage to more than 1ML, also the space between the patches fills, leading to a closed film. As described before, a pronounced network structure appears at this thickness, which shows almost the same periodicity($\sim$55Å) as the structures formed by the squared MgO patches at *sub mono-layer coverages*.

The squared network of bright lines might be interpreted as a Moirè pattern. Such a pattern

evolves, if two lattices with only slightly different lattice parameter are overlayed geometrically. This leads to the appearance of regions with low and high transmissivity, as depicted in figure (4.10). The Moirè structures in STM have a geometric and electronic contribution that often convolute in the images. Indeed the superposition of a fully relaxed MgO layer with a Mo lattice would lead to a network of a periodicity of 59,6Å, that is slightly bigger than the value found in the STM experiments, but still reasonably close. However, the experimental finding of tilted regions on the surface, as deduced from LEED is not explained by a simple Moirè construction.
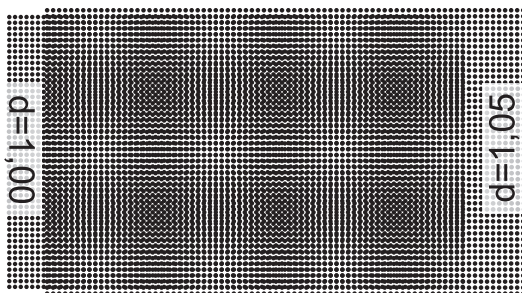

Figure 4.10: Moirè construction: the geometrical superposition of two lattices with a slightly different lattice parameter(1,00/1,05) leads to formation of dark and bright regions with the same symmetry than the underlaying structures.

To rationalize the observed structure it is crucial to take into account also the interfacial binding between the MgO layer and the Mo substrate. As already seen for the *sub mono-layer coverage*, the competition between occupation of preferred binding positions and the tendency to grow with the regular lattice constant, strongly affects the growth of the MgO. The restriction of the lattice parameter hereby forces the atoms to occupy unfavorable binding sites. Whereas this occupation is avoided during the formation of small islands at low coverage, this is not possible anymore at higher coverages. Therefore also unfavorable sites have to be occupied in the case of a closed MgO layer.

For a similar system, namely MgO on Pd, the dependence of the interfacial bonding strength was investigated theoretically by DFT[180]. It turned out, that a MgO layer on a Pd substrate would exhibit different binding lengths, if bounded to different positions on the substrate. For O on the preferred Pd top site the bond length is 2,38Å, whereas a Mg atom bound in a top position has a bond length of 2,96Å. That means, a MgO layer on a Pd substrate shows a rumpling of ∼0,58Å, due to the repulsive interaction between Pd and Mg. Transferring this finding to the MgO/Mo system means, that areas where unfavorable sites are occupied show a weakened interfacial binding and therefore have a larger separation to the Mo substrate.

Taking this into account a Moirè structure can be perfectly reproduced by overlaying the Mo with the MgO lattice with the slightly expanded oxide lattice constant obtained from GIXD. With this assumption one may construct a coincidence lattice that consists of 19 MgO unit cells over-growing 18 Mo unit cells. Such a structure has a calculated size of 56.7Å, in very good agreement with the periodicity extracted from STM-images.

In other words, the MgO film adapts to the substrate underneath by introducing one additional planes every ∼56Å and thereby sufficiently reducing the mismatch with the Mo support. But, since this additional plane changes the registry of the MgO lattice, its atoms expierence a reduced interfacial binding with the substrate and lift up at specific regions. Namely the positions were the O and Mg ions are forced to occupy unfavorable binding site. The larger bond length at this positions leads to the bright lines of the dislocation network and is confirmed by the observation of tilted areas in LEED. The fact that the bonding at
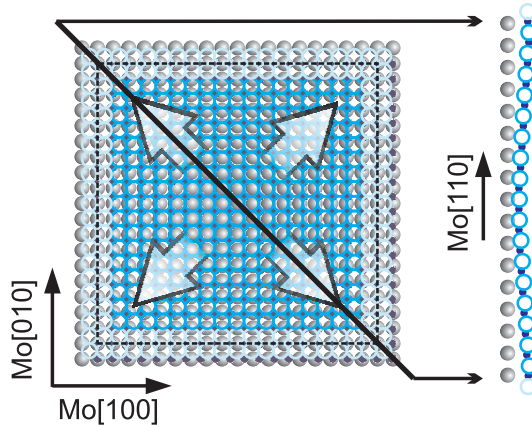
Figure 4.11: Growth model for the monolayer MgO film. The space between the MgO patches is filled and thereby unfavorable binding sites have to be occupied. The binding at such sites is reduced, which leads to a larger binding distance and therefore to the formation of tilted regions.

these sites is indeed weak is also confirmed by the frequent observation of point defects along these bright lines.

The growth model discussed here is able to explain the experimental results obtained from STM, LEED and GIXD. However this considerations mainly take geometric parameters into account and show that the bright lines of the network structure are at least in parts due to topographic relaxations in the oxide layer. STM measurements at different voltages have shown however, that the visibility of the network structure is enhanced at certain bias values. This suggests an electronic effect of the contrast formation in addition to the topographic contributions. Such electronic properties can be also probed by STM and will be discussed in the following.

4.1.4 Electronic Properties of MgO/Mo

An important electronic property of an oxide film is the gap between its valence and conduction band. This band-gap is known to change depending on the film thickness[181, 182]. Since the tunneling current in STM is depended on the LDOS of tip and sample, the presence of a band-gap can strongly affect the tunneling on such materials. Experimentally this means, that sufficient tunneling currents to stabilize the scanning are only achieved at biases above the respective value of the conduction band onset. This was clearly observed in the experiments, where the tunneling could be stabilized only for minimum voltages of around $3.0 - 3.7V$.

Furthermore STM offers the possibility to probe the LDOS almost independently from topographic effects, by Scanning Tunneling Spectroscopy(STS)[104, 105, 106]. Since this was not in the focus of this work, it should be discussed here only briefly. In equation (3.7) it can be seen that the tunneling current depends on the integral over the LDOS of the sample. By differentiation one can get back the LDOS. Hereby the term dI/dV is usually associated with the conductance and is given by:

$$\frac{dI(eV_s)}{dV_s} \propto \rho_s(eV_s) \cdot T(d, eV_s). \tag{4.1}$$

If the transmission function $T(d, eV_s)$ is constant, the differential conductance becomes pro-

portional to the LDOS ρ_s. Experimentally, various ways were established to obtain the differential conductance[183]. Commonly the "dV" is implemented by a Lock-In technique, that modulates the applied bias with a few tenth mV. The Lock-In signal than directly provides the differential conductance signal dI/dV. This technique was established first by Feenstra *et al.*[184]. The technique can be applied in a point-like manner, obtaining conductance versus biases curves at different locations on the surface or in a spatially resolved manner, where the conductance is mapped simultaneously with the topography at a constant bias.
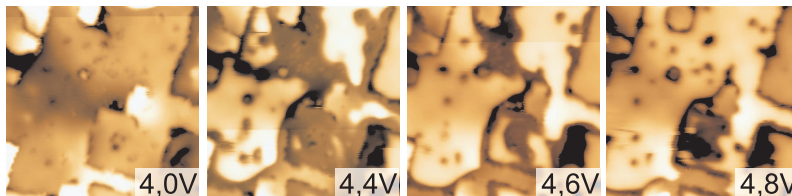

Figure 4.12: STM images of a 7 ML thick MgO film at the indicated biases. With increasing the bias bright areas appear on the surface, which grow in size until covering the whole terrace at $\sim 5V$. Such areas evolve because of the local availability of FER's as a new conductance channel.

The importance of the electronic structure for imaging becomes clear, when looking at the bias series in figure (4.12). Only slightly above the conduction band onset the tunneling is stable and the topography is not strongly affected by the electronic structure of the MgO. At roughly $4.3V$ the apparent topography changes and certain areas appear with larger contrast. This areas grow in size with increasing bias, until the whole surface is covered by these bright regions. The contrast change can not be explained by a topographic effect, but is a purely electronic phenomenon. The origin, becomes evident from dI/dV point spectra taken at different surface regions(figure (4.13.a)).

The simple picture of electron tunneling through a classically forbidden barrier gives an exponential increase in conductance for increasing the bias. Such a behavior is indeed visible in the dI/dV spectra, but superimposed by an oscillatory signal. A similar behavior was already observed for band-gap materials[185, 186]. It was interpreted in the framework of so called Field Emission Resonances(FER). The formation of these FER's can be understood by the scheme in figure (4.14) and is in detail described in Ref.[187, 188, 189, 190, 18]. If the bias applied to a tunnel junction approaches the value of the work function of the respective sample, the barrier, which the electrons have to tunnel through shows an important change. The slope of the potential leads to the formation of a region between tip and sample, that is not classical forbidden. That means that an electron does not directly tunnel from the tip, through the barrier into the sample, but also passes this region, which is restricted on the one side by the vacuum energy and on the other side by the potential step of the surface(figure (4.14)). This triangular quasi-potential defines the boundaries for the development of standing electron waves. The energy of these standing waves is given by the constrain, that the underlaying wavefunctions fulfill the boundary conditions of the potential, as known from fundamental quantum mechanics.

The first calculation of the eigen-energies for electrons in a triangular potential was done by Gundlach *et al.*[187], who also calculated the transport probability of such junctions. Hereby the energy position of the electron states in a triangular potential, depends on the work function Φ and the strength of the electric field F and is given by:

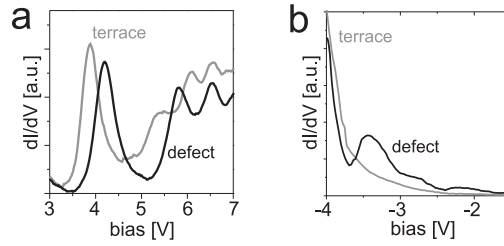$$E_n = \Phi + \left(\frac{3\pi\hbar e \cdot F}{2\sqrt{2m}} \right)^{\frac{2}{3}} n^{\frac{2}{3}} \tag{4.2}$$

Figure 4.13: **(a)** Differential conductance spectra taken at the terrace(grey) and a defect line(black). **(b)** A localized electron state is found in the conductance spectra taken at the defect line(black), whereas only the band onset is visible on the terrace(grey).

The oscillation in the conductance signal observed for a 7ML thick MgO film can now be traced back to Field Emission Resonances(FER). The opening of additional conductance channels is visible in STM by the appearance of bright areas at certain biases, indicating that a "new" FER is reached for electron transport for this particular region.

The observation of FER's on the MgO, offers the possibility to get insight into the local work-function distribution. The work-function is an important property of an oxide, since it influences the charge transfer behavior[179, 191, 192] and hence the chemical properties[193, 194, 195]. Statements on the work-function are possible, as the energy position of the FER's depends on the work-function of the surface(figure (4.14)). It is illustrated, that an increased work-function leads to a smaller slope of the triangular potential, that shifts the FER's to higher energies and decreases the distance between them. A lower work-function has of course the opposite effect.
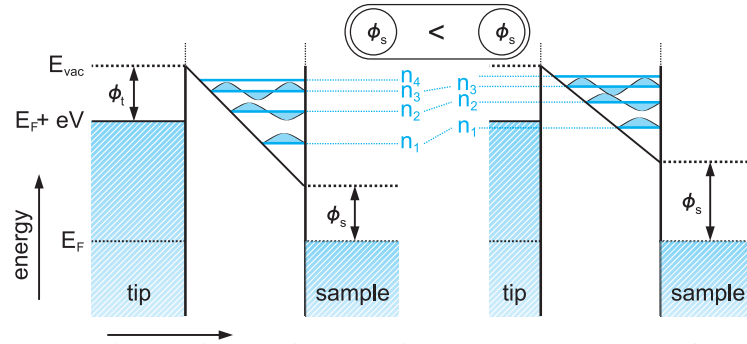

Figure 4.14: Scheme of the the formation of FER's in a tunnel junction. Quantized states form in the triangular potential defined by the vacuum energy(E_{vac}) and the potential step at the surface. ϕ_t and ϕ_s are the work function of the tip and the sample, respectively. On the right side the scheme is presented for a larger work function of the sample. This leads to the shift of the FER's to higher energies and reduces their energetic separation, as composed to the left side.

Summing up, the concept of FER enables the interpretation of the STM data obtained at higher bias voltages on oxide materials, as shown in figure (4.12). The 12ML thick MgO film imaged at $4.0V$ exhibits the usual morphology characterized by terraces of a few nm in size and a number of dislocation lines. The corrugation at this low bias is rather small and the edge dislocations have an apparent height of 2.5Å. The situation changes, if the bias exceed the 1st FER at around $4.3V$. Now the terraces become bright, while the lines defects stay dark. The actual height difference amounts to 7Å at an imaging bias of $\sim$5.0V. This contrast change implies that the first FER can be reached at this particular bias on the terraces, but not above the lines defects. Since the energy position of the FER's depends on the local

workfunction, it is an indication for a lower work-function of the terraces compared to the defects. Although an absolute determination of the work function is difficult, the relative differences in the local work-function can be directly observed in this way.

The interpretation, that FER's are not available at low bias on the line defects, could be confirmed by STS measurements at terrace and at defect sites(figure (4.13)). The dI/dV spectra taken at the different positions on the surface exhibit the oscillatory behavior, typical for the FER's. Taking such spectra at the lines defects and on the terraces clearly shows a shift in the energy position of the FER's. At defect sites the 1st FER is available only at a sample bias above $\sim 4.5V$, while it occurs at $\sim 3.8V$ on plain terraces. Furthermore, probing the conductance of the different sites, as show in figure (4.13.b), the presence of an additional state at the line defects becomes evident in the band-gap of the MgO. The substantial increase of the work function at the position of the defect lines is explained by the presence of additional electrons at these sites. The extra electrons produce a negative surface dipole that increases the work-function. The fact that such dislocation lines could act as a electron traps, was predicted by a theoretical work of Shluger $et\ al.$[196].

4.1.5 Optical Properties of MgO/Mo

To get more insight into the properties of the MgO films, they were also investigated with Photo Emission STM(PSTM). As mentioned in section (3.1.1) the stimulation of light emission can be done in a wide bias range. This range may be separated into two major voltage regimes, simply by the fact that the used electronics only provide voltages up to $15V$ for tunneling. Anyhow, imaging operation of the STM above this bias values is not reasonable, because of the poor resolution. Higher bias could be applied to the junction by retracting the tip and disable feedback loop and scanning. Thus electron energies of 50–$300eV$ could be reached(Field Emission Regime).

Optical Properties of MgO: Field Emission Regime   The electro-luminescence response of MgO films of up to 60 layer thicknesses is shown in figure (4.15). The electro-luminescence was excited with $200eV$ electrons. The acquisition time was set to 1 minute at a current of $1nA$, in order to minimize electron induced damage on the surface. Nevertheless, damages could not be completely avoided, although the effect seems to be small. This could be concluded from two observations. First, the spectra do not change even for longer acquisition times, which would be the case, if the surface would undergo dramatic changes upon electron bombardment. Secondly, the emission characteristic was also reproduced for much lower biases, where only the signal to noise ratio is much worse.

The spectra aquired in the field emission regime exhibit a similar characteristic for all different MgO coverages. Two emission bands at $287nm(4.3eV)$ and $400nm(3.1eV)$ appear in the spectra. Increasing the MgO film thickness does not change the overall spectral shape, but leads to an increased intensity for the two bands.

As already mentioned in section (2.2.1), this emission bands are assigned to the radiative decay of excitons at low-coordinated sites in the MgO surface. The excitons are created by the interaction of the O^{2-} ions at the surface and the injected electrons. Since these excitons are mobile[61], they are able to diffuse on the surface and become trapped at defect sites at which they decay via the emission of photons. The nature of these trapping sites is heavily discussed in the literature and either low-coordinated sites or oxygen vacancies(F-center) are considered. In this work the two emission bands are assigned to the exciton decay at 3-fold coordinated corner sites($3.1eV$) and 4-fold coordinated edge sites. This assignment is based on the work of Knözinger $et\ al.$[55] and is in good agreement with the experimental results. Nevertheless the presence of F-centers on the surface can not
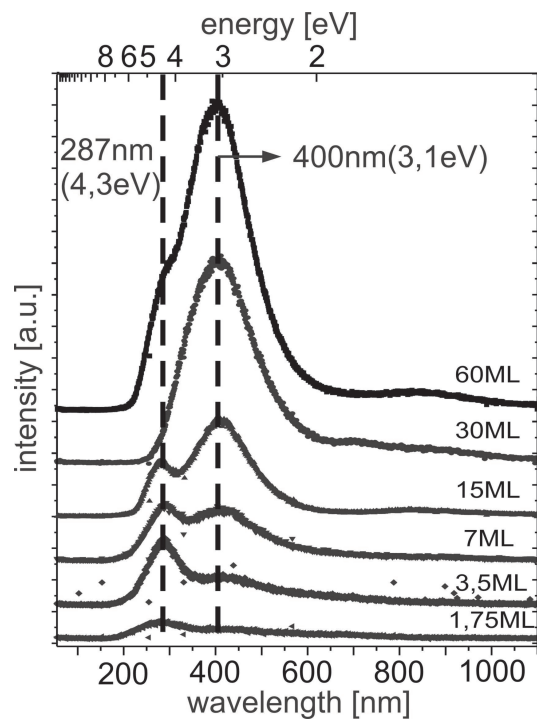
Figure 4.15: Thickness dependence of the light emission of a MgO film, stimulated by field emitted electrons($200eV$, 60sec, $1nA$. Two emission bands appear in the spectra, which are assigned to the radiative decay of mobile excitons at either 3-fold coordinated corner($400nm$) or 4-fold coordinated edge sites($287nm$)

be excluded from the experiment. However, even if F-centers are present, they seem to play only a minor role for the light emission of these surfaces. This was concluded by two experiments. On the one hand, additional F-centers were created by bombarding the surface with electrons(300V, 1mA, 10min), whereby O-ions desorb from the surface in an Auger-like process and leave behind oxygen vacancies. These additional F-centers should lead to an increased emission intensity, if they are responsible for the light emission. In fact, an decrease of the emission intensity was observed after such a treatment. On the other hand, also the reverse experiment, namely healing oxygen vacancies in an oxygen ambiance of $1 \cdot 10^{-7}$mbar did not result in a complete quenching of the light emission. Therefore the assignment of the optical active centers to the low-coordinated sites seems to be reasonable and F-center seem to be not decisive for the emission process.

This interpretation also explains the observed dependence of the emission intensity on the MgO film thickness. The radiative decay of excitons on the surface competes with a number of other non-radiative decay channels. The metal support itself provides many of these non-radiative channels, for instance via phonon coupling or Landau damping. The presence of the metal support therefore reduces the lifetime of the excitons significantly. If the film thickness is increased, the influence of the metal support diminishes and the radiative decay channel becomes more pronounced. The influence of the support seems to disappear at a film thickness of roughly 40 ML, since the emission intensity is saturated at this coverage and does not increase anymore. This critical thickness for saturation can be taken as a rough estimation of the interaction length for the excitons.

The identification of light emitting centers in the field emission regime is done only in an indirect way, ignoring the high spatial resolution of the PSTM. In the present experiment this is due to the rather high voltages that prevent a good resolution. Consequently the voltage was decreased to the tunnel regime($\sim$10V), in oder to probe the optical properties on the local scale.

Optical Properties of MgO: Tunnel Regime Surprisingly the emission bands found at elevated bias were not reproduced at lower values. The low bias photon emission is in fact very different and shows a pronounced dependency on the voltage. This dependence is depicted in figure (4.16). For a bias below 4.5V, almost no photon signal is observed. Starting at a critical bias value of 4.5V, an emission peak appears at 900nm(1.3eV). This single peak in the spectra is shifting to higher energies, when the bias is increased. However, a new peak at 700nm(1.8eV) evolves into the dominate feature in the spectra at 5.0V. This emission band differs from the 900nm peak, because it is almost constant in energy as a function of bias, but goes through a distinct intensity maximum at around 6.7V. A further bias increase leads to an intensity decrease of the 700nm peak, but results in the appearance of a third peak at around 500nm(2.5eV). Above 10V only some intensity is found in the range of 400–500nm, which is not clearly resolvable into individual peaks.

In contrast to the far-field emission regime, where the light emission is governed by the excitonic emissions, the emission below 10V seems to involve a number of different channels, which are active only in certain voltage ranges.

As a likely contribution to the photon response, FER's have to be considered, since they dominate the STM transport behavior at similar bias voltages where also the light emission is observed. Indeed, the emission from MgO films can be explained by taking these additional conductance channels into account[197, 198].

The only exception is the emission band at 900nm, that is neither related to the FER's nor to intrinsic emissions of the MgO or the silver tip. The observation of a blue shift of the emission with higher biases, thus higher electron energies, suggests the importance of inelastic tunneling effects for driving this emission. Such processes might be tip-induced
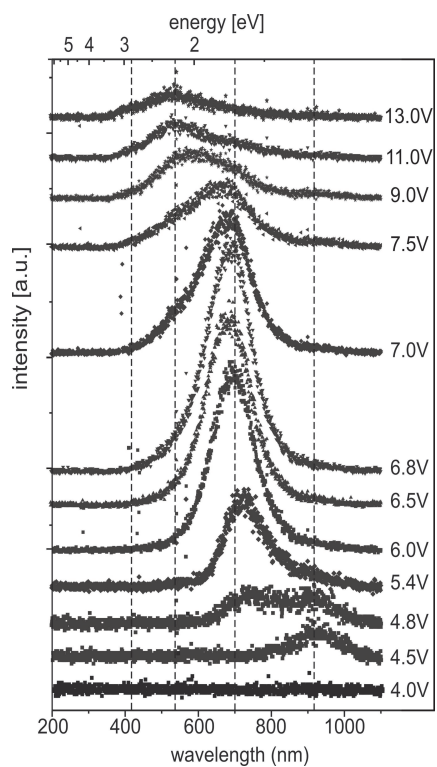
Figure 4.16: Light emission spectra for a 7 ML thick MgO film stimulated by electrons of the indicated energy($1nA$, 60sec). Four different emission band evolve with increasing the bias. Whereas the emission at $\sim 900nm$ is assigned to the formation of a TIP and the emission at 700, 500 and $400nm$ to radiative transitions between FER's.

plasmon(TIP) excitations in the Ag-tip/Mo-sample cavity. Calculating their resonance behavior with a simple electrodynamic model developed by Johansson *et al.*[126] results in a maximum that shifts from $900nm$ to $350nm$ with increasing sample bias($3 - 5V$). At the first glance, this seems to be not compatible with the experimental finding.

However the calculation only involves the tip and Mo sample, but neglects the oxide film in between. This additional dielectric material does not provide plasmon excitations by its own, because it lacks free electron density, but it substantially increases the polarizability of the whole junction. Therefore a shift to lower energies is expected, as known for example from investigations of metal particles in dielectric matrices[5]. Furthermore it is remarkable, that the $900nm$ light emission starts only at energies above $\sim4.5V$, which is an unusually high value for TIP's. It is nonetheless consistent with the excitation of TIP's on an oxide film, because the probability for TIP excitations by inelastic tunneling electrons strongly depends on the density of final states for the inelastic transitions. In the case of the MgO film, no states are available as final states, as long as the bias is below the conduction band(CB) onset. Therefore the emission only starts for voltages, higher than the CB onset plus the energy required to excite the TIP. The CB onset in the 7ML thick MgO film can thus be estimated with $E_{CB} = eU_{bias} - E_{photon} = 3.4eV$. Assuming a mid-gap position of the Fermi level, the band-gap of such a film would then amount to $\sim6.4eV$, which is smaller than the bulk value[47, 48, 50], but in good agreement with the value of $6.7eV$ found for the MgO surface[199, 200, 201]. The low-energy peak at around $800 - 900nm$ are however only a minor effect, as the emission response is clearly dominated by the $700nm$ peak. The evolution of this peak can not be described with the TIP-concept, because of its fixed energy position. It can be understood however, when taking into account the additional conductance channels related to the FER's. As shown before such resonances form in the classical part of the junction, if the bias is above the workfunction of the sample. Hereby the quantization conditions of the FER's are given by equation (4.2).

An electron in a FER has two possibilities to finally reach the substrate. First, it can elastically tunnel through the oxide film into the Mo in a direct way. Secondly it can undergo a transition to a lower state in the potential and than reach the substrate. The energy which is released by the transition to the lower FER is then emitted as a photon. The energy of the emitted photon is given by the difference between the involved states:

$$\hbar\omega = E_{photon} = E_m - E_n \qquad (4.3)$$

with n=1,2,... and m=n+1,n+2,.... Indeed, photon emission is observed when the bias reaches the energy of the second FER, which acts as the lowest initial state. The energy of the emitted light is then almost constant for increasing bias, since the energy difference between the FER's changes only slightly with bias. Furthermore the appearance of additional peaks at higher bias becomes understandable, as the electrons can occupy higher lying FER's, giving rise to additional transitions. Due to the limited spectral range of the detector system, not all possible emission lines could be observed, as they partly lie in the Infrared. However the emissions in the visible range can be assigned to specific transitions between the different FER's.

Applying the photon emission spectroscopy only in a point like manner gives insight into the bias dependence of the light emission. Spatially-varying parameters such as the workfunction cannot be probed. However, also this parameter determines the position of the FER's as revealed in equation (4.2). Therefore, spatially resolved photon emission spectroscopy was used to probe surface properties of the MgO film.

Photon-Maps The fact that the MgO workfunction is different across the surface was already observed by the dI/dV measurements(figure (4.13)). These conductance spectra revealed a shift for the energy position of the FER by $0.5eV$, measuring on a terrace or a line defect. This shift indicates an increase of the local workfunction for the line defects.

Also the light emission observed in the tunneling regime is related to radiative transitions between FER's. The fact that the energy position of these FER's depends on the workfunction of the sample, offers the possibility to probe these changes by optical means. The light emission should start first in the surface regions with lower work-function, since a lower work-function leads to lower energy positions of the FER's, according to figure (4.14). Such an effect is indeed observable in the spatially resolved photon emission(photon-maps).
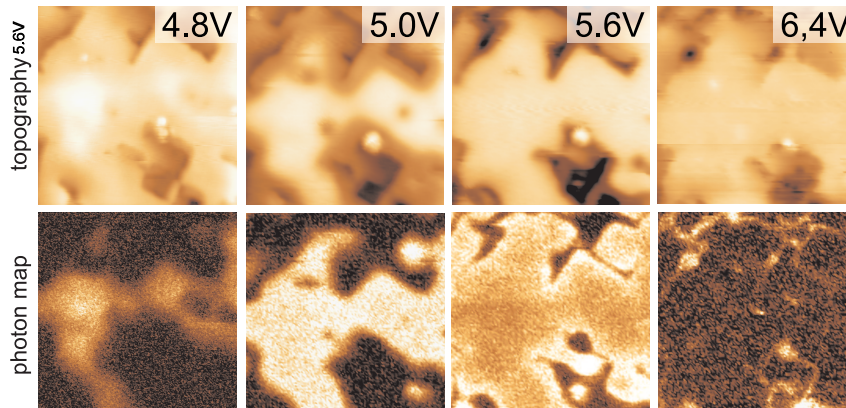

Figure 4.17: STM topographic images($40 \times 40 nm^2$, $2nA$) of a 7 ML thick film(upper row) and the corresponding photon map at the indicated bias. At $\sim 4.8V$ the 2nd FER is accessible on the terrace and light is emitted by radiative transitions. At $5.6V$ the condition for light emission is fulfilled almost on the whole terrace, but still the dislocation stay dark. For $6.4V$ the contrast has reversed, since now the FER's is reached also on the defect lines. The different energetic positions of the FER's hereby is explained by the locally different work function of the film.

Figure (4.17) shows the topography of a 7ML thick MgO film and the respective photon-maps for different bias values. Below the 2nd FER($4.7V$) no photon signal was measured, as the initial state for the radiative transition is not yet reached. The situation changes at $\sim 4.7V$, where the terraces start to emit light. In the beginning only the very central parts of a terrace becomes bright, while with increasing bias the bright regions expand until the whole terrace is bright at around $5.3V$. The dislocation lines however stay dark, even when the full terrace is already bright. Starting at $6.0V$, also these dislocation lines emit light, whereas the photon yield from the terraces has decreased. Finally at $6.4V$ the contrast in the photon-maps is reversed.

This emission behavior can be explained by the mechanism sketch before. The MgO layer itself lowers the workfunction of the Mo by almost $1.5eV$[182, 181], due to a suppression of the electron spill out at the Mo substrate and the creation of a positive dipole at the interface resulting from electron transfer out of the film. This lower work-function is reflected in the observation of light at $4.7V$, which corresponds to the value of the second FER on the terrace.
The line defects however do not emit light at this particular bias, indicating higher lying FER's. Apparently the work-function reduction at this site is weaker. This finding confirms the theoretical results of Shluger *et al.*[196], where defect structures(MgO domain boundaries) give rise to localized electronic states in the band-gap, that are able to trap electrons. Since the tunneling into the substrate is inefficient for large oxide thickness, the electrons are stabilized at this sites even in presence of the tip. The extra charge density at the surface introduces an additional negative dipole, which increases the work-function. Therefore the condition for light emission($eU_{bias} = E_2$) is fulfilled only at higher voltages of around $6V$.

The observation, that the terraces do not emit light at this bias anymore is due to the fact, that the next FER is not yet reached on the terrace.

Photon-maps mediated by FER-transitions therefore provide an effective way to probe work-function modulations on the surface of an insulating film.

The investigations discussed above provide a good understanding of the important properties of MgO films on Mo(001). Besides the morphological characterization also the optical response is rationalized. This detailed characterization allows to use these films as a support for the investigation of deposited metal particles. Hereby the knowledge of the specific properties is of crucial importance in order to be able to extract the particle induced response later. However, the fact that the excitons could be only excited at higher biases and the relatively large band-gap in general, make this film less promising for photo-catalytic studies and in particular to study the interactions of particles and excitons. In order to counteract this problems it was necessary to influence the optical properties. Therefore different systems were studied, that provide changed optical properties. First of all the optical response of the MgO film itself was rendered by means of doping. Furthermore, other metal oxide films were established, that provide different electronic and hence optical properties. Both approaches lead in addition to oxide films of different dielectric properties, which allow to study the effect of the supporting layer on the particle properties systematically. However, in order to start with such a systematic investigation it is of crucial importance to obtain a detailed characterization of these films before. Within this work such a investigation was started by studying the morphological and optical properties of lithium doped MgO films and by establishing calcium oxide and lithium oxide films as potential particle supports.

4.2 Li-Incorporation of MgO Films

Changing the electronic structure by introducing dopants is a well established technique in semi-conductor physics[39]. Tuning the electronic structure however, also changes the optical properties of the respective material. Referring to this strategy, the doping of MgO films with lithum was investigated in this study.

Besides the expected changes of the optical response, this system is in particular interesting for todays basic research in catalysis[21]. The Li-doped MgO is a potential catalyst for the oxidative coupling of methane[202, 203] and therefore studied as a model system to unravel the underlaying reaction mechanisms. Thereby one proposal, which was put forward by Jack Lunsford already several years ago[204] is debated in the literature.

Within this proposal the oxidative coupling of methane (OCM):

$$CH_4 + 1/2\,O_2 \rightarrow 1/2\,C_2H_4 + H_2O \tag{4.4}$$
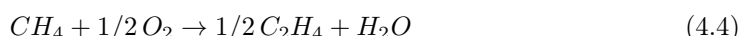
with ΔH$=139kJmol^{-1}$ at 800°C is discussed as the central point of the process, whereas hydrogen abstraction by O^{2-} is the key step of the mechanism. These O^{2-}-centers are supposed to be generated by Li-doping, resulting from the formation of Li^+O^--pairs. Lunsford *et al.* provided circumstantial evidence for the correlation between Li incorporation and chemical activity of the doped oxide by a number of different experiments[205, 20, 19]. On the one hand, $CH_3\cdot$ radicals were collected behind a Li/MgO-catalyst bed by condensation of the gas mixture on a cold finger and counted by means of Electron-Paramagnetic Resonance Spectroscopy(EPR). Thereby the $CH_3\cdot$ radicals were proposed to be formed upon dehydrogenation of methane.

In a second experiment, the Li/MgO material was annealed to 700°C in air or in pure O_2 and afterwards quenched at $77K$. After this treatment, the material was analyzed by EPR. A signal at g = 2.054 was hereby assigned to Li^+O^--pairs, although no evidence for the spatial proximity of the paramagnetic defects and the Li^+-ion could be provided. From these somewhat uncorrelated experiments it was concluded, that CH_4 molecules dissociate homolyticaly on the Li^+O^--centers into Li^+OH^- and $CH_3\cdot$ radicals. The latter would desorb into the gas phase and couple in a stoichiometric reaction, leading to C_2H_6 as the primary C_2-product($CH_3\cdot + CH_3\cdot \rightarrow C_2H_6$).

The preparation of Li-doped MgO films within this work might be compatible to get a more detailed view on the actual role of the Li for the proposed mechanism. All the experiments were hereby part of the excellence initiative "Unicat" of the Berlin universities and research institutes. Besides this temperature-dependent study of the morphology, it's likely to observe also changes for the optical properties of the film. In order to compare doped and bare MgO films, light emission experiments were performed in addition to evaluate such Li-induced changes of the optical response.

4.2.1 Morphology of Li-doped MgO films

Before the preparation of doped MgO films a series of experiments was carried out, where Li was deposited onto a bare 7ML thick MgO film. STM images for this experimental series are summarized in figure (4.18).

After the exposure of 1ML Li onto the bare MgO film at room temperature, the surface is found to be covered by islands of 30–50Å size(figure (4.18.a)). These island are usually 2 layers high and do not exhibit any order at the surface. If the sample is gently annealed to $700K$, de-wetting of the surface is observed in STM. The Li forms aggregates, which are
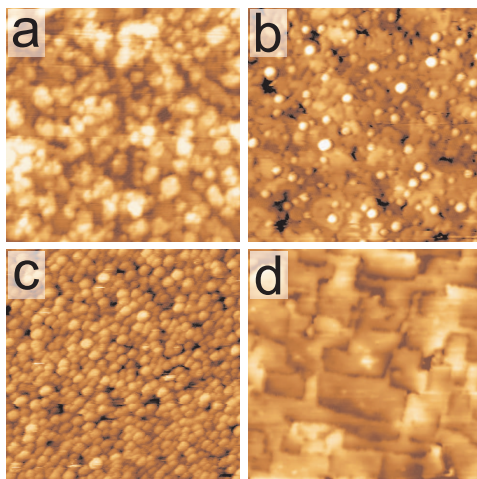
Figure 4.18: **(a)** STM image($75\times75nm^2$, $2,6V$)7 ML thick undoped MgO film covered with 1 ML of Li deposited at RT. **(b)** Preparation as in (a), but annealed to $700K$, which leads to a de-wetting and the formation of Li particles on the surface. **(c)** Surface topography after depositing 2ML of Li and annealing to $700K$. The increased amount of Li on the surface is reflected by the increased size and density of the Li particles. **(d)** If the annealing temperature reaches $1050K$, the particles desorb from the surface and the topography of the MgO is recovered.

10–15Å in height and around 25Å in diameter(figure (4.18.b)). The dislocation lines of the underlying MgO hereby serve as nucleation centers for these Li aggregates. This observation is in agreement with a combined calorimetry/DFT study[206, 207]. Here the experimentally found value for the heat of adsorption($2.6\ eV$) was explained by a preferential binding of the Li to kink($3.6eV$) and edge($1.6eV$) sites on the MgO surface. Furthermore, a large barrier for the up-step diffusion was found, resulting in a preferential growth of 2D islands at lower temperatures. Only close to the thermodynamic equilibrium 3D particles form, as their adhesion is 10% larger than for the 2D particles. At higher Li exposures(figure (4.18.c)) the size, as well as the density of the Li aggregates increases upon annealing, leading to a MgO surface which is almost completely covered by three-dimensional Li particles. These Li aggregates desorb, if the annealing temperature exceeds $1050K$. The bare MgO film is recovered and exposes again the known flat terraces. However, as proven by optical spectroscopy later, the Li does not completely desorb, but partly dissolves into the MgO.

Although this procedure seems already feasible to introduce small amounts of Li into the MgO, "direct" doping of MgO films turned out to be more suitable, as show in the following.

To establish doped MgO films two approaches were realized. First, simultaneous deposition of Mg and Li was performed in an oxygen ambiance of $5\cdot10^{-7}$mbar onto a clean Mo substrate. These films a referred to as doped MgO films in the following. The preparations were done at room temperature, followed by additional annealing steps. The atomic Li:Mg ratio was set to 1:5. Whereby the use of SAES dispensers as lithium sources enabled only limited control of the Li flux.

The second approach to incorporate Li into the MgO, is a sequential growth of MgO and Li_xO layers. This fabrication leads to sandwich structures, consisting of a 5ML thick MgO film at the interface, followed by 2ML of Li_xO and a 5ML thick MgO film at the surface. The room-temperature growth was again completed by an annealing step, which was applied to crystallize the structures.

Li-Doped MgO Films   Typical STM images of doped Li-MgO films for different annealing temperatures are shown in figure (4.19). Crystallization of the films sets in after a gentle annealing to $500K$(figure (4.19.a,b)). The STM images show almost the same topography as found for the bare un-doped MgO. Even the LEED pattern do not indicate any changes of the crystallographic structure. These observations suggest that the MgO film is able to store a fairly high amount of Li within its rock-salt lattice. Only a small amount of the material seems to segregate onto the surface, leading to small ad-particles of ~10Å height and ~20Å diameter. Such particles might consist of Li-O compounds, that could not be incorporated into the MgO film. A further annealing releases more of the Li, that was dissolved in the film before. Higher annealing temperatures thus result in films, that are covered with more and larger ad-particles(figure (4.19.c)). The particle size increases to a height of 15–20Å and a diameter of ~60Å. However LEED, still reveals the usual pattern of the pure MgO film with a slightly enhanced background intensity.

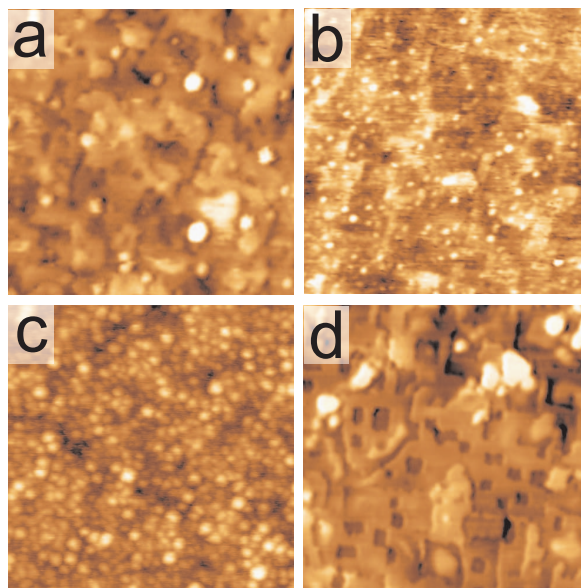Figure 4.19: **(a)**STM image($50\times50nm^2$, $5.0V$, $0.04nA$) of a Li-doped MgO film annealed to $500K$ indicating a topography very similar to the undoped MgO film. **(b)** Same preparation conditions as in (a) but with an increased amounts of Li($100\times100nm^2$, $5.0V$, $0.04nA$). In addition to the characteristic MgO topography small Li-containing particles are found on the surface. **(c)** STM image($100\times100nm^2$, $5.0V$) of the film after annealing to $700K$. The further annealing leads to the segregation of Li to the surface, forming larger particles. **(d)** Surface after annealing to $1050K$($50\times50nm^2$, $5.0V$). The Li particles are desorbed leaving behind rectangular holes in the surface.

Already at $500K$ annealing, changes of the bias-dependent contrast behavior were observed. For the un-doped MgO films the contrast is strongly influenced by workfunction modulations at the surface, mediated by FER's(section (4.1.4)). In particular the dislocation lines appeared dark at higher biases. Since these dark lines are not observed in the doped films anymore, it is suggested that the Li partly penetrates defect sites of the surface. As a result, the local workfunction modulations disappear. A homogeneous workfunction is even found for films that are annealed to elevated temperatures, when Li-aggregates already desorb($1050K$) from the surface. Thus it is concluded, that traces of Li remain in the rock-salt structure of the film, even for high-temperature annealing. These highly annealed films($1050K$) are furthermore characterized by 1ML deep rectangular holes, that seem to be left behind by the desorbing Li-aggregates.

Li-MgO Sandwich Structures   The preparation of sandwich MgO films essentially gives rise to the same experimental observations as the Li-doped films. Figure (4.20.a,c) shows

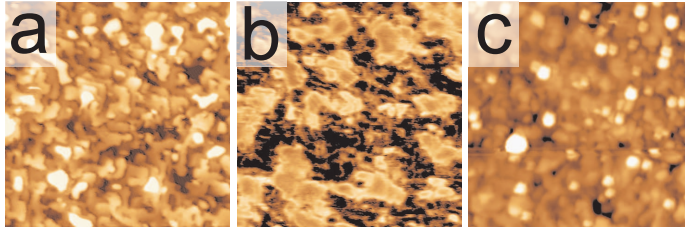typical topographic images of a 5ML MgO/2ML Li$_x$O/5ML MgO sandwich structure.

Figure 4.20: **(a)**Topographic images($75\times75nm^2$, $6.0V$, $0.05nA$) of a sandwich structure consisting of 5 ML MgO, 2 ML Li$_x$O and 5 ML MgO. **(b)** Conductance map($6.8V$) of a sandwich structure film, reflecting the different chemical composition by the appearance of distinct bright(high conductance) regions. **(c)** Film as in (a) but annealed to $700K$. Similar to the Li doped films, the Li start to segregate to the surface, where it agglomerates into particles.

Hereby the topography of the film is governed by a high density of small terraces(figure (4.20.a)), after annealing to $500K$. The Li-MgO mixing within these sandwich structures is not completed at this particular temperature, as indicated by dI/dV measurements shown in (4.20.b). The dI/dV image reveals rather large regions of different electronic properties, that can be traced back to a different Li/Mg ratio in a near-surface region. Such deviations in the chemical composition are be reflected in the LDOS and hence produce dI/dV contrast on the oxide terraces[208].

If the sandwich films are annealed, a very similar behavior is found as for the doped MgO films. Also in this case the crystallographic structure is dominated by the MgO rock-salt lattice, as no additional reflexes are detected in LEED. In analogy to the mixed films, the sandwich structure decomposes at elevated temperatures. At $700K$ Li-containing particles are observed on the surface, whereby the size and density increases with increasing temperature. Flashing the sample to $1050K$ removes these aggregates, leaving behind the flat MgO surface with the characteristic rectangular hole pattern.

Li-doped MgO Films: Discussion   To gain a better understanding of the growth and the thermodynamic stability of the Li-doped films, a DFT study was performed by Dr. S. Levchenko from the Theory department of the FHI. In the following, a brief summary of the results is given, whereas a more detailed discussion can be found in Ref. [209]. First of all the DFT study revealed, that the formation energy of a Li atom substituting a Mg(denoted as Li$_{\text{Mg}}$-defect in the following) depends on the initial Li concentration in the respective layer and furthermore on the position of the layer with respect to the surface. The formation energy was found to be lowest in the top most layer. Moreover, these defects are most stable, if the Mg/Li ratio amounts to a 50%:50% concentration, meaning that every second Mg is replaced by Li.

Furthermore it turned out, that the presence of such Li$_{\text{Mg}}$-defects strongly influences the stability of oxygen vacancies. The formation energy of F-centers is significantly reduced, if a Li$_{\text{Mg}}$-defect is in close proximity. This effect is indicated in figure (4.21), where the interaction energy between a Li$_{\text{Mg}}$ and an O-vacancy in the top layer is plotted versus the position of the Li$_{\text{Mg}}$-defect.

The increased vacancy formation probability is explained by changes of the electronic structure induced by Li$_{\text{Mg}}$-defects. Replacing the divalent Mg^{2+} by the mono-valent Li$^+$ results in a weakening of the Coulomb interaction with the O^{2-} and generates an acceptor state near the valence band of the MgO. This state can be occupied by electrons from the O-vacancy, leading to a $6eV$ smaller energy for the formation of a F^{2+}-center in the vicinity of a pair of Li$_{\text{Mg}}$-defects compared to a F^0-center. As each F^0-center contains two electrons,
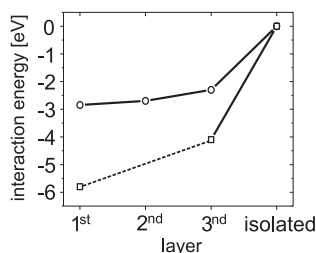
Figure 4.21: Interaction energy between a O-vacancy in the top layer and a Li_{Mg}(in different layers). F^{2+}-centers(squares) are more stable compared to the F^{+}-centers.

the formation of a Li_{Mg} pair plus one F^{2+}-center is energetically highly favorable.

The process of segregation can be understood by studying the defect concentration depending on the temperature. The starting point of the calculation is a MgO crystal with 12.5% Li dopage. At low temperature the concentration of Li-adatoms and O adsorbed from the gas phase is high and leads to the formation of Li_xO-islands. This islands correspond to the Li containing ad-particles that are observed in STM already before annealing. With increasing temperature Li_{Mg} defects diffuse to the surface and the concentration of O-vacancies increases. The most stable surface configuration is hereby the 50%:50% Li:Mg island, which develops in a broad temperature range.
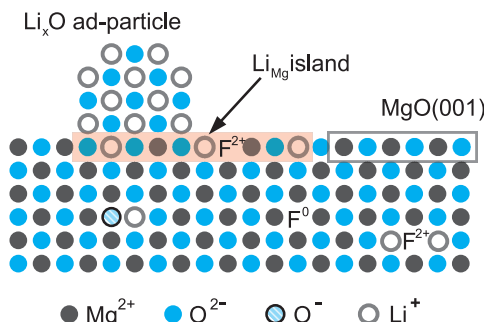

Figure 4.22: Surface and bulk structures related to Li-doping of MgO(001).

As a result, the film morphology changes with increasing temperature from the mixed Li-MgO structures to phase separated Li_xO-islands covering the surface. Only in the top most layer, mixed islands with 50% Li and 50% Mg are stable. A further temperature increase leads to the desorption of both, the ad-particles and the Li:Mg mixed islands. The desorption of the $Li_{50\%}Mg_{50\%}$ islands hereby leaves behind the distinct rectangular holes, observed in STM.

4.2.2 Optical Properties of Li-doped MgO Films

The optical properties of the respective films are investigated by means of PSTM in the *field emission regime*($200V - 250V$, $1 - 3nA$). First of all, the bare MgO films covered with Li islands were studied.

Li-covered MgO Films   The results are summarized in figure (4.23). It is evident from the comparison of bare MgO spectra with Li-covered spectra, that Li-dosage almost completely quenches the intrinsic MgO emission bands. This can be understood from the topographic images obtained with STM. Li agglomerates into small particles on the surface, that nucleate preferentially at defects and dislocation lines. The Li hereby blocks the low-coordinated edge and corner sites. Since these sites are responsible for the light emission of the MgO, it becomes understandable that Li dosage suppresses the MgO emission bands. Moreover, this result provides additional evidence for the involvement of the low-coordinated site in the light emission from the MgO.
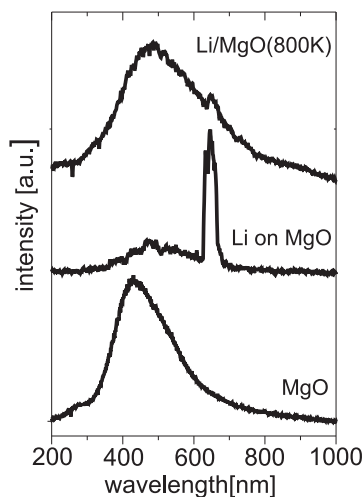

Figure 4.23: Photon emission spectra taken at $200V$ and $1nA$. The lowest spectra shows the typical exciton mediated emission band of the undoped MgO film. This emission is quenched, if Li is deposited onto the surface, because the optically active sites are blocked. The spectra is dominated by the Li D-transition(see text). Annealing to $800K$ recovers the optical properties, because the Li is desorbed. A fraction of Li ad-layer also diffuses into the film, which results in a red-shift of the broad emission band.

However the spectra of the Li-covered films show a very sharp and intense peak at $640nm(1.9eV)$. The sharpness of this emission is very unusual for excitonic or plasmonic excitations within a tunnel junction. The Full Width at Half Maximum(FWHM) of $\sim$90meV is only compatible with an optical transition of a gas phase species. In fact this emission line is explained by a radiative transition in gas-phase Li. For alkali species at surfaces it is well known that electron injection can efficiently induce the desorption of the respective species[210]. The desorption process is closely linked to the neutralization of the ionic Li by the injected electron. The neutral Li, which was stabilized by the Madelung potential of the ionic lattice before, is now only weakly bound to the surface and can easily desorb at thermal energies. The desorbed Li in the gas-phase is then excited by a second electron. It turns out that for a Li atom the most probable transition is the one from the $1s^2 2p^1$ to the $1s^2 2s^1$ configuration, being associated with an energy of $1.85eV$ or correspondingly to a wavelength of $\sim$670nm. The value found in the experiment($640nm$) can be related to this process, if the Stark-shift induced by the high electric field in the tunnel junction is taken into account.

The appearance of this sharp emission line is therefore associated with Li on the surface or in the first layer. Thus the spectra taken at an annealed($800K$) film has to be interpreted as follows. Since the sharp $640nm$ peak is still present in the spectra, it is concluded that

few Li-containing species are still on the surface. This conclusion, is confirmed by the STM investigation. Furthermore the intrinsic MgO emission band has recovered, indicating the desorption of most Li-containing patches from the surface. However, careful analysis of the spectra reveals a slight red-shift of the emission band. This shift is assigned to the presence of Li which has dissolved in the MgO film, as concluded from the optical investigations on Li-doped films discussed next.

Li doped MgO The diffusion of Li into the MgO at higher temperature was already suggested from the vanishing bias-dependent contrast of the dislocation lines. In addition, optical spectroscopy clearly reveals such a diffusion process, as indicated by the shifted MgO emission line. The optical properties of bare, doped and the layered Li-MgO films are summarized in figure (4.24).
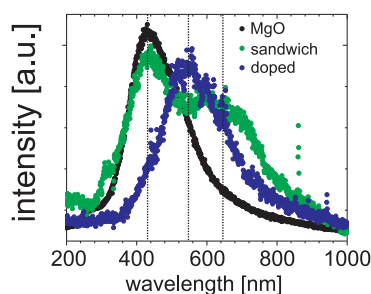

Figure 4.24: Photon emission spectra($200V$, $1nA$, 60sec) of different MgO films. The emission of the undoped MgO(black) is shifted to smaller energies with the Li doping. In the case of the sandwich structure(green) the separation of the different phases is visible by two distinct emission band, whereas the doped film(blue) only shows the red-shifted band.

In the case of the Li-doped films(blue curve) a clear red-shift of the MgO emission band is evident. This shift from $400nm$ to $\sim 550nm$ is induced by the Li incorporation. The red-shift compared to bare MgO is explained by the presence of Li mediated impurities in the MgO. Such impurities provide states in the band-gap, that act as traps for excitons. The excitons recombine at these sites and emit photons of lower energies. The low-coordinated edge and corner sites are not reached anymore.

The actual position of the emission peak in the doped MgO is slightly changing with the amount of Li incorporated into the film. This is most drastically seen for the sandwich structures. The optical response is hereby governed by the presence of two emission bands, namely a band at $400nm$ and a band at $650nm$. The high-energy band is hereby assigned again to the well known intrinsic MgO emission. The second line indicates the presence of another chemical entity, as already suggested from the dI/dV measurements. This strongly red-shifted emission is assigned to regions in the film, where the actual Li-concentration is high. This interpretation is confirmed, when the sandwich film is annealed. Afterwards, only one band is observed in the spectra, that is localized in between the two former bands and indicates an efficient intermixing of Li and MgO in the film. The actual position of the emission band of a particular Li-doped film can therefore be used as a measure of the Li amount dissolved in the MgO.

In summary the doping of MgO films with Li could be realized experimentally and was found to be one possibility to change the optical properties of the oxide film. In future experiments, not only the physical properties of Li-doped of a MgO will be explored. The emphasis will shift to the chemical performance, in particular to the ability of Li-doped MgO to promote oxidative coupling of methane. From the model systems presented here a

more detailed understanding of the actual reaction mechanisms is expected. Such chemical studies of Li-doped MgO will be performed in collaboration with the Inorganic Chemistry Department of the Fritz-Haber Institute.

4.3 Other Metal-Oxide Films: CaO and Li$_x$O

Doping of the MgO films is one way to tailor the optical properties, in particular the exciton excitations of oxide materials. Within this work also another approach was established; namely the preparation of other metal-oxide films with different band-gaps. The focus hereby lies on two important aspects. First of all, the band-gap, which has to be overcome for excitonic excitations, can be tuned to change the optical properties. The optical absorptions of a band-gap material are also closely connected to its photo-catalytic properties, since electron-hole pair generation hereby is a crucial step. Secondly, different support materials for metal-particle deposition open the possibility for a systematic investigation of particle-support interactions. By comparing the growth behavior and optical response, it might be possible to deduce the influence of the dielectric and chemical properties on the performance of an oxide material.

As a starting point for such studies, a preparation procedure for calcium oxide(CaO) and lithium oxide(Li$_x$O) was established and shall be discussed in the following.

4.3.1 Growth of Calcium Oxide Films

CaO as thin film material was chosen for a number of different reasons. First of all, CaO crystallizes in the rock-salt structure, as MgO, and owns the similar structural properties(section (4.1)). Thereby the (001)-plane was found to be the most stable surface termination[211, 212]. The lattice parameter of CaO is $486pm$; almost 15% larger than for MgO. Thus the lattice mismatch with the Mo substrate amounts to 8.1%(5.4% for MgO). Therefore the actual growth behavior might be very different. Furthermore CaO exhibits similar physical properties as MgO, for example the same high melting temperature($\sim 2800K$), which allowed to transfer preparation parameters from the well established MgO preparation. The chemical properties, of CaO on the other hand are rather different as the oxide is more basic and hence more reactive than MgO.
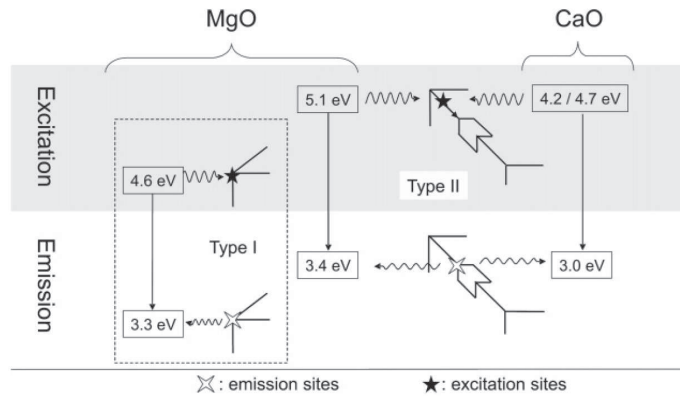

Figure 4.25: Scheme of the luminescence light emission for MgO and CaO taken from Ref. [55]. The CaO hereby only exhibit one emission band at $3.0eV$, which can be excited at $4.2eV$ and $4.7eV$.

Considering the optical properties, also CaO is a wide-gap insulator. Its band-gap is however "only" $6.3eV$, which is $1.5eV$ smaller than the one of MgO. According to studies of Knözinger *et al.*[55] the luminescence characteristic shows distinct similarities to MgO, whereas excitonic excitations are found at energies of $4.2eV(295nm)$ and $4.7eV(264nm)$. These excitations are assigned to less-regular oxygen-terminated corners and four-fold coordinated anions on edges. The emitted light of $3.0eV(413nm)$ originates from the deactivation of

mobile excitons at defect sites(figure (4.25)), e.g. corners and kinks.

Since the excitation energies are reduced compared to MgO, the investigation of excitons by means of PSTM might be feasible for thin CaO films.

Preparation of CaO   As already mentioned the preparation of CaO was adopted from the well established procedure for MgO films. All depositions were done on the Mo(001) substrate, that was cleaned before by several sputter/flash cycles(section (4.1.1)). After checking the substrate quality by LEED, the CaO film was prepared by evaporation of Ca from a Mo crucible heated via electron bombardment. Hereby the substrate was held at room temperature and biased with $+400V$, in order to avoid high energy Ca ions to hit the surface. The Ca flux was adjusted to approximately 1ML per minute and the depositions were done in an oxygen ambiance of $2 \cdot 10^{-7}$mbar.

After the deposition LEED indicates only a diffuse and almost featureless pattern, which suggest a poor long-range order. Consequently, the film was post-annealed to different temperatures to stimulate crystallization. In fact the best LEED pattern indicating the highest film quality was observed upon annealing to $\sim 1100K$ for $10min$.

Morphology of CaO Films   Using this preparation procedure, CaO thin films of different thickness could be prepared, as shown in figure (4.26). As expected the observed morphology of the CaO films shows some distinct similarities to the experimental findings made on MgO. However, important differences are observed as well.
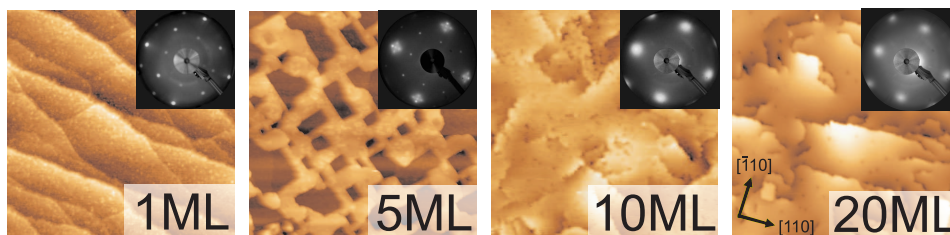

Figure 4.26: STM images and the corresponding LEED patterns of CaO film of different thickness. All films are prepared at room temperature and post-annealed to $\sim 1100K$.

Starting from the first ML the CaO is found to cover the whole Mo surface. At this thickness the film grows pseudo-morphic onto the substrate, which is indicated by the sharp LEED pattern that only shows the spots corresponding to the Mo lattice constant. In addition, LEED also exhibits a pronounced (2×2) super-structure, which fades away, if the coverage increases. In the STM a complete wetting layer of $2-3$ML thickness is formed first. Above 4ML coverage, no closed film but the formation of 3D CaO patches and islands is found. This morphology change is also seen in LEED. At 5ML, additional spots with a (1×1) structure emerge next to the (2×2) spots. Those spots are diffuse for weakly annealed films but show a distinct satellite structure upon healing to $1100K$. With increasing coverage the (2×2) disappears and the (1×1) spots become sharper. The (1×1) LEED pattern hereby corresponds to the bulk-like CaO lattice structure.

Discussion

The observed CaO growth behavior can be explained within the Stranski-Krastanov model. Hereby the lattice mismatch between the CaO film and the Mo substrate is of crucial importance. Since the mismatch amounts to 8.1%, the CaO film experiences a large compressive
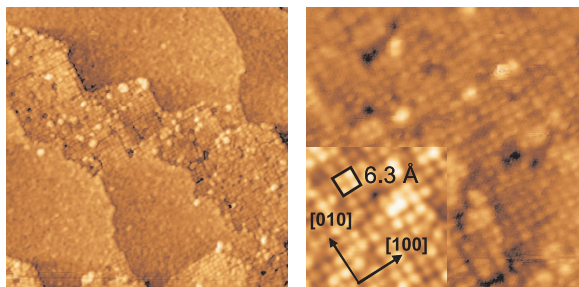
Figure 4.27: Topographic images of CaO films of 2ML thickness($100\times100nm^2$, $1.2V$, $0.04nA$). On the left hand the (2×2) structure together with some un-resolved pattern is seen on the surface. On the right-hand($30\times30nm^2$), the crystallographic directions of the Mo, as well as the size of the super-structure is indicated. The squared cell of 6.3Åsize is thereby close to two lines the Mo(1×1) unit cell.
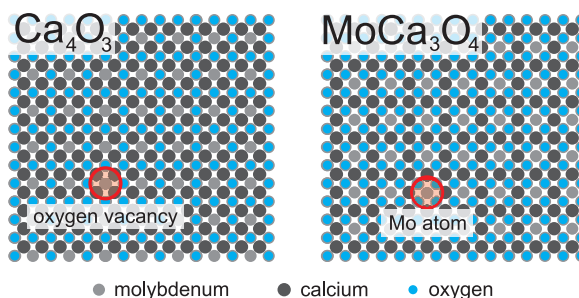

Figure 4.28: Calculated model geometries of a CaO 2×2 super-structure. The super-structure is either formed by missing O-atoms(Ca_4O_3 - left) or substituted Mo-atoms an surface alloy($MoCa_3O_4$ - right).

strain while growing on the Mo. In order to release this strain, a wetting layer that is not pure CaO is grown in registry with the underlying Mo lattice. This layer by layer growth transforms at a initial thickness into a CaO island growth with bulk like lattice parameters.

The wetting layer hereby shows a clear (2×2) structure, which is also visible in the STM images(figure (4.27)). These images clearly indicate an alignment of the new unit cell with the [010]- and [100]-direction of the Mo substrate. The size of the super-structure unit cell is ~6.3Å, as measured with STM. A likely reason for the development of this super-structure is the large lattice mismatch, which prevents the occupation of all atomic sites of the usual CaO lattice. The relaxation of the film to its bulk lattice parameter is done either by leaving atomic positions open or by substituting Ca^{2+} with Mo^{2+} ions from the support. In both cases a (2×2) super-structure forms. At this stage, the contrast in the STM images can not be assigned to a particular atomic species. Therefore it is not clear, whether the bright spots are O-vacancies, Ca-ions or Mo-ions. These questions have to be answered in future experiments and in collaboration with theory. Preliminary theoretical results from the group of Prof. G. Pacchioni from the university of Milan are already available. Two different models geometries are debated here. In these two models, shown in figure (4.28), the (2×2) super-structure is formed either by a network of missing O, leading to a Ca_4O_3 stoichiometry of the film, or by the formation of a $MoCa_3O_4$ surface alloy, where the bright protrusions would be the Mo-ions. In order to discriminated between these two possible models more theoretical calculations have to be done, which need to be accomplished with experimental STS and photo-electron spectroscopy data, for example.

At higher coverages the film morphology exhibits clear similarities with the MgO films. For instance, the development of a distinct satellite structure was observed in LEED as for MgO films. Its origin is traced back to the formation of tilted planes on the surface(mosaics). The
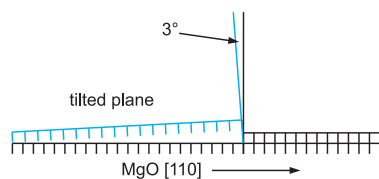
Figure 4.29: Schematic representation of the growth of tilted planes on the CaO interface layer to reduced the lattice mismatch.

formation of tilted regions is hereby a possible mechanism to reduce the lattice mismatch. Schematically this is shown in figure (4.29). By growing the next CaO patch not planar onto the wetting layer but by introducing step dislocations, the CaO lattice is able to grow with almost its bulk lattice parameter and does not have to adapt to the underlying registry. Since the tilting of the mosaics($\sim 3°$) is oriented along the [$\bar{1}$10]- and the [110]-direction of the CaO, also the satellite spots in LEED orient in this directions. If the thickness of the CaO film is further increased the tilting flattens out and the corresponding spot-structure develops into one single peak. At this higher coverages($>$10ML) also the morphology of CaO in the STM is rather similar to the known MgO morphology. Large terraces form, which exhibit a number of defects, consisting most likely not only of single missing atoms, but of larger holes. Moreover, step edges can be found, that mostly align with the CaO [$\bar{1}$10]- and the [110]-direction. The presence of these dislocations indicates, that strain still affects the growth and the film is not fully relaxed even at higher coverage.

The preparation procedure for CaO films and the analysis of its growth parameters is certainly only the starting point for a more detailed investigation of this system. This could however not be done within this work anymore. Future investigation will focus on the optical properties of these films, their adsorption behavior for metal particles and molecules. These studies might offer a better understanding of the particle-substrate interactions, in comparison with the well-studied MgO system.

4.3.2 Growth of Lithium Oxide Films

The second oxide thin film studied in this context is lithium oxide(Li_2O). It has attracted considerable attention for example as a blanket material in fusion reactors, for applications of solid-state batteries or for the production of conductive glasses[213, 214, 215].

Li_2O crystallizes in the anti-fluorite structure(figure (4.30)), which is related to the fluorite structure, but with Li-cations substituting the fluoride-anions and oxide-anions substituted calcium. It has an lattice constant of $462pm$ and a melting temperature of $1840K$. Although it has been studied experimentally and theoretically in terms of lattice dynamics[216, 217], defect formation[218] or conduction properties[219], its luminescence properties are only sparsely investigated. The lowest exciton absorption band was found at $7.02eV$[220], whereas other bands could be only observed after the creation of lattice defects by γ-rays[221], He^+-ions[222] or neutron irradiation[223]. Hereby emission bands at $4.7eV(264nm)$ and $4.13eV(300nm)$ were suggested to be intrinsic in nature and bands at $3.7eV(335nm)$, $3.3eV(375nm)$ and $2.87eV(430nm)$ are attributed to F^+-, F^0- and F_2-centers. A more recent work, performing luminescence measurements on Li_2O single crystals, found the two intrinsic luminescence bands at $3.7eV$ and 4.75[224]. They could be assigned either to the radiative decay at defects and impurities or to the the decay of self-trapped excitons, described theoretically by Shluger and Itoh[225].
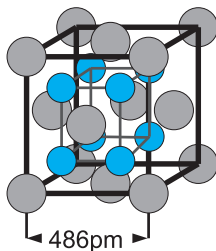

Figure 4.30: Anti-fluorite crystal structure of Li_2O with the Li-atoms(grey) constituting a fcc-structure and the O-atoms(blue) arranged in a cubic structure in the center.

Growth of Li_2O   The Li_2O films were prepared on the Mo(001) substrate, which was cleaned by the usual sputter/anneal cycles first. The deposition was done at room temperature, evaporating the Li from a SAES dispenser($6.3A$) in an oxygen background pressure of $\sim 2 \cdot 10^{-7}$mbar. After the deposition the sample was annealed to different temperatures in order to promote crystallization. The quality of the preparations was evaluated by means of LEED and STM. A summary of the experimental results for $\sim$2ML nominal Li coverage and different annealing temperatures is given in figure (4.31).

At low annealing temperature the Li_xO forms small particles, that completely cover the Mo surface. In LEED, as well as in the corresponding STM images, no indication for a long-range order is found, as the LEED pattern only reveals a diffuse background and the spots of the Mo substrate. Although, also larger agglomerates are observed occasionally, the particles usually have a diameter of $\sim 2nm$. This surface morphology is found until the annealing temperature exceeds $600K$. At this temperature the particles form regular structures on the substrate, although their are still separated from each other. If the temperature reaches $\sim 800K$ the morphology of the surface changes again. It is now characterized by atomically flat patches that initially form at the steps of the Mo substrate. The LEED pattern at this preparation condition clearly indicates a (2×2) super-structure, which was not observed for lower annealing. Since the formation of flat patched films was found for this annealing treatment, the thickness dependent investigations were done by maintaining these conditions.
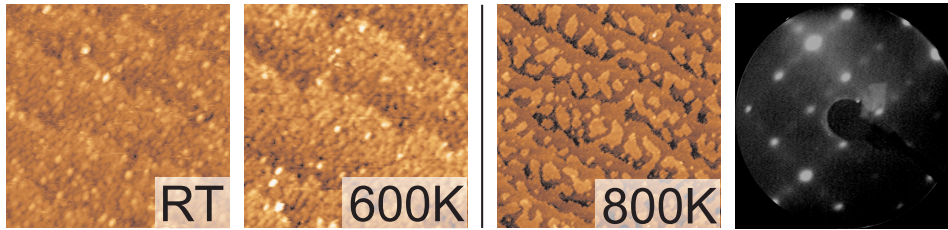
Figure 4.31: STM topographic images($100 \times 100 nm^2$, $0.04 nA$) of a Li_xO film of 2ML nominal thickness post annealed to the indicated temperatures. Below $800K$ the surface in completely covered by small particles. At higher annealing temperatures flat patches start to form, that are crystalline. The LEED pattern(right) for this preparation conditions indicates a (2×2) super-structure.
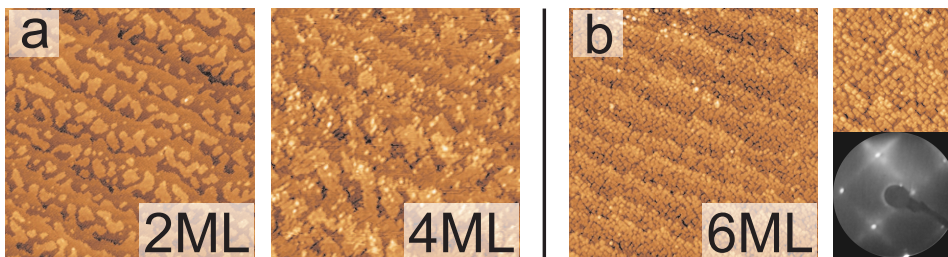

Figure 4.32: **(a)** STM images of the Li_2O morphology for different nominal Li-coverages and a post annealing temperature of $800K$. **(b)** Zoom of the 6ML topography, indicating the particle network and the corresponding LEED pattern, showing no 2×2 super-structure spot, which were present at lower coverages.

The corresponding STM images of Li_xO films of different thicknesses are shown in figure (4.32). At a nominal Li-coverage of 2ML the patched films are found again. Increasing the Li-dosage to ∼4ML results in a very similar surface morphology. The Li_xO forms large patches with small features found on-top of the patches. These extra features, do not form an additional layer, but can be characterized as small particles, with $2nm$ diameter. At this conditions, STM still reveals the stepped surface of the Mo substrate. For a nominal Li coverage of 6ML, the flat, patched surface morphology disappears and the film is completely covered with small almost equally sized protrusions, as show in figure (4.32.b). These protrusions have a square-like shape and an edge length of around $1.5nm$. Furthermore they are aligned with the [100]- and [010]-directions of the Mo, leading to a quadratic network structure. At this point of the investigation it is not clear whether these protrusions are purely topographic features or comprise in addition an electronic contributions.

The small particles are expected to grow on-top of the initially formed interface layer, which has grown pseudo-morphic onto the Mo. The fact, that only the interface layer exhibits a superstructure was also found for the CaO and might reflect the relaxation of the Li_xO film. The particles might be understood as stoichiometric Li_2O particles which are not able to wet the interface to the Mo(001) due to the lattice mismatch(4%).

However, models for the interface layer of CaO also assume the possibility of an surface alloy. Hereby, the fact that for Ca and Li deposition a (2×2) super-structure was observed might be interpreted by a general tendency of the Mo to form an alloy structure in the presence of small amounts of metal and oxygen and relatively high temperatures. Especially for Li, where the superstructure was visible even at higher nominal coverages, this might be the case. The associated class of materials are the molybdates. Many stable compositions are known between Mo-Ca-O and Mo-Li-O. To understand the real surface composition, chemical sensitive measurements are required such as XPS, UPS or NEXAFS. Those measurements are however beyond the scope of this work.

To finally answer these question, it is however necessary to perform more experimental work

on this system, which would also allow to get a more detailed insight into the interesting and rarely studied optical properties.

Chapter 5

Metal Particles on MgO Films

Metal particles are known to show catalytically interesting properties. Especially, in heterogeneous catalysis they are subject of intensive studies already for a couple of decades[226]. The substantial influence on the chemical activity of a catalyst is hereby depending on a numerous number of parameters. Besides the chemical identity of the particle, also the actual size and shape can induce dramatic changes of the chemical behavior. This was shown for instance in the case of Au particles by Haruta *et. al.*[227, 228], where an increase of the Co oxidation is observed, if the gold is dispersed into small particles onto an oxide material. Furthermore the interactions between the support material was found to be of crucial importance, as seen for Au on MgO[179], where a charge transfer into the Au appears, which depends on the actual thickness of the supporting layer. This particle-support interactions can actually lead to extremely different chemical activities. However, the optimum catalytic performance is usually achieved only for a specific combination of particle and support material. Such a combination is characterized by parameters like particle size, film thickness or defect structure. Further restrictions for an application as a potential catalyst are given by the thermodynamic stability, the suitability of fabrication, as well as the actual material costs. Therefore the development of promising catalytic application is linked to the understanding and the control of these properties. In particular surface science techniques offer a tool to answer this questions. This section thereby mainly focus on two aspects out of this broad discussion.

On the one hand a number of different metal particle-oxide system were prepared. Whereby a number of different metals was used, keeping the oxide film at always the same conditions. This was done to determine the growth behavior of the respective particles. Furthermore the constant properties of the support, allow to compare the different growth modes and enables to extract intrinsic material parameters, controlling the growth.

On the other hand, the optical response of these supported metal particles was investigated. This optical response is of crucial importance for photo-catalytic applications. Common questions which have to be addressed in this context, regard the influence of particle size, shape and material, as well as the properties of the support, on the actual optical properties. The Photon STM is perfectly suited to investigate this kind of question by probing the light emission characteristics of single particles in an energy- and spatially resolved manner.

According to these two main questions the following discussion is divided into two main parts, concerning the growth behavior of the different metals on the MgO support and the optical response of these systems.

The second part, focusing on the mechanism of light emission, is divided further into two subsections. A section which describes the optical properties of the energy-resolved investigations in the *field emission* and *tunneling regime* and the second part presenting the spatially resolved measurements.

5.1 Growth of Metal Particles on MgO Films

The growth of metal particles on surfaces and in particular on oxide surfaces is described in detail in the literature[229, 230]. Therefore only some important points shall be introduced in the following.

In this work the metal particles are produced by metal vapor deposition, where the metal is evaporated into the gas-phase. This beam of atoms arrives at the substrate surface, where the particle formation takes place by agglomeration of single atoms. Hereby the oxide film serves as substrate and the properties of this film therefore influences the growth. At an initial stage, this influence determines the nucleation process. Particle nucleation is heavily affected by the defects, like missing atoms or low-coordinated sites, which serve

as preferential nucleation centers for the atoms. Actually, this nucleation behavior can also determine the chemical properties of the particle, since the nucleation site affects the electronic structure of the adsorbate and hence its chemical behavior.

Atoms evaporated into the gas-phase, reach the surface with a finite amount of thermal energy, which allows transient diffusion. Furthermore all depositions in this work are done at room temperature, which provides additional energy for atom diffusion. The initial step for the development of particles on a surface is the formation of a seed. Such seed is not mobile anymore by definition and is therefore able to grow in size by an attachment of additional atoms. Since the agglomeration of particles starts to evolve from such nucleation centers, the actual particle density is strongly linked to the initial number of these seeds on the surface. Commonly the formation of seeds is distinguished into homogeneous and heterogeneous nucleation[11, 231, 9, 229]. In the case of homogeneous nucleation the seed is usually a dimer, although in some cases the first stable agglomerate can be larger. After deposition, the atoms diffuse statistically on the surface until they find other atoms to form a stable seed, which than acts as a nucleation center. In this case the particle density is given by the number of seeds formed on the surface, which itself depends on the diffusion behavior, the atom flux and the actual size of the nucleus. Homogeneous nucleation however doesn't consider defects, that is an essential parameter in the case of heterogeneous nucleation.

As described in section (4.1.2) the surface of the MgO film is characterized by a significant number of defects. Therefore heterogeneous nucleation is expected to be more likely in this case, while homogeneous nucleation exclusively takes place on large defect-free surfaces. The dominance of homo- versus heterogeneous nucleation is governed by the interplay between the mean length of diffusion and the defect density.

If the diffusion length is larger than the actual defect concentration on the surface, the particle density is governed by the number of defects, since these defects stabilize the diffusing atoms and act as a seed for the particle formation. The diffusion length is however depending on the temperature. That's why heterogeneous nucleation becomes enhanced at higher temperatures, when the diffusion length is increased. Contrary the lowering of the potential modulations on the surface, decrease the binding energies of defect sites. Consequently, defects with small binding energies can not be occupied at higher temperatures anymore. If however, the temperature is low, the diffusion length is reduced and the diffusing atoms will not reach the defect sites. In this case homogeneous nucleation becomes the dominating process.

After the formation of a nucleation center the growth can evolve in different ways. The actual growth mode is hereby mainly determined by the surface free energy of the respective materials[232, 233] and the interface energy to the support. In general, three different modes can be distinguished. First of all, the layer-by-layer growth, which results in a complete wetting of the surface, is referred to as Frank van der Merwe growth. Second, the growth of three dimensional particles is called Vollmer-Weber growth mode. Finally, in the Stranski-Krastanow mode, a wetting layer is grown initially, followed by the growth of three dimensional particles. This three different modes are schematically shown in figure (5.1).

It is possible to discriminate these different growth modes by taking into account the different surface free energies of the metal γ_m, the substrate γ_s and the particle-substrate interface γ_i. The difference of the surface free energy plus the interface energy hereby provides a measure of the interactions between metal and oxide. In general a strong interaction leads to a wetting of the surface, whereas a weak interaction results in the formation of three dimensional particles. This is described by the contact angle θ given by the Young equation:

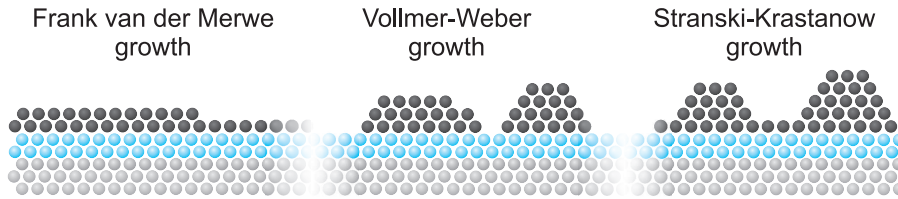$$\gamma_s = \gamma_i + \gamma_m \cdot \cos\theta \tag{5.1}$$

Figure 5.1: Schematic representation of the possible growth modes for a metal deposited onto an oxide film. Which mode actually evolves is strongly depended on the surface free energies of the metal, the substrate and the metal/substrate interface, as described by the Young-Dupré approach.

A small contact angle corresponds to a strong particle-substrate interaction and vice versa. The binding strength of the particle to the support is given by the energy of adhesion, the energy which is needed to separated the particle from the substrate. The adhesion energy E_{adh} is given by the Dupré equation which connects the various terms of surface and interface energies:

$$E_{adh} = \gamma_s + \gamma_m - \gamma_i \tag{5.2}$$

Both equations can be combined, giving the so called Young-Dupré equation:

$$E_{adh} = \gamma_m \left(1 + \cos\theta\right), \tag{5.3}$$

with θ the contact angle, as sketched in figure (5.2). Besides the Young-Dupré model, where the particle is seen as a metal droplet on the surface, the Wulff-Polyeder construction(figure (5.2.right)) allows predictions of the aspect ratio and furthermore the crystallographic orientation of the particle facets[234].
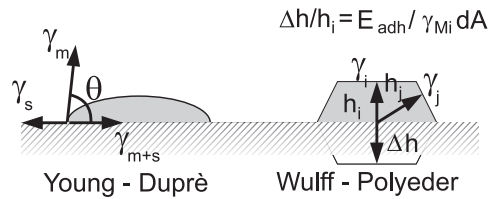

Figure 5.2: Schematic representation of the geometric considerations to determine the contact angle. The Young-Dupreé model(left) describes the particle by a metallic droplet, whereas the Wulff construction also allows to extract the crystallographic orientation of the particle facets(right).

In general the actual growth behavior can be extracted from the ratio between the surface free energies. If the sum of $(\gamma_m + \gamma_i)$ is smaller than the surface free energy γ_s of the substrate, the metal wets the surface and will grow in a flat fashion. If however this sum is larger than the surface free energy γ_s of the substrate the formation of 3D particles is observed[235, 236]. Such a behavior is expected for Mg($0.6 Jm^{-2}$) deposited on the MgO substrate, because of the larger surface free energy($1.19 Jm^{-2}$ [237, 9, 238])of MgO. Indeed this expectation was confirmed by the experimental results, as shown in the following.

5.1.1   Experimental Results

In this work a number of different metals were deposited onto the MgO film, such as Mg and Ca as earth-alkali metals, Ni as a transition metal and Ag and Au as noble metals. Crystallographic parameters of the respective metals are given in table (5.1).

As a general observation, all deposited metals nucleate and form three particles as expected by concerning the respective surface free energies. Nonetheless the value of the surface free energy alone is not adequate to describe the experimentally found growth behavior. In particular the shape and the crystallographic orientation of these particles is not captured by this approach. Additional parameters have to be considered for the description, as the difference in the lattice parameter, as well as the actual interaction between the oxygen sub-lattice of the MgO and the metal.

metal	crystal structure	lattice parameter [pm]
Mg	hcp	320,9
Ca	fcc	558,8
Ni	fcc	352,4
Au	fcc	407,8
Ag	fcc	408,5

Table 5.1: Crystal structure, lattice parameter and heat of oxidation are listed for the different metal studied in this work.

Mg Particles on MgO   The importance of these interactions is clearly resolvable for the growth of Mg particles on the MgO; the first simple metal investigated in this work. The strong interactions of simple metals with the oxide substrate is reflected in their high heat of oxidation, which is in the range of -500$kcal/mol$[239]. These interactions are associated with the formation of strong metal-oxide bonds[240, 241, 242, 243, 244]. Due to this affinity, the metal atoms preferentially occupy the MgO oxygen positions, resulting in a correlation between substrate lattice and particle on top. This interface contribution to the growth behavior is clearly found for most of the investigated metals.

Depositing Mg onto a 7 ML thick MgO film results in the formation of faceted and well oriented particles(figure (5.3)). However, a particle formation is not observed for the deposition of less than 1 ML. The Mg atoms of the first ML, which arrive at the surface are supposed to be incorporated into the film of defect sites. Such defects are for instance the dislocation lines discussed in section (4.1.3). The diffusing Mg is oxidized at these low-coordinated oxygen sites and does not form a metallic particle. This process is confirmed by X-ray photoelectron spectroscopy(XPS) measurements[245], that reveal a spontaneous oxidation of almost the complete first monolayer of Mg. Such an oxidation is much less pronounced for MgO films on an Ag substrate, where such deep dislocations are not present. Above the first mono-layer the XPS measurements confirm the metallic character of the particles.

Mg particles are found to preferentially nucleate at defects lines or low-coordinated sites on the surface. That these defects can act as strong binding sites is however expected from the observations made on the bare MgO film. The local increase of the work-function, induced by negative charges from trapped electrons and the different oxygen-rich stoichiometry are likely reasons for this enhanced preference. In addition, various binding sites are available, where Mg coordinates to two and more O-ions at the same time. Nucleation on the terraces or at point defects was however rarely observed. This observation is in line with earlier publications[246, 247], where also the terraces sites were found to play a minor role for the

nucleation.

Typical STM images of the Mg particles on MgO for different coverages are shown in figure (5.3). The particles develop distinct edges and well evolved facets indicating their crystalline character. Moreover, they are of rectangular or square shape and show a clear orientation along the crystallographic directions of the underlying MgO substrate. This correlation indicates the strong interactions between the metal and the oxygen underneath. The edges of the rectangular deposits hereby align with the orthogonal [110]-MgO directions, as depicted in figure (5.4). These are the directions of closed packed oxygen rows. Furthermore the Mg particles show atomically flat top facets, which frequently exhibit single steps or a roof like structure in some cases(figure (5.4.b,c). Besides the preferentially found rectangular shape, also slightly octagonal edges were observed, as well as distinct 45° angles.
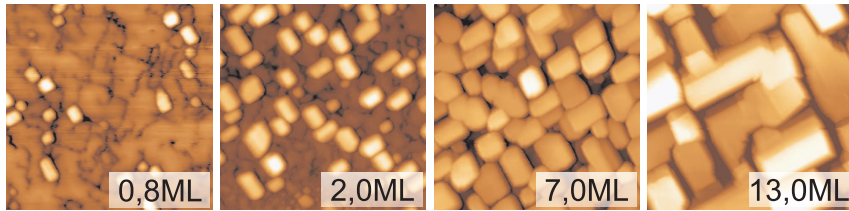

Figure 5.3: STM images($100 \times 100 nm^2$, $5.0V$, $0.05nA$) taken for a 7 ML thick MgO film covered by an increasing amount of Mg. Starting at a coverage of 1 ML rectangular particles are found on the surface, which grow preferentially in height for increasing dosage. At $\sim$8 ML the particles start to coalesce.

With increasing Mg coverage the particles grow in a pronounced three dimensional manner, where the aspect ratio(height/width ratio) increases to 1.0, being 0.5 at lower coverage. These 3D particles start to coalescence at $\sim$8ML, evolving to a compact film.

In order to assign the crystallographic orientation of the metal particles, the STM measurements were complemented by a photoelectron diffraction(PED) study, performed in collaboration with Dr. S. Benedetti from the group of Prof. S. Valeri at the University of Modena. These measurements were done using the Mg KKL Auger transition at $E_{kin} = 1187eV$, exploiting the large separation from the Mg^{2+} signal emerging at $1182eV$. The diffraction data were produced for Mg particles(10 ML nominal thickness) grown on a 10 ML thick MgO film, by moving the sample along an azimuth angle of $0° < \phi < 90°$ and a polar angles of $0° < \theta < 70°$ by a five-axis manipulator and collecting the emitted electrons with a hemispherical mirror analyzer. The polar angle θ hereby gives the tilting against the surface normal. Furthermore, the PED plots have been simulated with the MSCD program package, which is based on the Rehr-Albers approximation and includes single as well as multiple scattering events to determine the total diffraction cross-section[248].

The combination of both techniques allows to extract a growth model for the Mg particles. The PED stereogram in figure (5.5) suggests the (11$\bar{2}$0)-plane of hcp Mg to be at the
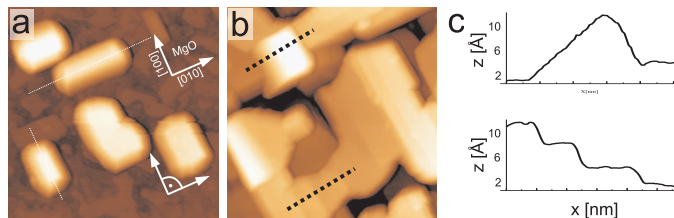

Figure 5.4: **(a)** Topographic image of typical Mg particles, characterized by the well oriented edges and the rectangular shape. **(b)** Image for coalescence of the Mg. Besides atomically flat top facets, also roof-like structures are found. The according height profiles are depicted in the line scan of **(c)**.
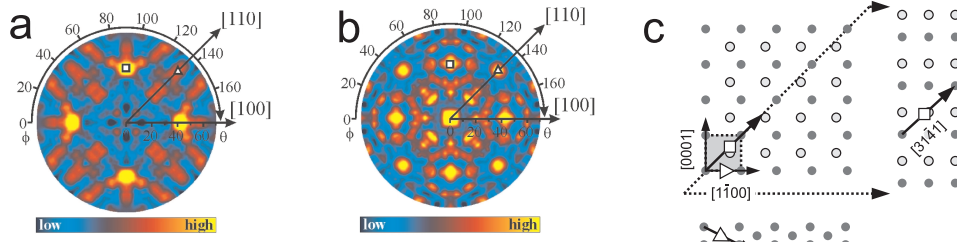
Figure 5.5: PED stereogram((**a**)) of Mg particles on a 10ML thick MgO film and the corresponding simulated PED stereogram obtained with the MSCD package. The most intense maxima are marked by a square and a triangular. These maxima correspond to the directions of scattering, as indicated in the schematic view of the hcp(11$\overline{2}$0)-plane in (c). (**c**) respective directions of the hcp Mg and the MgO.
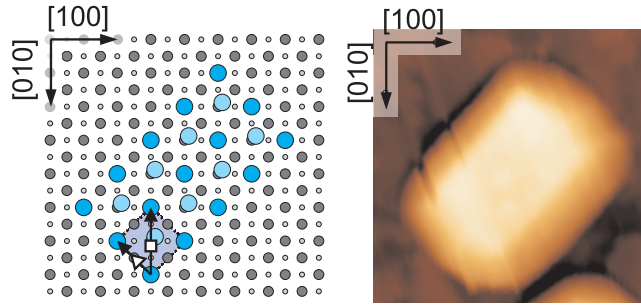

Figure 5.6: Schematic representation of the interface plane of the Mg growing onto the MgO substrate lattice. The unit cell is marked by the dashed lines. One of the two atoms in the unit cell has to be slightly displaced in order to occupy the oxygen site of the MgO(marked in light blue).

interface, because such an assignment enables the simulation of the experimentally found data with the best agreement. The four maxima along the equivalent MgO[110] directions at $\theta = 43°$, which originate from the forward-scattering of electrons along the Mg[31$\overline{4}$1] directions, are reproduced in the simulated stereogram at almost the same polar angle. Also the slightly weaker maxima at $\theta = 55°$ originating from scattering along the [0$\overline{1}\overline{1}$0]-direction, is clearly discernible in the simulation and further supports the assignment.

The interface plane of a Mg particle is shown in figure (5.6). The (11$\overline{2}$0) plane of the Mg hereby mimics the squared lattice of the MgO underneath and permits the occupation of the oxygen sites by the Mg atoms with a reasonable small distortion. Hereby the Mg [0001] direction aligns with the [110]-direction of the MgO. By realizing the Mg(11$\overline{2}$0) contact plane, every Mg atom at the interface is able to bind to a lattice oxygen, although one unit-cell atom needs to be displaced slightly from its original position. To reach commensurability with the oxide surface, the in-plane lattice parameter of Mg is stretched by 12% for the [0001]- and by 6% along [1$\overline{1}$00]-direction. This asymmetry in the lattice strain leads to a preferential growth along the direction of smaller mismatch and therefore results in the development of rectangular shaped particles. In general, the required elastic distortion of the interfacial Mg plane is rather large and can therefore only be realized in spatially confined nano-particles. As a consequence, the growth of Mg particles seems to be self-limited at a maximum width of 6–8 nm along the high-strain direction and continues mainly in vertical direction, if the coverage increases.

Mg, as the first example for particle growth on MgO clearly shows, that the surface free energy as considered in the Young-Dupré formula has to be extended by a contribution, that accounts for the preference of good lattice registry with the substrate and includes the associated distortion of the lattice.

Ca Particles on MgO   Though chemically very similar to the Mg, the main difference between Ca and Mg is the crystal structure. Ca has a fcc structure with a lattice parameter of $512pm$, which is 19% larger than the one of Mg. Since the interfacial binding between the metal atom and the oxygen of the oxide surface was found to be of crucial importance, it is likely that the larger lattice parameter will lead to structural differences.
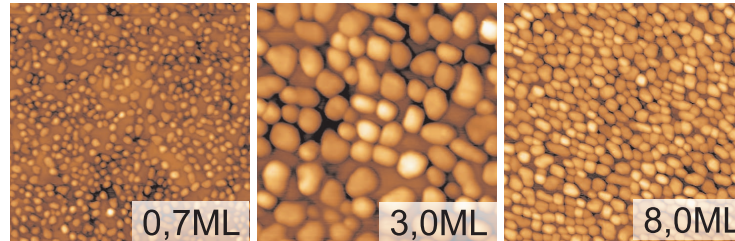

Figure 5.7: Topographic images($60 \times 60nm^2$(middle), $100 \times 100nm^2$, $5,0V$, $0,05nA$) of different coverages of Ca on a 7ML thick MgO film. Contrary to the Mg, the Ca starts to develop particles already below 1ML coverage. The rectangular shape, as well as the clear orientation with respect to the MgO lattice is evident at all coverages.

At the initial growth stage also the Ca is nucleating at defect sites in the MgO surface. Particles are preferentially found at the defect lines, as shown in figure (5.7). With increasing the metal exposure the Ca forms rectangular or squared particles, very similar to the Mg. Moreover the rectangular shape is evident in the STM images, as well as the clear orientation of the particle edges. The edges are however 45° rotated to the orientation of the Mg particle edges. However, the particles generally have a smaller aspect ratio, evolving from ∼0.4 at low to ∼0.7 at higher coverages. Furthermore the particles develop from flat top facets at lower coverage to a more hemispherical shape at higher coverages. In general the Ca particles do not have as regular base planes as it was observed for the Mg particles. Apparently the interfacial registry to the MgO is less prefect and the Ca is able to adapt to its bulk lattice parameter more easily. The nucleation density of the Ca is $\sim 25 \cdot 10^{11} \text{cm}^{-2}$, which is larger by a factor of three compared to the Mg($\sim 7 \cdot 10^{11} \text{cm}^{-2}$).
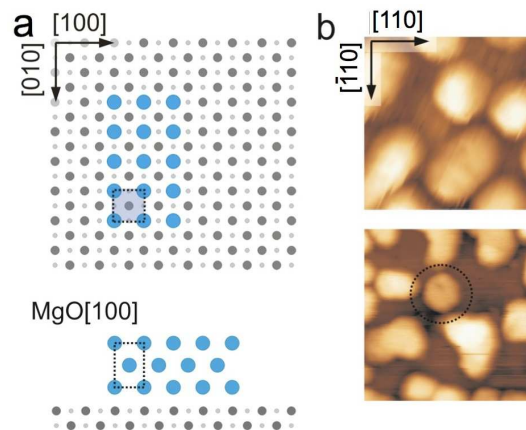

Figure 5.8: **(a)** Schematic representation of the growth behavior for Ca on MgO. The top view(top) show the squared arrangement of the Ca(001)-plane and the actual stacking is show in the side view cutted along the MgO(010)-plane. In **(b)** a typical Ca particle is show with the respective orientation(top) and one example of an hexagonal shaped particle(below), which was also observed in some rare cases.

The Ca particles on MgO were not investigated with PED and the growth model is therefore extracted only from the STM data. The most favorable configuration is assumed to be the one, where the number of Ca-O bonds is maximized and at the same time the lattice
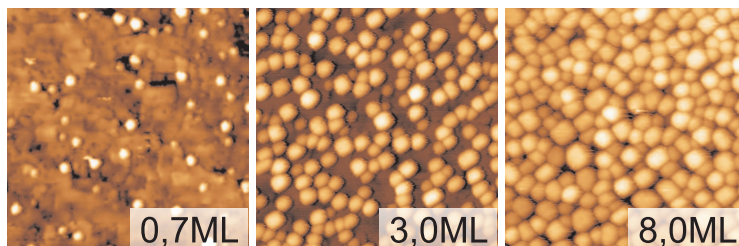
Figure 5.9: Topographic images($100\times100nm^2$, 5,0V, 0,05nA) of Ni on MgO for increasing coverages. Very similar to the simple metals, also the Ni preferentially nucleates at the dislocation line of the MgO. A particles develop a pronounced shape, which again is correlated to the MgO registry underneath.

distortion is reasonably small. Analyzing the different possible geometrical configurations, that fulfill both restrictions leads to the growth model presented in figure (5.8). The Ca interface plane with the MgO is the (001) plane, where the lattice mismatch amounts to 5.4%, when Ca occupies the oxygen in the MgO. Due to the larger lattice parameter of the Ca this matching of Ca and O is achieved best by orienting the Ca[110]- parallel to the MgO[100]-direction. It has to be pointed out, that in some cases also particles with a hexagonal symmetry are found in the experiment(figure (5.8)b). This (111)growth direction is stabilized by the lower free-energy of this surface. However, the ratio of Ca atoms sitting atop of lattice oxygen is strongly reduced in this case. On the other hand, the structural constrains in terms of lattice mismatch are softened for the (111) growth regime, which makes this mode particularly attractive at larger Ca exposures. The gradual transformation of the (100) in favor of the (111) growth direction at high exposure is reflected in the development of more hemispherical particle shapes. In this regime, the minimization of the total surface energy and not the interfacial registry governs the particle shape.

Ni on MgO The third material considered in this work is Ni, as a transition metal. It is chosen, because the parameters which lead to the strong correlation of the particle shape to the underlying MgO registry are different, compared to the simple metals. Ni has an almost three times smaller heat of oxidation(-57,3$kcal/mol$[239]) and should therefore show reduced interfacial interactions. With a fcc lattice constant of 249pm it is not suitable to adapt to the MgO lattice constant, since the mismatch amounts to -16%. Both factors suggest a growth mechanism, that differs from the one of the simple metals.

Figure (5.9) shows a series of STM images taken for different Ni coverages on the 7 ML thick MgO film. For low exposures of Ni the surface exhibits small spherical particles, that nucleate at the defect positions of the MgO surface. The fact that the formation of particles is observed already with the very first Ni deposition, indicate that the Ni is almost not incorporated into the defective MgO film. At increasing Ni dosage the formation of mostly squared particles is observed, although some particles tend to develop also rectangular shapes. Crystalline particles evolve with a clear edge orientation along the MgO[110]- and [1$\bar{1}$0]-direction. Also apparent from the topographic images is the correlation to the lines defects in the underlaying MgO, reflected by the tendency of the particles to align in chain-like structures, that follow the MgO dislocation lines. A higher dosage of Ni leads to an increase of the aspect ratio from 0.25 to 0.5 and to the formation of pronounced 3D particles. At a coverage of 6 ML also the Ni particles start to coalesce. As for the Mg, also for Ni photoelectron diffraction measurements have been performed. Stereograms were recorded using the Ni 2p core level at $E_{kin} = 633eV$ and changing azimuth and polar angle. The respective results are shown in figure (5.10).

The Ni stereogram does not show such a clear symmetry and peak structure as it was the case for Mg. This indicates a larger spread of the particle orientations and shapes. Nevertheless
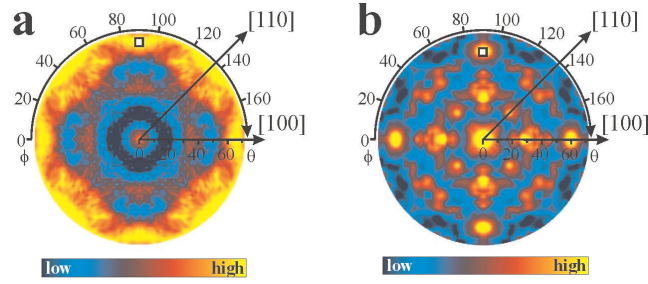
Figure 5.10: **(a)** Experimental PED stereogram of Ni on 10ML MgO, obtained at an energy of $E_{kin} = 633eV$. **(b)** simulated PED stereogram for the hcp Ni(11$\bar{2}$0)-plane. Although the overall agreement is less good than for the Mg, the most prominent features are reproduced. The diffuse, featureless experimental data is attributed to a rotational disorder of the Ni deposits.
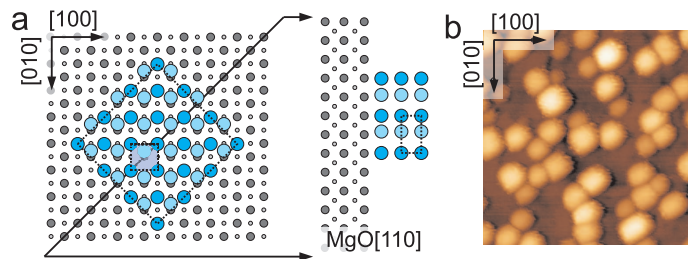

Figure 5.11: **(a)** Structure model of Ni particles growing on MgO(001), with top view and side view(below) cutted along the MgO[110]-direction. In **(b)** a typical topographic image of Ni particles is shown, indicating again the correlation between the MgO lattice and the actual particle shape.

some geometric parameters can be deduced from the PED measurements. Experimental PED maxima occur along the equivalent MgO[100] directions at $\theta = 62°$, indicating a square symmetry of the interfacial plane. In addition four maxima can be identified at $\theta = 35°$. However, along the MgO[110]-direction no clear features are recognizable. A first attempt to simulate the PED stereogram with a fcc Ni deposit growing along the [100]-direction did not reveal good agreement with the experiment. This was however expected, as the large mismatch with the MgO would lead to an unreasonable strong expansion of the interface layer. The energy costs associated with a 16% expansion are not likely to be compensated by the energy gain of the metal-oxide bond formation.

Relatively good commensurability with the MgO(001) is however reached, if the (11$\bar{2}$0)-plane of hcp Ni is assumed to form the interface layer and the hcp[0001]-direction aligns with the [100] of the MgO. In this configuration every Ni atom is able to bind to an oxygen in the MgO surface, whereby the Ni lattice undergoes a distortion of +4% and -2% along the hcp Ni[0001]- and Ni[11$\bar{2}$0]-directions. Using the PED maxima at $\theta = 62°$ along the Mg[100], the out of plane lattice parameter of hcp Ni is extracted to be 1.1Å. This value is close to the interlayer spacing of 1.24Å of the ideal hexagonal structure. The assignment of the interface plane is further supported by the PED simulations for a Ni(11$\bar{2}$0) orientation, as shown in figure (5.10). The main features found in the experiment are reproduced in this simulated stereogram. Due to the PED results and the fact that the formation of fcc Ni is unlikely, the interface plane is concluded to be the hcp(11$\bar{2}$0). Such a configuration represents the best balance between commensurability with the oxygen sub-lattice and distorting the Ni lattice. Nonetheless the hexagonal structure is not the preferred bulk phase of Ni. However, recent experimental and DFT studies reported also the growth of Ni nanodots in a hcp fashion, as this geometry strongly reduces the interface mismatch to the MgO surface[249, 250].

Since also for Ni a strong interfacial contribution to the particle formation was found, noble metal were investigated, with even smaller interfacial interactions.

Ag Particles on MgO   The noble metals Ag and Au were deposited as the third group onto the MgO. Both metals have a much lower heat of oxidation (Ag -$28kJ/mol$, Au -$50kJ/mol$[239]) compared to the simple metals Mg and Ca and even compared to Ni. Thus, they are suggested to show almost no interaction with the substrate. Therefore the actual growth behavior should be mostly governed by the bulk metal properties, in clear difference to the particles studied before. This expectation is further supported by the relatively small lattice mismatch, which amounts to ∼3% in both cases and therefore does not give strong restrictions for the growth behavior. However, the expectations hold in the case of the Au, but could be not confirmed for Ag.
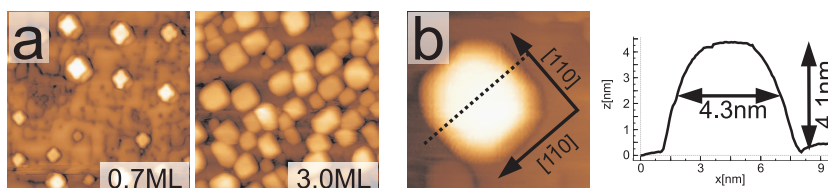

Figure 5.12: STM topographic images of Ag on the 7ML thick MgO film for 0,7ML and 3ML coverage. The image at the left side indicates the almost perfect cube shape of the particles, after the annealing treatment($800K$).

Depositing Ag onto the MgO surface leads to the formation of small metal particles, whereas once again the defect sites serve as nucleation centers for the metal atoms. In contrast to the expectation, the MgO registry is clearly reflected in the Ag particle shape. The Ag particles develop almost perfect square and rectangular shapes, with edges aligned to the [110]- and [1$\bar{1}$0]-direction of the MgO. The aspect ratio of the particles is rapidly increasing from 0.5 to one upon increasing the nominal thickness. Therefore most of the pronounced 3D particles have therefore an almost perfectly cubic shape. This trend can be furthermore enhanced, if the sample is annealed to $800K$. After the annealing treatment preferentially cubic particles are found on the surface, whereas the actual particle density has decreased by a factor of 10 from $8\cdot10^{11}$cm^{-2} to $5\cdot10^{10}$cm^{-2}. Such a de-wetting of Ag is in agreement with a small interfacial energy calculated by DFT[251]. The construction of a growth model in this case follows the considerations already discussed before and is furthermore strengthened by a number of theoretical works[180, 251, 252].
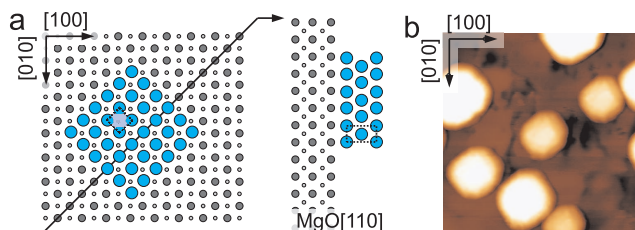
Figure 5.13: **(a)** Schematic representation interface plane of Ag particle on MgO. The top view(top) shows the squared arrangement, which is associated with a rather small lattice mismatch of 3% in the case of Ag. The side view(below) shows the actual stacking of the Ag lattice(cut along the polar [110]-direction). In **(b)** a typical Ag particle is show with the respective orientation to the MgO.

The experimentally observed orientation of the Ag particles can be reproduced, when the Ag(001)-plane forms the basis of the particle and the Ag[100] direction aligns parallel to the [110] direction of the MgO. A schematic view of this configuration is shown in figure

Figure 5.14: STM images($100\times100nm^2$, $5.0V$, $0.05nA$) taken for a 7 ML thick MgO film covered by an increasing amount of Au. Au forms hexagonal particles already in the initial stage of the growth. With increasing the thickness the particles stay flat. This 2D like growth leads to the coalesence already at $\sim$3 ML.

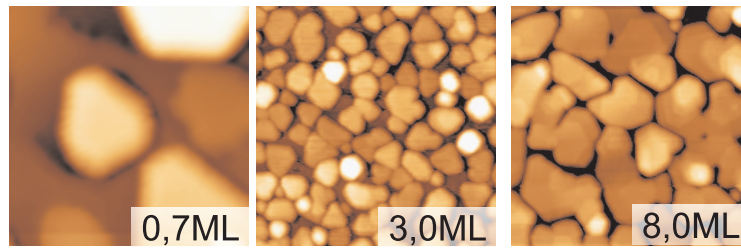(5.13). Since the lattice mismatch between the Ag and the MgO is only 3% the Ag lattice can adapt to the oxygen registry of the underlaying substrate relativly easy. Although the Ag atoms only have a small affinity to the oxygen, it still affects the particle formation and determines the well-defined particle shapes. It should be noted that the Wulff construction would predict a (111)-terminated truncated pyramid in this case.

Au Particles on MgO   The chemically similar Au is found to be the only case in this study, where interfacial interactions seem to play only a minor role. Starting already at low coverages the Au forms hexagonal or triangular shaped particles. Also here the defect structure of the MgO film is governing the nucleation of the particles, as it was already observed for all other metals. In contrast to the metal/MgO systems investigated before, no indication for the four-fold symmetry of the substrate is found. On the contrary, the Au particles develop distinct three-fold symmetries with increasing thickness. The interfacial interactions seem to be weak, so that the Au is not forced to adapt to the MgO registry, but is able to grow in a bulk-like fashion right from the beginning. However, a careful analysis of the topographic data still reveals a correlation between particle orientation and the underlaying substrate symmetry. As shown in figure (5.15) one of the particle edges is always aligned to the MgO[110] directions.
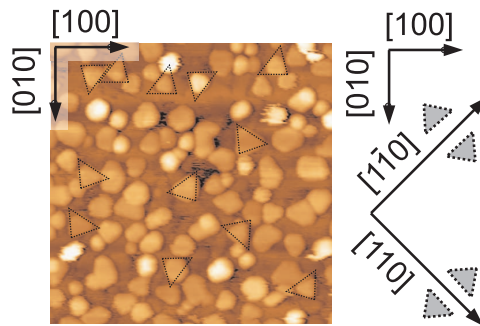
Figure 5.15: Topographic image of 2ML Au on 7ML MgO. The orientation of some triangular particles is indicated by dashed triangles. By comparison with the respective crystallographic directions of the MgO, it turns out that one of the edges is always aligned with one MgO[110] direction. Besides of this, the Au does not adapt to the MgO registry and grows in its bulk-like (111) orientation.

Furthermore the STM images of figure (5.14) show the almost perfect 2D character of the Au particles. Indeed, the Au was found to have the lowest aspect ratio among all investigated metal particles. The aspect ratio increases from 0.2 at sub-monolayer coverage to a maximum value of 0.4, which is already reached at a coverage of around 1 ML. Due to the flatness of

Figure 5.16: Growth model of Au on MgO. The energetically most favorable (111)-plane does only adapt to the underlying oxygen in one of the polar directions with 3% lattice mismatch. For the ongoing growth the Au is not fixed to the MgO registry. However, due to the relativly small mismatch every second atom sits on an oxygen position.

the particles, already at 2,5 ML coalescence sets in and the Au forms a compact film(figure (5.14)). The top facet of the particles are atomically flat with atomic steps visible in some cases.

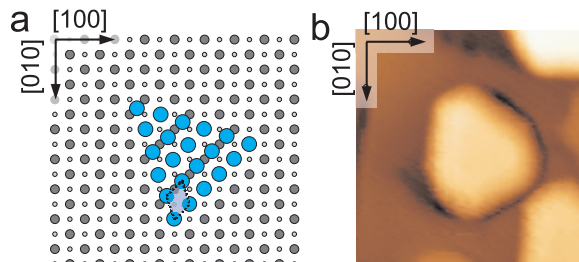The interface model presented in figure (5.16) is composed by overlaying the MgO lattice with the Au(111)-plane. The tendency of Au to occupy oxygen sites in the MgO still leads to distinct orientations of the hexagonal Au particles. Nevertheless, the interaction in not sufficient to fix the Au lattice to be in registry with the MgO(001). The particles therefore develop the energetic most favorable (111)-plane. The fact, that the Au is not in registry with the MgO(001) is particularly surprising as the lattice mismatch amounts to 3% only. However, only in the case of the Au such a weak correlation to the oxygen lattice of the MgO was observed, raising the question on the compatibility with the growth models sketched above.

5.1.2 Discussion

The investigation of a number of different metals deposited onto the MgO film allows us to draw some general conclusions on the growth of such particles. Several experimental findings suggest that the interfacial interaction are of crucial importance for the particle shape and orientation. This coupling to the MgO lattice is reflected by the two-fold symmetry of all particles, with the exception of Au, reflecting the squared symmetry of the MgO substrate. Also the variety of different interface planes in the particles suggests the significance of these interactions. This behavior can be traced back to the preferential formation of metal-oxygen bonds, with binding energies ranging from $0.4eV$ and $0.8eV$ for Ag and Au[253, 254], respectively, to approximately $1.0eV$ for many simple metals, and more than $2.0eV$ for various transition metals (Pd, Ni, Pt)[253, 254, 244]. The binding energies to the cationic species are on the other hand more than two times smaller and do not influence the actual growth. However, the strength of metal-oxygen bonds is not the only contribution, which governs the particle growth[255, 234, 233, 232].

In order to understand the growth, it is therefore necessary to modify the usual Young Dupré approach, as it was sketched at the beginning. In this approach the adhesion energy E_{adh} determines the particle shape of a particular system consisting of metal(γ_m), substrate(γ_s) and interface(γ_i). Although γ_i is a measure of the interfacial interaction it does not include the contributions given by the distortion of the interface layer to achieve a pseudomorphic growth with the substrate. Such a distortion is however important in the first layer and will only cancel out with additional layers, as the particle gradually adopts to the lattice constant of the bulk. Also the insertion of dislocations in larger particles is a conceivable way to release misfit strain. In order to introduce these effects into the Young Dupré approach,

the energy related to the lattice distortion has to be taken into account. The total adhesion energy is then given by:

$$E_{tot} = E_{adh} + E_{elast} \propto (\gamma_m + \gamma_s - \gamma_i) + (E\Delta^2) \tag{5.4}$$

Hereby lattice mismatch Δ and the Young's modulus E, are taken as a measure of the metal elasticity. This additional term $E_{elast} \propto E\Delta^2$ can only lower the total adhesion energy, since only positive values are possible. Therefore large E_{elast} is linked to more 3D particle shapes(more positive E_{tot}), whereas the particles are flat in the case of small E_{elast}(more negative E_{tot}).

Following this approach the experimentally found particle shapes can be rationalized. Hereby the respective value for the surface free energies are taken from the literature[256]. The surface free energy of the MgO is neglected, since it is equal for all experiments and therefore does not have to be taken into account for a simple comparisons. The interfacial energy γ_i is estimated by extrapolating the DFT binding strength of a single metal atom on MgO(001), by the number of atoms at the contact plane of the respective metal particle. This value can however only serve as an upper bound, since the single-atom binding energy is expected to decrease in an atom assembly due to depolarization effects at the interface. The surface free energies of the considered metals are averages over their most stable crystallographic facets[256]. This simplification is justified, as the energy differences between typical facets of one metal are usually much smaller than the spread between different metals.

Metal	Adatom adsorption energy $[kJ/mol]$ (M-O bonds in MgO unitcell)	Surface free energy $[J/m^2]$	Interface adhesion per UP $[J]$	Young's modulus [GPa][239]	lattice mismatch [%]	elastic energy per UP $[J]$	total adhesion per UP $[J]$
hcp Mg [0001] [1100]	49.2[257](1)	0.6	$1.8 \cdot 10^{-17}$	45	-12% -6%	$4.9 \cdot 10^{-17}$ $1.8 \cdot 10^{-17}$	$6.7 \cdot 10^{-17}$ $3.6 \cdot 10^{-17}$
fcc-Ca	82.0[207](1)	0.4	$-4.2 \cdot 10^{-17}$	20	-5.8%	$8.2 \cdot 10^{-17}$	$-3.4 \cdot 10^{-17}$
fcc Ni hcp-Ni [0001] [1100]	170.7[244](2) 170.7[244](2)	2.7 2.7	$-5.2 \cdot 10^{-17}$ $-5.2 \cdot 10^{-17}$	214 214	-16% +4% -2%	$5.5 \cdot 10^{-16}$ $3.4 \cdot 10^{-16}$ $8.6 \cdot 10^{-17}$	$4.0 \cdot 10^{-16}$ $-1.7 \cdot 10^{-16}$ $-4.3 \cdot 10^{-17}$
fcc-Ag	40.5[244](2)	1.2	$4.4 \cdot 10^{-17}$	72.5	-2.6%	$7.9 \cdot 10^{-17}$	$5.2 \cdot 10^{-17}$
fcc-Au	85.8[244](1.5)	1.6	$3.9 \cdot 10^{-17}$	74.5	-2.6%	$8.1 \cdot 10^{-17}$	$4.7 \cdot 10^{-17}$

Table 5.2: Summary of the parameters that are included in the estimation of the total adhesion energy for the different metal particles and different phases.(unit particle (UP))
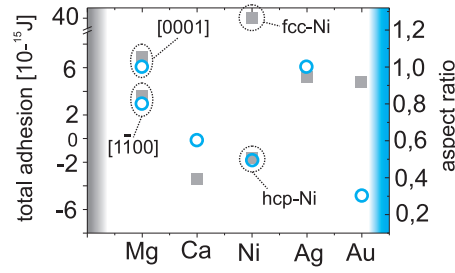
Figure 5.17: The total adhesion energy(gray squares) as well as the aspect ratio(blue circles) for the respective metals are plotted. With the exception of Au the estimation of the interfacial interactions by the modified Young-Dupré approach correspond to the particle shape(aspect ratio) extracted form the STM measurements. This shows the suitability of the model to explain the observed particle shapes. In the case of Ni it is furthermore emphasized that a fcc growth is energetically not possible.

The calculated values of E_{tot} for the different metals are shown together with the respective aspect ratios in figure (5.17). Although the matching is not perfect, it clearly shows the correlation between these parameters and therefore the possibility to rationalize the actual particle shape by the modified adhesion energy.

In the case of the Mg and Ag rather tall particles form, in correspondence to the more positive value of E_{tot}. The reason, in this case of Mg is the large lattice distortion, which leads a large value of E_{elast}, whereas in the case of Ag it is the high surface free energy($1.2 Jm^{-2}$). The Ca however forms more flat particles with a smaller aspect ratio, which results from a stronger Ca-MgO adsorption strength and the low elastic constant.

Even for the Ni case, the model provides an explanation for the development of hcp particles with a $(11\bar{2}0)$ contact plane. To illustrate this, the respective values are given for the possible fcc planes, as well as for the hcp. It is clearly recognizable, that the large misfit with the fcc-lattice of 16% results in a total adhesion energy, that is one order of magnitude larger than the usually found values. This excludes the formation of the fcc orientation by simple energetic arguments. Furthermore, the large value of the Young modulus has to be recognized, which also leads to a larger value of E_{elast}. If however the hcp$(11\bar{2}0)$-plane is considered, the substantial reduction of the lattice mismatch counteracts the large elastic constant and leads to a reasonable value of the total adhesion energy. The development of a hcp-plane is therefore preferred at the interface, although the resulting lattice structure is not the energetically most favorable bulk phase of Ni.

It has to be pointed out, that this approach provides a relatively good estimation for the particle shape, but it fails in the case of the Au. This is however not too surprising, since the growth of Au particles on MgO is known to involve charging effects due to electron-tunneling from the metal substrate into the Au, as it was discussed already in a number of experimental and theoretical works[179, 191, 192]. Such charging or polarization of the particles strongly affects the growth behavior of these particles, because additional electrostatic or polaronic interactions occur. These effects are not captured by the sketched approach. The prediction of 3D particle growth for Au, due to the small metal-oxygen binding energies and the large surface free energy, does therefore not match the experimental data in this case.

However, with the exception of Au, the insertion of an additional term E_{elast} allows to rationalize the experimentally found growth behavior on MgO.

Finally, the metal nucleation behavior shall be discussed. For all metal particles the defect
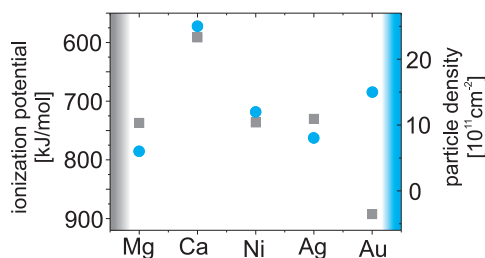
Figure 5.18: The ionization potential(grey squares) and the particle density(blue circles) are plotted for the different particle materials. The comparison indicates the same trend, reflecting the relation between the ability to become cationic at the dislocations and the actual particle density. Again the Au is an exception, since charging through the MgO changes the nucleation behavior.

sites in the MgO surface were found to serve as nucleation centers. However, looking to the actual particle densities listed in table (5.3) shows, rather large deviations, although the number of defects in the surface should only slightly differ form one experiment to another. Regarding the generally high defect density in the MgO films, leads to the conclusion that homogeneous nucleation does not play a major role. The actual density seems to depend on the critical seed and the respective affinity of the metal to attach to a MgO defect.

Metal	Ionization potential $[kJ/mol]$[239]	Particle density $[cm^{-2}]$
Mg	737.05	$6 \cdot 10^{11}$
Ca	591.37	$25 \cdot 10^{11}$
Ni	736.08	$12 \cdot 10^{11}$
Ag	730.29	$8 \cdot 10^{11}$
Au	892.37	$15 \cdot 10^{11}$

Table 5.3: Values of the ionization potential and the measured particle densities for the respective metals.

As already discussed, the MgO line defects are considered as electron traps, which are able to attract electrons from an electro-positive material and capture them by their Madelung potential[258, 259, 196]. This is also indicated by the potential of the MgO film to oxidize almost 1 ML of Mg and the strong influence of the defects on the work-function as observed by STS and PSTM measurements. This interpretation may suggest, that the ionization potential of the respective metal provides a good measure of their actual affinity to attach to the defects. A low ionization potential means, that the metal becomes cationic in vincity of the line defects more easily, compared to a material with a high ionization potential.

If the ionization potentials are compared for the different particle materials, it turns out, that the particle densities follow reasonably well the ionization potentials. Correspondingly, Ca that is the material with the lowest ionization potential exhibits the highest nucleation density among all metals. For Mg, Ni and Ag the respective values of the ionization potential are very close to each other and also the particle densities are rather similar. Only, for Au the suggested sequence of Ca>Ag>Ni>Mg>Au for the particle density is clearly broken.

Although the Au ionization potential is particularly high, the particle density on the MgO surface is comparatively large. An explanation for this discrepancy has already been given in the discussion of the particle shapes. The Au has the unique property to become anionic

on the MgO thin film, as the Au $6s$ affinity level shifts below the MgO/Mo Fermi energy and becomes doubly occupied. In analogy to the cationic Ca, the anionic Au experiences strong Coulomb interactions with the oxide Madelung potential, promoting the formation of seeds for particle growth. The fact that also Au preferentially nucleates along the MgO misfit dislocations indicates a certain electron-donor character of the defect lines. Electron transfer out of this state might be easier than out of the Mo support, rendering charging and nucleation of Au on the line defects more probable, in agreement with the experimental results.

5.2 Optical Properties of Metal Particles on MgO Films

As in the case of the bare MgO film, also for the metal particles, two bias regimes were investigated for the light emission. The investigations were done in a spectroscopic manner, probing the wavelength resolved emission from different particles and by recording photon-maps, in order to get insight into the spatial localization of optical modes in the particles. Most of the work was done on Mg, Ca, Au and Ag particles, while Ni was only investigated from a topographic viewpoint and is excluded from this discussion. Furthermore photon-maps are exclusively presented for Mg, Ca and Ag particles, due to the high quality of these data.

5.2.1 Field Emission Regime

Comparing the optical response of the bare MgO film with that of the particle-covered films in the field emission regime shows only slight changes for Mg and Ca, but more rigid shifts for Au particles.

Figure (5.19) shows the emission spectra of bare MgO in comparison with the same film covered with Mg, Ca, Au, Li and Ni respectively. The spectra are normalized to the maximum intensity in order to be able to compare the respective energy positions of the emission bands. It has to be noted, that the observed emission intensity is not suited for a precise quantitative analysis, because of a significant influence of the tip shape on the intensity. Nevertheless a qualitative comparison is possible. In general the emission intensity is reduced, if the metal is deposited onto the MgO. In the case of Li and Ni, the pronounced reduction of the emission intensity indicates the efficient quenching of the intrinsic MgO emission mechanism. Such a reduction might be linked to a blocking of the optical active sites on the MgO surface. Since the optical properties of the MgO film are governed by the deactivation of excitons at low-coordinated sites in the surface, it is not surprising that the deposition of metal particles can influence the optical activity of those sites. As shown in section (5.1) the particle growth initially starts at exactly these low-coordinated sites. If such a site is occupied by a metal particle, it is not available for the radiative deactivation of excitons anymore. This effect is strongest in the case of Li particles, where the characteristic emission of the MgO is almost fully suppressed by the metal deposits. The behavior can be traced back to the distinct particle morphology. The Li does not agglomerate into large 3D particles, but disperses over the entire surface in rather flat islands. Therefore almost every optically active site is blocked by the Li and the MgO light emission is efficiently quenched.
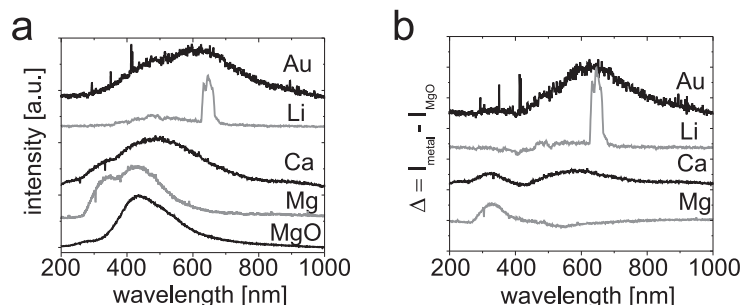

Figure 5.19: **(a)** Field emission spectra($200V$-$250V$, $(1\text{-}3)nA$, $1min$) of a 7 ML thick MgO film and the covered with the respective metal particles. The optical response is a convolution of the characteristic MgO emission and the emission associated with the Mie-plasmon in the metal particles. **(b)** Optical response of the particles, obtained by subtracting the MgO

In the other cases the emission is still dominated by the well known band of the bare MgO. This band is however red-shifted with respect to the uncovered surface in the case of Au, almost not shifted for Ca and slightly blue-shifted for Mg covered films. These shifts are attributed to the presence of metal particles and their associated optical modes. The observed emission characteristic thus consists of a contribution from the MgO and a second one, that is intrinsic to the metal particles. As discussed in section (5.20) the optical response of a metallic particle can be described by the Mie-theory, where a metal sphere is resonantly excited at the plasmon energy. This plasmon resonance can be calculated, if the dielectric function of the material is known.

The calculations of the Mie resonances are done using the Granfilm program by R. Lazzari and I. Simonsen[37]. Dielectric functions were taken from the Sopra database[260], as well as from the literature. All spectra were calculated using a typical particle diameter and the same substrate(MgO). The experimentally obtained spectra however represent the optical response of a large number of different particles, since the excitation in the field emission regime involves a rather large surface area. This leads to a broadening of the measured peaks compared to the calculated ones. The calculated Mie resonances for the different materials deposited on the MgO is shown in figure (5.20).
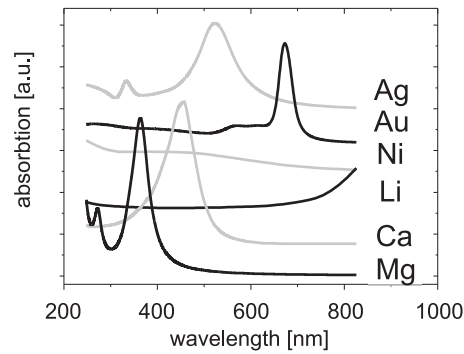

Figure 5.20: Absorption versus wavelength as calculated with the Granfilm software package. The peaks represent the Mie-resonance of the respective particle, described by its dielectric function and typical diameters as extracted from experiment. The particle is hereby modeled as a spheroid on the MgO support.

Comparing the experimental findings with the Mie-resonances from the calculation clearly shows the relation between the respective shifts in the experiment and the calculated position of the plasmon. Whereas in the case of Mg and Ca, the energy difference between the MgO mediated emission at $400nm$ and the emission associated with the plasmon excitation is small, it is more pronounced for the Au. Both contribution are separated in energy in this case, giving rise to almost two different bands in the in the FER spectra.
However, the effect of Mie plasmon excitations is not very pronounced. This can be explained, because only Ag and Au are good Mie scatterers as their electronic structure is free-electron like. Ni on the other hand has d-electrons directly at E_F which strongly quench the plasmon excitations. For Li, Mg and Ca the perfect scaling of the Mie resonances with the electron density can be seen, which is however blurred in the experiment due to modifications in the particle shape. Additionally the particles undergo some damages at the high electron energies. Such damage was frequently observed in STM images of the probed area taken before and after the electron bombardment. After bombardment, the particles were sometimes found to be desorbed from the surface or agglomerated into larger units. Furthermore the effect of field enhancement is only weakly evolved at this sample voltages, as the tip-sample separation is large and the corresponding interactions are small.

The tip-sample interactions become more important, if the actual tip-sample separation is reduced significantly. This is the case in the tunneling regime, when the bias is reduced to $3V$ – $10V$ and the field enhancement increases due to coupled plasmon modes in the tip-sample cavity. Because of that, investigations of the optical properties are possible at this lower bias even for single metal particles. Such experiments are discussed below.

5.2.2 Tunneling Regime

Decreasing the sample bias leads to a smaller tip-sample separation and simultaneously to an enhanced interaction between both electrodes. The associated electro-magnetic near field in the tip/sample cavity enhances optical modes at the surface, whereas the number of active center is reduced at the same time.

Indeed the observed light emission is found to exhibit pronounced differences compared to the field emission regime. Furthermore, working under tunneling conditions allows to probe the optical properties of single metal particles, instead of averaging over an ensemble of different particles.

To probe the optical response of a single metal particle the tip is stopped right above the respective particle and the beam of tunneling electrons is used as a local source of excitation. Leaving the feedback on, the current is increased slowly to usually 1 to $4nA$. This is necessary to get a sufficient photon yield and to achieve reasonable acquisition times. For acquisition times of $1 - 5$ min the photon emission is recorded with the liquid nitrogen cooled CCD device coupled to a spectrograph. After the spectral acquisition the current is reduced again to the usual tunneling conditions and a STM topographic image is taken, to exclude possible damages induced by the enhanced electron flux. For bias voltages below $\sim 8V$ no damage was observed in most spectral runs. It was even possible to reproduce the spectra for single particles several times($>$20 spectra à $2min$) without any observable changes of the particle. At higher bias voltages, desorption or modification of the particle were observed in some cases, although even at these conditions reproducible spectra could be acquired.

Optical Properties of Single Mg Particles on MgO Figure (5.21.left) shows a STM topographic image of Mg particles deposited onto a 7 ML thick MgO film. The right side shows the associated emission spectra, which were recorded at a bias of $7.0V$ on the enumerated particles. The topographic image shows a number of Mg particles, which differ in size and shape. For example particle② is rather high and almost round, whereas particle ⑥ has only 50% of the height and is elongated in one direction.

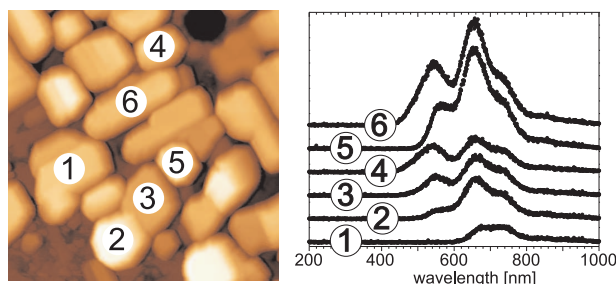Figure 5.21: STM topographic image(left, $100 \times 100 nm^2$, $5.2V$, $0.1nA$) of Mg particles on a 7 ML thick MgO film and the corresponding light emission spectra(right, numbered) taken at $7.5V$($2nA$, 3 min aquisation time). The spectra do not show a clear correlation to the particle size and consists of a pronounced peak structure.

Since the geometry of these particles is rather different, also their optical response should

differ. But the corresponding spectra of both particles reveal only slight differences, while the main characteristic is reproduced. Three emission bands are well resolved in the spectra. The wavelength of the bands is the same for both particles, and the main difference occurs for the intensity. Additionally the spectra of particle⑥ exhibits some intensity also below $500nm$, which is not found for particle②.

Generally the comparison of several spectra taken on differently sized particles did not lead to a clear relation between the actual size of the particle and the optical response. This is surprising, in particular because former investigation on similar systems did reproduce the expectations for Mie resonances as a function of particles size.

One example is the work of Nilius *et al.* [261], where Ag particles on an alumina support were investigated. Depending on the size of the actual particle, the single emission band, which is attributed to the radiative decay of the corresponding Mie plasmon, shifts in energy. This is explained by the size-dependent impact of depolarization fields of the d-electrons, that lowers the plasmon energy of the particle. The depolarization field becomes less relevant, if the size of the particle is decreased, because the $5s$-electrons that represent the free electron density of the particle, are much more delocalized, than the d-electrons. Thus the s-influence is strengthened at the surface of the particle and the plasmon energy increases for particles with large surface to volume ratios. Therefore the plasmon frequency blue-shifts in smaller Ag particles, as observed in the experiment.

However, the effect is not present for Mg, which has no d-electrons. But still, a size dependence would be expected also in this case. The plasmon resonance should show a red-shift, if the particle size decreases. The plasmon energy for these simple metals is proportional to the electron density as depicted in equation (2.1)(section(2.1)). This electron density is decreasing however, if the particle size becomes smaller, due to the spill out of the electrons at the surface. The actual ratio between the volume occupied by the electrons and the classical volume of the particle increases and explains the red-shift of the plasmon energy for simple metals with decreasing size[261].

The fact that such a size-dependence is not found for the Mg particles on MgO suggests, that the light emission behavior can not be described in the simple picture of the Mie-theory. Therefore the interpretation focused on the actual peak structure in the spectra, since this structure does not follow the expectations for plasmon excitations in metal spheres.

For all different particles the light emission is characterized by a number of emission bands in the spectra. The spectra taken at a particular bias show emission bands, which are at constant wavelength positions. The difference between different particles is mainly reflected in the number of emission bands, developed in the spectra and their intensity. To verify this observation the spectra of different particles and of different experimental runs were fitted with a fixed set of gaussian peaks.

This fitting is exemplarily shown in figure (5.22). It turns out, that it is indeed possible to describe the optical response of different particles by the use of such a set of energetically fixed emission peaks(table (5.4)).

The fact, that this set of emission bands is independent of the particle geometry, excludes the interpretation of this structure as different plasmon modes in the particles. For a perfectly spherical particle the plasmon energy is three-fold degenerated, corresponding to the three equivalent axes. If the geometry of the particle is changed to a spheroid, this degeneration is lifted and three different modes, which are now separated in energy can be observed. However, since the dipolar mode of a sphere is three-fold degenerated corresponding to the three axes of the particle, one would expect maximal three energetically separated emission bands in the spectra. This is not confirmed by the experimental results, where frequently up to five bands are observed. Secondly, the symmetry of the tunneling junction is such,
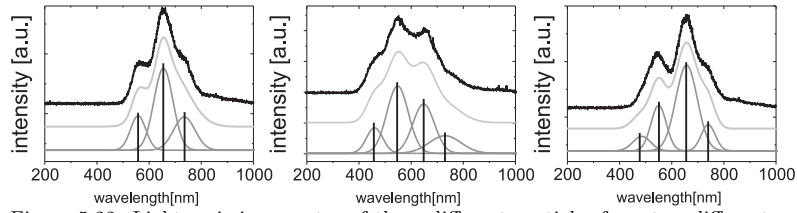
Figure 5.22: Light emission spectra of three different particles from two different experimental runs. The corresponding gaussian peaks, used to reproduce the optical response are shown below. Spectra for different particles, experimental runs and voltages can be reproduced by the same set of energetically fixed peaks(see table 5.4).

that only plasmon modes which are parallel to the electron flux can be efficiently excited. This is because the dipole induced by the tunneling electrons is perpendicular to the surface. Therefore one would expect to preferentially find the out of plane plasmon mode, that means only one emission band. This consideration might be one reason, why the optical response is very similar for very different particles. Since the out of plane mode would only depend on the actual particle height, only changes in the height would affect the plasmon energy. Nevertheless, the observed peak structure cannot be explained within such a picture.

peak position [nm]
$(730\pm10)nm$
$(650\pm15)nm$
$(550\pm15)nm$
$(475\pm15)nm$

Table 5.4: Center positions of the gaussian peaks used to fit the experimental spectra of the different particles. Changing the energy positions within the given range allows to reproduce every single particle spectrum from the experiment.

In order to get insight into the light emitting process, also the dependence of the optical response on the bias voltage was investigated. This is shown in figure (5.23) for one selected particle.

The spectra were acquired by positioning the tip over a single particle and gradually increasing the excitation bias. The overall emission characteristics can be reproduced again by fitting the spectra with a set of peaks, as shown in table (5.4). These fit values hold for every bias value.

Moreover it is found, that the every peak starts to appear at a specific bias value, which means, that higher energetic bands are only excited at higher bias. This observation is verified by plotting the respective peak intensities versus the bias, as it was extracted from the fitting procedure(figure (5.24)). The light emission appears first at a voltage of $\sim5.5V$ with a low energy emission at $730nm$. Increasing the bias leads to the gradual arising of more emission bands. The emission at $650nm$ appears at $\sim5.8V$, the emission at $550nm$ at $6.9V$ and finally the emission at $\sim470nm$ starts at $7.2V$, although this value can not be determined precisely, since this peak does not evolve into a pronounced maximum.

This behavior is interpreted such, that different emission channels are present in the Mg/MgO/Mo system, which open at different voltages. In addition it is found, that the appearance of further emission bands in the particle spectra stops at roughly $7.5V$. Further increase of the voltage does not change the composition of the spectra anymore, but leads to a reduction of the overall intensity. This behavior was independently measured by placing the tip over a
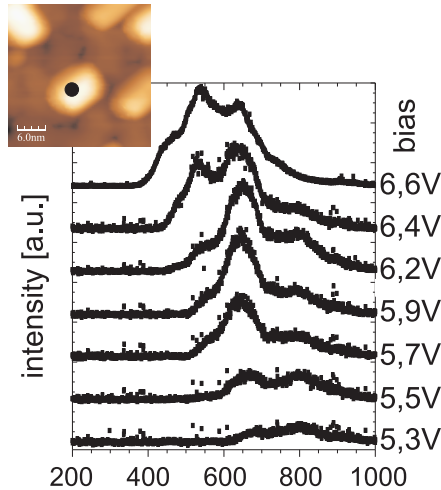
Figure 5.23: Single particle emission spectra for increasing excitation bias($1.0nA$, $1min$). With increasing bias, new emission bands start to appear in the spectra. At $7.0V$ no further emissions evolves and a further increase leads to a decrease of the emission intensity(not shown here).

single particle and ramping the voltage while recording the integrated photon intensity with the photomultiplier-tube(figure (5.25)).

Two additional conclusions can be extracted from the measurements discussed above. The most intense emission band is the one at $\sim 550nm(2.25eV)$. Moreover, the energetically highest emissions from the Mg particles is observed at roughly $400nm(3.1eV)$. Even at higher bias, no additional emissions bands are observed. This upper limit for the emission will therefore be called cut-off wavelength(energy) in the following.

Summarizing the investigation of the optical properties of Mg particles on MgO films, three main observations are crucial to note at this point. The spectral response of a particle can be decomposed into different peaks, whereas only the respective intensity changes between the different particles. Moreover it is possible to fit every single-particle spectrum by the use of these fixed peaks(table 5.4). This distinct emission bands evolve with increasing bias, while the most intense one is the band at $550nm$. Further bias increase does not lead to additional peaks, but results in a characteristic cut-off wavelength at $\sim 400nm$.

In order to examine, if the observed behavior is unique for the Mg/MgO/Mo system and furthermore, to investigate the influence of the respective particle material, other metal/MgO/Mo systems were now investigated.

Optical Properties of Single Ca and Au Particles on MgO: Tunneling Regime
Examples for the optical response of Ca and Au particles on a 7 ML thick MgO film are shown in figure (5.26). The actual light emission spectra correspond to single particles, which are indicated in the inset. By comparing these spectra with the ones for the Mg particles, some similarities become evident. Ca, as well as Au spectra are not characterised by one single emission band, but by a number of different bands. In order to evaluate the relation between particle size and optical response, also in this case the spectra were fitted with a number of gaussian peaks. Interestingly the fitting did show the same behavior as it was already found for the Mg. The spectra of Ca and Au particles could be fitted with a set of peaks, whereas the energy position of the respective peaks was almost constant and did not show a clear dependence on the particle size.
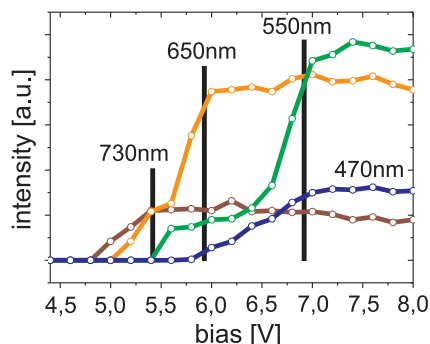
Figure 5.24: Intensity of the emission bands used to fit the single-particle emission spectra depending on the excitation bias. Increasing the bias, results in the appearance of the different bands, whereas the low energy(longer wavelength) bands appear before the higher energy(shorter wavelength) emissions.
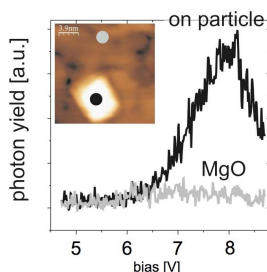

Figure 5.25: Energy integrated photon yield measured at the position of a Mg particle and on the bare MgO, depending on the applied bias. Whereas the intensity goes through a distinct maximum at $\sim 8V$ in the case of the Mg, almost no emission is observed for the MgO.

Although a relation between intrinsic properties, like the size or shape of the particles were not found, the actual shape of the spectra was found to depend on the excitation bias. This bias dependence is shown in figure (5.27).

Again, the emission characteristic shows certain similarities to the experimental results of the Mg/MgO/Mo system. The photon emission starts at around $5.5V$. A further increase of the voltage leads to the emergence of additional peaks in the spectra. In contrast to Mg, the most intense bands are found at $\sim 540nm$ for Ca and at $\sim 650nm$ for Au. If the bias is increased to more than $\sim 8V$, also the cut-off wavelength, as defined for the Mg particles, can be determined. The respective cut-off wavelengths are $\sim 410nm$ for Ca and $\sim 510nm$ for Au.

Summarizing the observations for both particle systems, one has to notice a number of similarities with the emission characteristics of the Mg system. These similarities lead to the assumption, that the emission mechanism for all three systems might be of the same nature. To verify this assumption, the spectra of the different metal particles have to be compared in more detail.

Since the light emission of a single particle seems to have almost no dependence on the particle geometry, the discrimination between different particles is not longer useful. Therefore the different single particle spectra were summed up, to get the overall optical characteristics for the specific metal/MgO/Mo system. For the bias, at which all peaks are fully evolved in
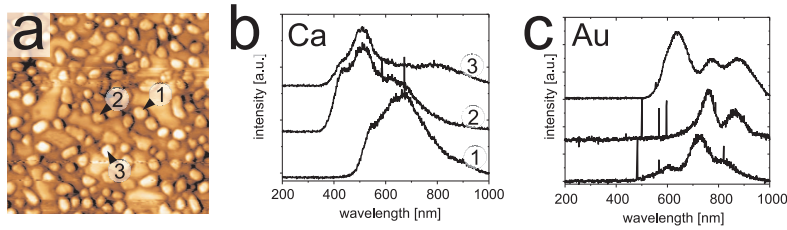
Figure 5.26: Light emission spectra($7.0V$, $1.5nA$, $1min$) taken on different Ca particles on a 7 ML thick MgO film. Similar to the optical response of Mg particles on MgO, also in this case no clear relation between particle geometry and optical response was found.
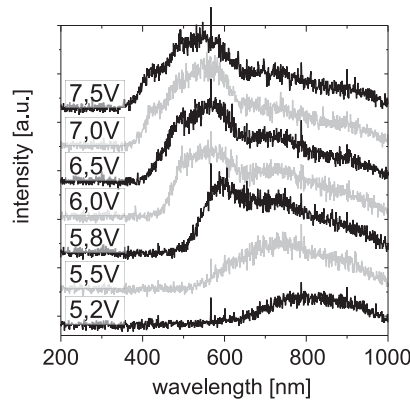

Figure 5.27: Optical response of a single Ca particle for increasing bias($1nA$, $1min$). If the voltage increases, new emission bands start to appear in the spectra. Above $6.5V$ all peaks are fully developed and no additional bands appears anymore.

the spectra, this represents the particle-size-independent optical response of Mg, Ca and Au particles on the MgO film. The respective average spectra are shown in figure (5.28). They represent the sum of 50 to 100 single-particle spectra, taken for different particles within different experimental runs.

The surprising observation from the averaged spectra of figure (5.28), is the appearance of a peak structure, which is present in the optical response of all three metal particles. This conclusion was already implied by the fitting of the respective single-particle spectra with the same set of gaussian peaks. It turns out, that this set, which describes most single spectra, is almost equal for the different systems. The energy positions of the observed peaks is only shifting by some ten meV, which might be explained by the effect of tip changes and the possibility of small differences in the MgO film thickness. The average spectra allow however to point out the differences between the respective systems more clearly. Besides the almost equal peak structure, those differences are the cut-off wavelength and the position of the most intense emission, as summarized in table (5.5).

To come up with a model for the light emission mechanism of such systems, the peak structure and the cut-off/maximum wavelengths were studied separately. Hereby the emission characteristic apparently consists of a contribution, which depends on the material of the particle and a contribution which is material-independent.

The cut-off wavelength and the respective emission maximum is considered to be material-dependent, since these values are very different for the different metals. The peak structure
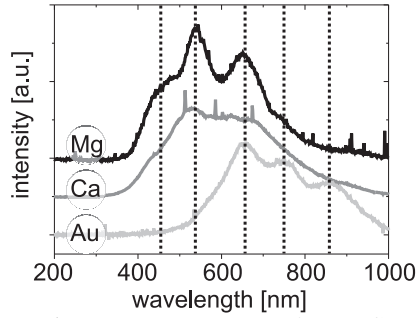
Figure 5.28: Averaged optical response for Mg, Ca and Au particles on MgO. The spectra are averaged over $50 - 100$ single particle spectra. A comparison shows the emergence of a peak structure with the same energy distribution and different cut-off wavelengths.

metal	cut-off	maximum
Mg	$390nm(3.2eV)$	$530nm(2.3eV)$
Ca	$400nm(3.1eV)$	$540nm(2.3eV)$
Au	$510nm(2.4eV)$	$650nm(1.9eV)$

Table 5.5: Summary of the cut-off wavelengths and the positions of maximal intensity for the different metal particles.

on the other hand is assigned as the material independent contribution, because the peaks are found at always the same energy position for all materials. To get a description of the light emission mechanism, one has to identify the origin of these two contributions. In the case of the material dependent part is seems to be reasonable to assign it to the dielectric properties of the particle. The material independent part however seem to be an intrinsic property of the whole metal-oxide system.

In the following the material dependent contribution is discussed first.

As a starting point, the different metal particles are treated in the frame-work of Mie-theory. As pointed out already this is reasonable, because all metals considered here, have a s-dominated state density at the Fermi level and therefore fulfill one criteria for the existence of Mie plasmon excitations. Furthermore such excitations can efficiently couple to light and show high oscillator strengths, which would explain the relatively high photon intensities observed in the experiment. Referring to the discussion in section (2.1), the optical response of a spheroidal metal particle is given by the frequency(ω) dependent polarizability:

$$\alpha(\omega) \propto \frac{\epsilon(\omega) - \epsilon_m}{3\epsilon_m + 3L_\perp(\epsilon(\omega) - \epsilon_m)}. \tag{5.5}$$

Hereby the depolarization factor $L_\perp$ is given by the aspect ratio, as extracted from the STM data. For this calculation only the (1,0)-mode is considered, since this is the mode which can be efficiently excited in the tunnel junction. The results of this calculation is shown in figure (5.29).

The vertical plasmon peaks are found at $\sim 420nm(2.95eV)$ for Mg, $\sim 460nm(2.7eV)$ for Ca and at $\sim 680nm(1.8eV)$ for Au. Although the energetic positions do not fit the experimental values, the sequence of the emission maxima is already reproduced. Moreover the energy sequence can be understood by the considerations mentioned above. The plasmon energy
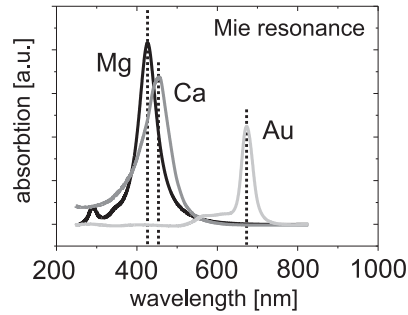
Figure 5.29: Results of the calculation of the plasmon resonance in the frame work of Mie theory. The experimental order is already reproduced by this simple approach. The center position of the peaks does however not fit the experimental results.

for simple metals is given by the respective electron density and the lower plasmon value for the Ca, therefore results from its larger lattice parameter compared to the Mg. In the case of the Au the plasmon resonance is further red-shifted, due to the depolarizing influence of the d-electrons, as already described above.

However, the simple picture of Mie-theory is not able to reproduce the experimental values for the particle emissions. This is caused by the poor representation of the actual experimental situation within this model. In order to take into account also the metal tip, the plasmon resonance positions were calculated with the Johansson model of Tip Induced Plasmons(TIP). Although the model geometry, consisting of a metal sphere above a flat surface used there to calculate the TIP energy, is not perfectly reflecting the experimental situation, reasonable results could be obtained. However the model geometry had to be adapted to the experiment, by taking the metal sphere as the particle and the flat surface as the STM tip. Such an assumption is valid, as long as the tip radius is larger than the actual particle diameter. The results of the calculation are shown in figure (5.30).
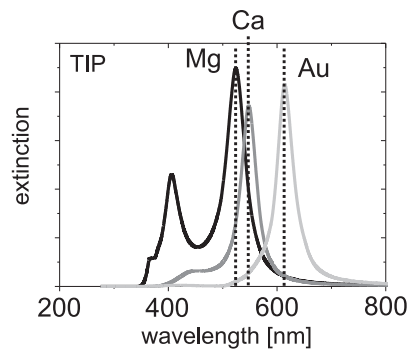
Figure 5.30: Calculation of the tip induced plasmon resonance for the respective materials. The experimental situation is modeled by a metal sphere and a flat surface, being associated with the tip in this case.

All plasmon peaks undergo a significant red-shift due to the presence of the metal tip, which is the result of the strongly increased polarizability of the system. Moreover a new peak is found in the case of the Mg particle at $\sim 410 nm$, which is the plasmon mode of the Ag tip, that appears in addition to the Mg one.
Introducing the influence of the metal tip, via the TIP, leads to a better agreement with the experimental values. Especially, the cut-off wavelength and the respective intensity maxi-

mum is reproduced by these calculations. Therefore the material dependent contribution can be described in the picture of TIP's. However, although the formation of coupled plasmon modes in the tunnel junction is suitable to explain the energy position of the most intense emission line, it fails to describe the additional fine-structure found in the experiment. As pointed out before this is not surprising, since the peak structure seems to have its origin in an intrinsic property of the whole system, whereas the TIP-model only describes the interactions between STM tip and metal particle.

Particle-independent parts of the whole system comprise the tip, the oxide film and the Mo substrate. Since the STM tip was included in the calculation of the TIP and did not induces a peak structure in the respective particle spectra, the investigation needs to be focused on the Mo supported oxide film.

The MgO film is of the same thickness in all experiments and furthermore known to have a strong influence on the transport characteristics of the whole tunnel junction. This was already found for the bare MgO film. To understand how the oxide film can influence the emission characteristic of metal particles, the excitation mechanism of TIP's needs to be considered. The free electron gas in the metal particle is excited by electrons tunneling from tip to sample. The required energy for the plasmon is hereby provided by inelastic tunneling processes, as sketched in figure (5.31).
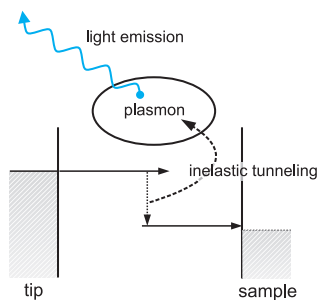

Figure 5.31: Sketch of the light emission mechanism. The electrons which inelastically tunnel from the tip to the sample, transfer the loss energy to the plasmon excitation in the particle. This plasmon then decays via photon emission.

First of all, the region where energy losses take place in the tunnel junction needs to be identified for the particle/oxide system. A scheme of the double barrier junction, that is present in the experiment is shown in figure (5.32). The picture shows two regions were such energy losses can take place, either inside the vacuum barrier or in the MgO film. Energy losses in the metal particle to drive the plasmons are unlikely, due to the presence of several competing decay channels, like phonon excitations or band transition in the metal. Tunneling through such a double barrier junction is defined by the condition, that the current through the whole junction is constant and therefore the tunneling rates at both barriers have to be equal. Otherwise charges would accumulate somewhere inside the junction, which would destabilize the tunneling.

In order to realize the same tunneling rates across both barriers, the only parameter which can be changed at fixed bias is the distance between tip and metal particle. The rate limiting tunneling step for this junction is the electron transport through the oxide barrier, because it is rather large(15Å) and of constant thickness. The potential step across the oxide film might further be increased by a charging of the metal particle in the junction. By this means, the height of the oxide tunneling barrier is lowered and electron transport becomes more efficient. Due to such considerations the MgO film is supposed to be the place where the electron energy losses take place.
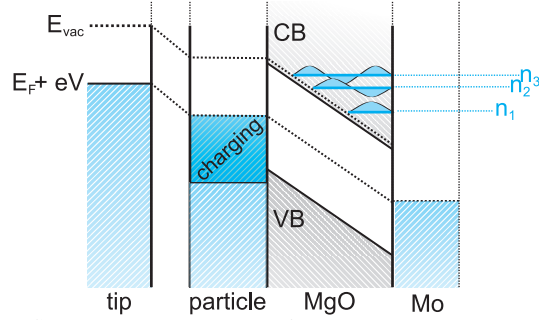
Figure 5.32: Schematic representation of the tunneling junction, consisting of the tip, the metal particle, the MgO film and the Mo substrate. The tunneling characteristics are dominated by the presence of two tunneling barriers and the formation of the triangular potential between particle and substrate, which renders the tunneling properties.

That means, plasmon excitations via inelastic electron tunneling, as the source of the photon emission, is strongly influenced by the transport characteristics through the oxide film. Additionally the probability of inelastic tunneling will be influenced by the density of initial and final states available for this process.

This was already found for the bare MgO film, where the TIP mode could only be excited, if the conduction band onset of the MgO was accessible for the inelastically tunneling electrons. The situation here is similar in the way, that the states in the oxide barrier also influence the possibilities for inelastic energy losses.

The oxide barrier formed between metal particle and Mo substrate has a triangular shape and is therefore suitable to be described in the frame-work of Gundlach resonances. Electron tunneling through this barrier is now strongly enhanced if such Gundlach resonances are available for the transport. Gundlach resonances occur if the associated electron wave-function fits the potential. The energy position within this triangular shaped potential is hereby:

$$E_n = \Phi_s + \left(\frac{\hbar^2}{2m} \right) \left(\frac{3\pi eF}{2} \right)^{2/3} n^{2/3} \tag{5.6}$$

As discussed before Φ_s and F are the work-function and the electric field, respectively. The energy, which can be provided to drive the TIP is now given by the difference between these states. In the case, where a continuous energy transfer of the tunneling electrons to the TIP is possible, only a broad emission band would emerge, that peaks at the calculated position of the plasmon resonance. If however the energy transfer is restricted to quantized energy values, as in this double barrier junction, the single emission band is overlayed with this discrete excitation spectrum.

Consequently the material dependent plasmon resonance is excited only at energy positions, which are compatible with the transport behavior of the junction.

This picture allows a consistent explanation of the experimental results. The observation of different peaks in the spectra can be understood by the fact, that an increased bias leads to tunneling electrons reaching higher Gundlach states. With tunneling into such higher states, more transitions are possible for the inelastic pathway and hence different energies for the TIP excitation.

To further confirm this picture, the energy of the emitted light was fitted with the possible loss energies, given by the difference between the initial Gundlach resonance E_n and the conduction band onset E_{CB} of the MgO as a final state:

$$E_{loss} = E_n - E_{CB} = \Phi_s - E_{CB} + \left(\frac{3\pi\hbar e F}{2\epsilon_{\text{MgO}}\sqrt{2m}} \right)^{2/3} n^{2/3} \tag{5.7}$$

Fitting the photon energies of the fine-structure peaks with the $n^{2/3}$ dependence of the loss energies shows a good agreement. The fit parameter $\Phi_s - E_{CB} = 0,71eV$ is reasonable, if one takes the value of the work-function of the MgO/Mo system($3.3 – 3.9eV$) as reported in the literature[262, 182] and the conduction band onset for a 8 ML thick MgO film($3.1eV$)[263, 197]. The electric field strength extracted form the fitting procedure corresponds to a voltage drop of $6V$ for the 15Å thick MgO film. If one considers an applied voltage for the light emission of $7.5V$, which is a typical value found in the experiments, this means that almost 80% of the potential drops inside the oxide barrier.

This picture also explains, why light emission is observed only for rather high bias, since only for such bias values the electrons are able to occupy the Gundlach states.
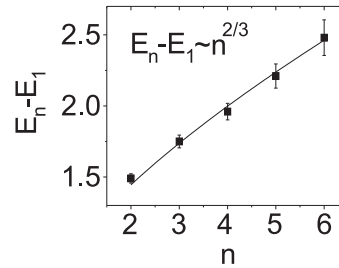
Figure 5.33: Fitting of the photon energies of the observed peaks with the $n^{2/3}$ dependence from the energy positions given by Gundlach equation (5.7)

In summary, the emission mechanism of single metal particles on MgO can be divided into two contributions. One contribution is connected with the actual particle material and gives rise to the appearance of a distinct intensity maximum and a cut-off wavelength in the respective spectra. Both quantities are dependent on the particle material and indicate a photon emission process that is governed by the decay of plasmons. Those energy position depends on the dielectric properties of the metal. The material independent contribution is found in the excitation process of these plasmons. The excitation is done via inelastically tunneling electrons. Since these electrons are confined to quantized transport channels in the tunneling barrier, formed by the oxide film, only specific energies can be provided for the plasmon excitation. This restriction is an intrinsic property of the oxide film and therefore independent of the actual metal particle. The overall spectral response is finally given by the convolution of the material-dependent plasmon emission and the material-independent excitation spectrum of the inelastic tunneling electrons.

5.3 Ag and Mg Particles on MgO: Photon-Map Study

Besides of the energy resolved characterization of the particle light emission, the setup of PSTM also enables the investigation of the spatial distribution of the light emission. Hereby the topographic features of the surface are correlated with the simultaneously acquired photon yield, producing so called photon-maps. Such photon-maps were obtained for Ag, Mg and Ca particles on the MgO film. The possibility to identify positions of strong photon emissions can provide a detailed insight into the properties of the respective surface, as already discussed for the bare MgO film. Work-function changes and the existence of a defect state in the band-gap of the MgO were studied by this approach. Performing similar measurements on particle covered surfaces possibly provides information on the actual field-distribution and the optical active parts of the metal particles. Similar investigation are done for instance in the field of plasmonics, where the geometrical parameters, that leads to certain field enhancements are studied for different particle arrangements[100, 264]. The main difference to this study are the dimensions of the investigated ensembles, which are in the range of some hundred nm large, artificially build ensembles. Furthermore Scanning Optical Near Field Microscopy(SNOM) is usually used to locally detect the emitted light, while the PSTM is a method to locally excite the surface.

Most of the results shown here, are measurements on the Ag system, since particular high emission yields were obtained and stable tunneling conditions was more easily achieved. However, also the Mg and Ca systems could be treated with the relatively harsh tunneling parameters(3-8V, 1–4nA), that are necessary to achieve a reasonable photon flux.

Ag on MgO   Topographic measurements on the Ag particles have shown, that they can be considered as almost perfect nano cubes with an edge length of around $5nm$. This tendency to form cubic particles was found to be even enhanced after sample annealing to $800K$. Since the particle density is smaller in this, also particle-particle interactions are supposed to be smaller. Therefore annealed ensembles are chosen to extract the optical response of an almost undisturbed(by means of inter-particle interactions) particle. Possible effects of such inter-particle interactions were discussed in section (2.3) and furthermore found in the case of more dense ensembles of Mg and Ca particles.
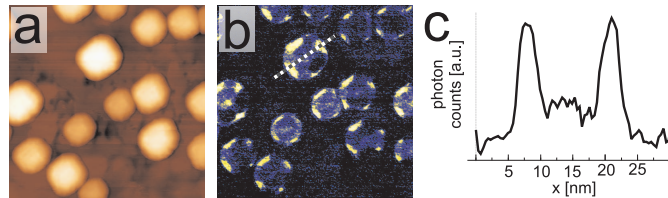
Figure 5.34: **(a)** Topographic image($50 \times 50nm^2$, $4.5V$, $0.02nA$) of Ag particles on a 7 ML thick MgO film. The particles evolve pronounced squared shape with an edge length of 3–6nm. **(b)** Corresponding photon-map emphasizing, that the Ag particles are the optically active species on the surface. Also note the distinct internal structure. **(c)** Photon counts along the line indicated in (b). At this particular bias only at the edges of the particle a high photon intensity is found.

Figure (5.34) shows a topographic image of a 7 ML thick MgO film covered with Ag particles and annealed to $800K$ for $10min$. The image of (5.34.b) shows the corresponding photon-map, whereas a cut along the indicated line is shown on the right side of the figure. From this line-scan it becomes evident, that the photon yield is modulated within the particle, leading to regions of high(yellow) and low(black) intensity.

Since the light emission of a metal particle is governed by the excitation and radiative decay of particle plasmons, one would expect to find the whole particle to become bright. In fact,

the direct correlation of photon yield and topographic position reveals a sudden increase of the emission intensity, when the particle is scanned by the tip, whereas almost no photon flux is recorded on the bare MgO surface. It has to be recognized, that the photon yield within the particle is not constant, but shows a distinct structure over the particle area. This is surprising, because a plasmon is not a localized excitation, but affects the whole particle, although the excitation is performed on a local scale. This unusual behavior was studied in more detail on single particles, in order to have more stable tunneling conditions and to resolve internal structure in the photon yield more clearly.

The results of such a single particle study is shown in figure (5.35), which shows the topographic image together with the corresponding photon-map as a function of bias. The particle has an edges length of $4nm$ and a height of $\sim 3nm$. This height is measured at a voltage of $4.5V$, but actually shows a pronounced bias dependence, as indicated by the two STM images at $5.5V$ and $7.8V$. If the bias is increased the topographic height decreases. The value of $3nm$ therefore represents the maximum height measured at $4.5V$.
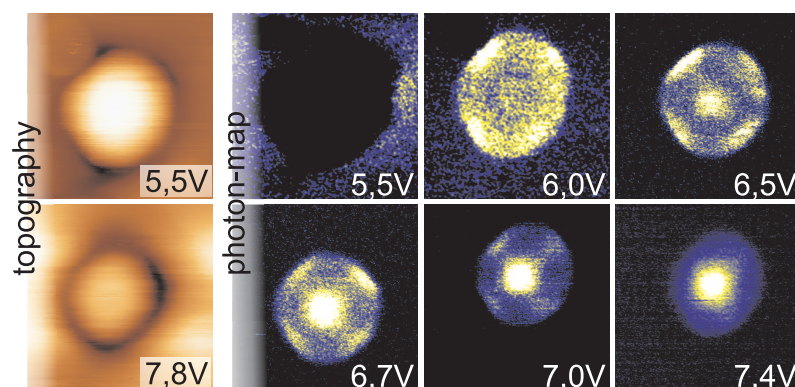

Figure 5.35: STM topographic images(left row) of a single Ag particle on 7ML thick MgO for two different biases($1nA$, $8 \times 8nm^2$). At the right side the corresponding photon-maps are shown, recorded simultaneously with the topographic image at the indicated bias. Whereas at $5.5V$ only the MgO is bright, pronounced contrast changes evolve with increasing sample bias.

With increasing bias a distinct contrast change is observed in the photon signal. Starting at lower bias($5 - 6V$) the particle is found to be dark, while the MgO is bright. This observation is in agreement with the experimental results obtained on the bare MgO film, discussed in section (4.1.5). At around $6V$ light emission of the particle sets in, which leads to a contrast change in the photon-map. Since the emission intensity of the particle is much stronger, the MgO appears dark. However, the bright area found in the photon-maps does not just reproduce the dimensions of the particle, but shows a distinct internal structure. Not the central regions of the particle is found to become bright, as expected from the better field enhancement at this position, but the four side facets of the deposit. With further increase of the bias the central part of the particle becomes bright as well and at $\sim 7V$ the four-fold symmetry of the bright edge regions has vanished.

Optical activity of the particle is found up to a bias of $9V$, although the emission intensity decreases already at $\sim 7V$. The observed contrast change is a real change in the spatial distribution of bright areas, as the photon intensity of the different regions(if they are active) are comparable. Furthermore, the particle corners stay dark over the entire bias range.

In order to rationalize the spatial distribution of the emitted photons, also spectroscopic measurements on such particles were performed. The results are shown in figure (5.36), which shows optical spectra taken at the different positions of the particle. The respective spectra were obtained at $6.5V$ and $7.9V$, where either the side facets or the central part were found to be most active in the photon-map. The spectrum taken at the side facet of
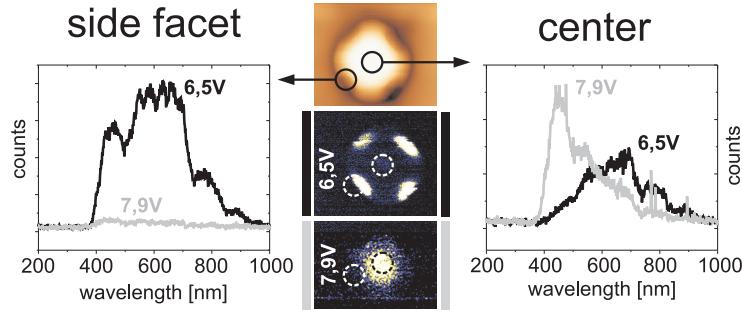
Figure 5.36: Spectra taken at the indicated position plus corresponding phtonmap taken at 6.5 V and 7.9 V

the particle at $6.5V$ exhibits three different emission bands, one emission at $450nm(2.75eV)$ with a FHWM of $0.6eV$, a band at $600nm(2.1eV)$ of $0.6eV$ FWHM and an emission at $760nm(1.65eV)$ with a FWHM of $0.2eV$. The $600nm$ emission in addition shows a distinct fine structure overlayed to the broad emission maximum. This structure consists of four narrow peaks, which are almost equally separated by $\sim 0.1eV$. At this state of the experiments the origin of this fine structure could not be clarified. Different mechanisms could be possible, e.g. the presence of Gundlach states as discussed already for the Mg, Ca and Au particles. Also a convolution with the excitation spectrum of Mg phonons is plausible, whereby the MgO Fuchs-Kliewer mode[265] at $80meV$ would be the most likely excitation. Alternatively, Coulomb blockade effects experienced by the inelastically tunneling electrons could be responsible. Also here, the Coulomb charging energy of $80meV$ fits well with the observed fine-structure. A more detailed investigation is needed at this point to rule out the responsible mechanism. Up to now only the emergence of the three different emission bands, as evident form the presented spectra is discussed.

If the side facets are excited at $7.9eV$ the photon yield has significantly decreased. The respective spectra does not exhibit any strong emission bands anymore. This behavior is compatible with the respective photon-maps of this particle.

Recording the spectroscopic data at the central position of the particle, results in an almost opposite intensity behavior for these two bias values. At $6.5V$ the spectrum exhibits only two emission bands, at $760nm$ and at $600nm$, which is again overlayed with the fine structure. The emission band at $470nm$ is not found in the spectrum and furthermore the overall emission intensity is much lower than at the facets. For $7.9V$ the spectrum shows two emission bands at $470nm$ and $600nm$, whereas the high energy emission is much more intense.

Although, we lack a statistical relevant number of single-particle spectra to draw a correlation between the particle geometry and the optical response, the appearance of the three emission bands is found for all particles investigated in this study. Therefore these emissions are discussed as the optical response of the particles. This response is governed by plasmonic excitations, which are known to be particularly strong for noble metal particles[5]. The Mie-plasmon for a silver particle can be calculated hereby in a model geometry of a metallic sphere on the MgO film using the Granfilm software[37]. Due to the polarizable MgO film, the three degenerated plasmon modes of a perfect sphere split into two energetically separated modes, one oscillating perpendicular to the surface and two in-plane modes, which are degenerated. This separation is clearly found in the calculated absorbance of a $5nm$ Ag sphere shown in figure (5.37). The in-plane mode occurs at $445nm(2.8eV)$ and the out of plane mode is at $350nm(3.5eV)$. The results are roughly $0.7eV$ higher than the experimentally observed values, due to the neglection of the tip influence in this calculation. That the additional polarizability of the tip, can have a strong impact on the emission characteristics of a tunnel
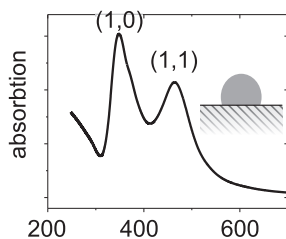
Figure 5.37: Calculated absorption spectra of a Ag particle of $5nm$ diameter supported on MgO(001).

junction was demonstrated in section (2.1). Hereby the tip-sample junction provides a certain energy window for the field enhancement that depends on tip and sample material, as well as on the geometry of the junction. It can be calculated in the frame-work of tip induced plasmons and gives an energy range from $1.5 - 3.7eV$ for the Ag-tip/Mo-sample system used in this experiment. Furthermore the tip influences the optical response by its additional polarizability, which leads to the observed red-shift of the emission features in comparison to the isolated particle/substrate system.

An explanation of the observed emission data can now be obtained by taking the intrinsic optical properties of the Ag particles and the role of the tip into account.

The low-energy emission at $1.65eV$ is hereby attributed to radiative electron transitions between FER's, as already discussed for the light emission of the bare MgO film. This assignment is reasonable, because the emission band is found with even higher intensity, if the tip is placed over the MgO film, but vanishes at the particle center. In the proximity to the particle this emission decreases in intensity, but still contributes to the spectra, taken at the side facets.

The other emission bands in the spectra are assigned to the two plasmon modes of the particle. Whereas it has to be pointed out, that the set of peaks, which were used to fit the optical response of the other particle system in section (4.1.5) are sufficient for fitting, also in this case. However, the fact that at different positions on the particle the relative intensities change is attributed to the excitations of different plasmon modes.

This high energy out of plane mode at $400nm(3.1eV)$ and the in-plane mode at $600nm$ are red- shifted with respect to the calculated values. A shift of the resonance position by $0.7eV$ is however compatible with the anticipated influence of the STM cavity on the particle polarizability.

In order to understand the recorded photon-maps and especially the bias dependent contrast change, one furthermore has to take into account geometric considerations. In particular it has to noted, that the photon-maps do not represent the places of photon emission, but of excitation. More precisely the nm-spatial resolution is given by the size of the electron-beam, that means the actual position of the excitation source with respect to the particle surface. The detection of the emitted light on the other hand has only a resolution of the size of the parabolic mirror's focal point($0.1mm$). Combining the information of the most effective excitation position and the respective energy positions of the emitted light, it is possible to identify the different plasmon modes of the particle. Thereby the geometric restrictions give the conditions for the excitation of the (1,0)- or the (1,1)-mode. The actual geometry of such a tunnel junction is shown in figure (5.38).

The crucial parameter is the point of "contact" between the almost cube like particle and the tip. Whereas the electrons tunnel vertically into the MgO, the situation changes abruptly
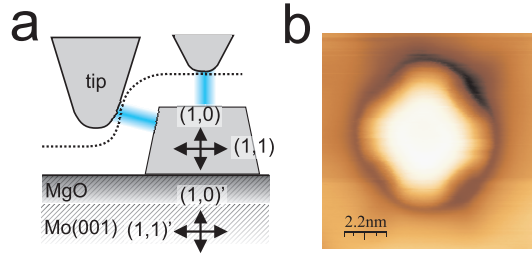
Figure 5.38: **(a)** Schematic representation of the geometry formed by the tip, the particle and the surface, indicating that horizontal tunneling into the particle is only possible at distinct tip positions. **(b)** Topographic image($10 \times 10 nm^2$, $6.7V$, $1.2nA$) of a Ag particle, exhibiting concave side facet, indicating that the tip is closer to the particle at these positions.

at the point, where the tunneling becomes almost horizontal into the particle. The electrons hereby carry a large horizontal dipole moment, which can efficiently excite the (1,1)-plasmon mode of the particle. Accordingly the low energy emission band of the (1,1)-mode shows up in the spectra, taken at the particle edges. From this geometrical consideration it becomes clear, that this condition for horizontal electron injection is only fulfilled in a small spatial window. This is reflected by the rather narrow regions found at the four sides of the particle in the photon-maps. Only at this position the actual geometry between tip and particle enables the excitation of the in-plane mode. The observation of this mode is surprising, because this in-plane mode with its dipole moment parallel to the surface is usually efficiently quenched by the image dipole formed in the metal substrate underneath. In this particular case the oxide film seems to act as a spacer layer between the metal and the particle and prevents or reduces the formation of the image dipole. Also a transport phenomenon might promote the visibility of this mode. The topographic images of these particle reveal a concave shape of the side facets at higher biases(figure (5.38)). This indicates a further approach of the tip to the particle at these positions. Therefore the distance between tip and side facet is further reduced and the associated electromagnetic near field is increased. Such a near field enhancement also increases the cross section for the excitation of the in-plane mode of the particle.

The special tip-particle arrangement to excite the (1,1)-mode also explains the bias dependent behavior of this emission. If the bias increases, the tip has to retract from the surface in order to stabilize the constant current. If however the distance to the particle increases, also the associated efficiency for horizontal electron tunneling into the side facet is reduced and finally not possible anymore, as sketched in figure (5.38.b). Therefore the (1,1)-plasmon mode is not observed at higher bias. The geometric restriction is less severe for the (1,0)-mode, which is excited by electrons tunneling perpendicular to the surface and provide a vertical dipole moment.

One observation is however surprising for the excitation behavior of such particles. Although the emission band associated with the (1,0)-mode is found at the position of the side facets at $6.5V$, it is not visible in the spectra taken above the particle at the same bias. This observation can be rationalized in the framework of a double barrier tunnel junction, as discussed before. Hereby the energy for the excitation of the particle plasmon is provided by inelastic tunneling. These inelastic tunneling processes can only provide a maximum energy, which is given by the actual voltage drop within one of the two barriers(vacuum- and oxide-barrier). Whereas $\sim 70\%$ of the voltage drop at the vacuum barrier, a large drop is also associated with the oxide barrier, since the voltage division is given by the thickness and the respective dielectric constants of the barriers:

$$\frac{d_{\mathrm{vac}}/\epsilon_{\mathrm{vac}}}{d_{\mathrm{MgO}}/\epsilon_{\mathrm{MgO}}} = \frac{U_{\mathrm{vac}}}{U_{\mathrm{MgO}}} = \frac{5/1}{20/10} = \frac{5}{2} \tag{5.8}$$

However the voltage drop at the MgO film might be larger, due to the charging of the metal particle, still it is not sufficient to excite the high energy mode, if the tip is placed above the central position of the particle. In contrast, most of the voltage drops within the vacuum barrier for the tip positioned at the side of the particle. Now the particle is not positioned between the tip and the oxide, so not in the maximum field gradient and its Fermi level will thus be closer to the Mo support. The resulting potential step in the vacuum barrier might allow inelastic electron transitions, which are sufficient to drive the (1,1), as well as the (1,0)-mode. Therefore the observation of the respective plasmon modes is linked to both, the actual inclination of the injected electrons, as well as the potential drop present in the double barrier system.

In the light of this distinct excitation behavior for a single particle, one can conclude, that the actual arrangement of tip and neighboring metal particles, is of crucial importance for the observed light emission. Such an effect will be even more pronounced, if the particles themselves form certain constellations, which might give rise to a large field enhancement on the surface. This effect could be studied on the Mg and Ca particles on MgO, which were prepared with higher particle densities.

Mg and Ca Particles on MgO Some general observation shall be discussed in the following, which involve Mg and Ca systems. The focus was hereby put on non-annealed preparations of rather high coverage. In this case the interactions between the particles is supposed to be larger, which might result in a difference of their actual optical response.

Figure (5.39) and (5.40) shows the topographic images of Mg and Ca particles on the MgO, respectively. Hereby the poorer resolution reflects the more crude tunneling conditions that are necessary to produces the photon-maps, shown in the lower rows of the figures. These examples have been chosen in order to indicated two effects, which could be observed on such systems quiet frequently.

For the Mg particles the spatial distribution of the light emission shows an almost uniform character, with only little intensity emitted from the different particles. However the photon-map exhibits positions of much higher intensity. Surprisingly, these very bright regions do not correspond with the position of a particle. If the correlation with the topographic images is done carefully, it turns out, that the most intense emissions can be found at gap positions between a number of adjacent aggregates. This is indicated in figure (5.41), where a topographic image and corresponding photon-map is shown, together with a cut along the same line in both measurements. By this means the photon yield can be correlated directly with the topographic features.

For the Ca particles the very same behavior can be found. Again, the optically most intense emission is excited at positions, which do not coincide with a particle. Figure (5.39) even shows a photon-map were only a single particle is found to show high photon intensity.

This effect can be understood by considering the actual field enhancement. The system consisting out of metal particles and a metallic tip forms a cavity, which strongly promotes local optical near fields of high intensity. These plasmon-enhanced near fields are for instance considered as the basic requirement for "surface enhanced" Raman scattering(SERS)[266]. Furthermore it is known, that metal particle arrangements, rough surfaces or extended fractal metal objects can exhibit strongly enhanced optical near fields, which are very localized and often referred to as "hot spots"[100]. Usually this kind of measurements are done with a Scanning Near-field Optical Microscope(SNOM)-technique. Although its actual resolution can go down to $\sim 10nm$, the studied metal structures are usually larger than the metal particles investigated in this work. Furthermore this technique probes the light scattering efficiency, which can be influenced by the local field enhancement. Nevertheless, also the PSTM can in principle also probe the optical near field via the emission response.
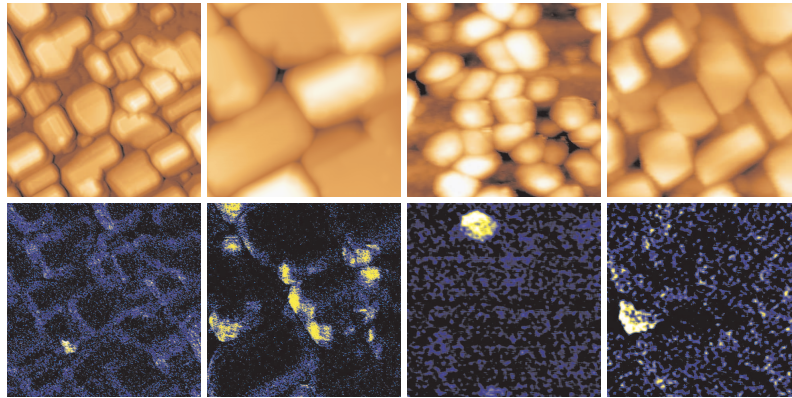
Figure 5.39: STM topographic images($75\times75nm^2$, $1-2\ nA$, $5-7V$) of Mg particles on 7ML thick MgO, whereby the Mg dosage varies. Below the STM images are the respective photon-maps, that indicate on light emission on the surface, besides for specific positions, where the particle arrangement results in the formation of "hot-spots".

Figure 5.40: STM topographic images($75\times75nm^2$, $1-2\ nA$, $5-7V$) of Mg particles on 7ML thick MgO, whereby the Mg dosage varies. Below the STM images are the respective photon-maps, that indicate on light emission on the surface, besides for specific positions, where the particle arrangement results in the formation of "hot-spots".
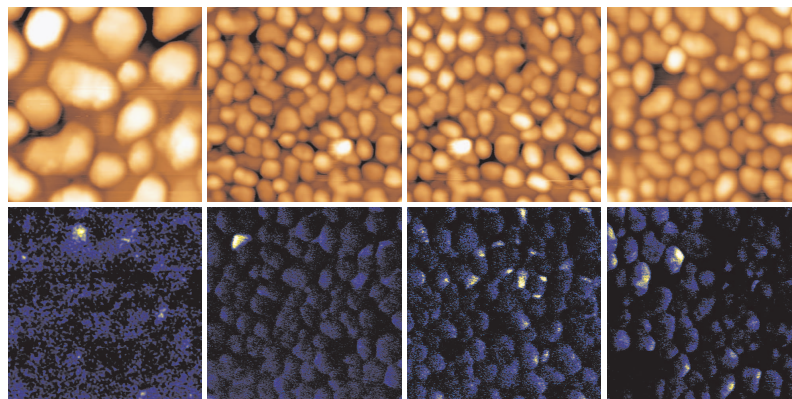
If the tip approaches the particle-covered surface, it always forms a cavity, which in the most simplest case, is represented by two metal spheres above each over. The corresponding field enhancement is calculated in the model of Johansson[135] for example. However, if the tip scans a surface exhibiting a large number of differently sized and shaped metal particles, the actual geometry of the cavity always changes.

In the case of Mg and Ca particles on the MgO, this results in a complex variation in the field enhancement. The positions of large photon yield are now interpreted as positions at which the geometry formed by the particles gives rise to a strong optical near field. Such highly confined near fields are expected to be present in the gap region of resonant particles and were found for example by introducing molecules into these plasmon resonators[267]. Calculations showed, that the field enhancement in such cavities can be several hundred-times stronger than for flat geometries[268]. This confined regions of strong enhancement could also be found experimentally by scattering SNOM on Au particles[269]. However the actual position at which such strong enhancement effects occur can not be determined in advance. Certainly not only the shape of the tip and the gap region determines the near field, but also the constellation of the particles adjacent to the "hot spot" position[100]. This is for instance visible in figure (5.40), where the Ca particles form dense protrusions almost on the whole surface. But the corresponding photon-maps indicates a strong light emission
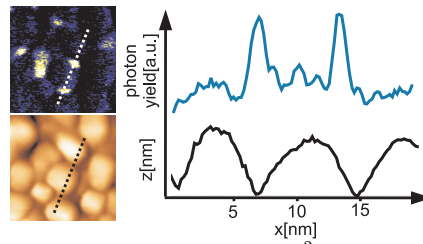
Figure 5.41: Topographic images($35 \times 35 nm^2$, $5V$, $1.5nA$) of Ca particles on MgO with the corresponding photon-map above(**left**). On the **right** side the respective line-scan is shown, indicating the correlation of the formation of a gap between the particles and the observation of light.

only at one particular area. At this point the particle constellation seems to provide the right geometry, for an efficient increase of the optical near field.

In order to investigate these effects more systematically it would be important to acquire a statistically relevant amount of data. Furthermore, also the artificial creation of different structures could be envisioned by using template effects of the substrate. With such artificial structures, a more systematic study of field-enhancement effects could be preformed, e.g. as a function of tip shape, STM bias voltage or current. Additionally, molecules could be placed in such cavities to produce stimulated optical responses with the tip. In general artificially produced structure, that show this kind of field enhancement effects could have an enormous importance in the development of photo-catalytic applications.

Chapter 6

Summary and Outlook

In the first part of this work the investigations on the morphological and optical properties of bare MgO films by means of PSTM, LEED and GIXD had been discussed. The growth behavior of the MgO for different thicknesses was evaluated, leading to a comprehensive model, which allows the explanation of the experimental results at all investigated coverages. The strain, introduced by the lattice mismatch between the MgO and the Mo substrate was found to strongly influence the growth. At all different thickness regimes discussed here, relaxation of the film is the driving force for the development of the specific topographic features. Hereby the different morphology of the films was investigated at sub-monolayer, intermediate and higher coverages, identifying the formation of small MgO patches, a distinct periodic dislocation network and the development of step and screw dislocations to be the relaxation mechanisms. Furthermore the electronic properties of these films were investigated. Hereby, line-defects on the 7ML thick MgO film were found to exhibit a higher work-function, as revealed from dI/dV spectra. The higher work-function however, results from the ability of these sites to trap electrons. Such trapped electrons lead to a negative surface dipole and hence to an increased work-function. This experimental results are in line with the theoretical prediction by Shluger $et~al.$[196]. Local work-function changes were also used to explain the contrast formation in photon-maps of the MgO film and influence the light emission. In both cases, the emission response is governed by electronic transitions between Field Emission Resonances that depend on the local work function and make this quantitative accessible to the experiment.

In order to tailor the optical properties of oxide materials and furthermore to establish other metal-oxides films for a systematic investigation of particle-substrate interactions, two approaches were taken within this work. On the one hand, Li-doping of the MgO films was performed. The doping was found to result in a red-shift of the MgO emission bands. Moreover the temperature dependent morphology of these films was studied. It was shown that at low temperature and concentration the Li is incorporated into the MgO. It segregates however to the surface upon annealing, whereby Li-MgO islands and phase separated Li_xO particles develop. At even higher temperatures($1050K$) the particles desorb and leave behind a distinct pattern of rectangular holes in the MgO surface. However, not all of the Li is removed from the MgO matrix, as indicated by the optical data that still exhibits a red-shift of the MgO emission, assigned to the presence of Li-dopants. The experimental findings could be consistently described with DFT results, obtained in a collaboration with the theory department of the FHI. A further aspect of this study was the preparations of Li-doped MgO as a model system for the oxidative coupling of methane in heterogeneous catalysis. Those chemically oriented experiments were performed within the UNICAT initiative of the Berlin universities and research centers.

In a second approach, other oxide films were prepared on the Mo(001) substrate, e.g. CaO and Li_2O. The CaO growth follows a Stranski-Krastanow behavior, starting with a layer by layer growth and forming CaO islands at higher coverages. The interface layer hereby exhibits a pronounced (2×2) super-structure, as indicated in LEED and also found in the STM images. The formation of this super-structure, as well as the overall growth behavior is related to the rather large lattice mismatch of 8.1% with the Mo. The atomic structure and stoichiometry of the interface layer, could not be clarified in this work, although first model structures were proposed in collaboration with the group of Prof. G. Pacchioni from the university of Milan. More experimental and theoretical work is needed to draw clear conclusion on these questions.

Investigations on Li_2O films did only produce preliminary results. A first procedure to prepare thin Li_2O films could be established. Also in this case a pronounced (2×2) super-structure is found initially, which might be interpreted either in terms of the lattice mismatch or by the formation of a surface alloy, which was also considered in the theoretical models for the CaO.

In the second part of this work, the MgO film was used as a substrate for the deposition of a number of different metals. In particular Mg, Ca, Ni, Ag and Au were deposited and investigated by means of PSTM, LEED and PED. In general the formation of three dimensional particles was observed, whereby the actual morphology showed pronounced differences. Since the MgO films was always prepared at the same conditions, the growth differences could be traced back to the properties of the respective metal. It turned out, that the Young-Duprè approach concerning the respective surface free energies of metal, surface and interface is not sufficient to predict the experimental observations. In order to rationalize the growth behavior, this approach was expanded by a contribution, that accounts for the distortion of the metal-lattice. It was observed that the metal atoms tend to bind at oxygen sites of the underlaying MgO lattice. Occupation of these sites is however associated with a distortion of the metal-lattice. The observed particle morphology reflects the configuration, in which the energy cost of lattice distortion is smallest and energy gain from preferential binding is largest. Only in the case of Au, this simple model failed, as additional effects, e.g. charge transfer from the metal substrate appear, which are not captured by this approach.

The optical characterization of the particle systems lead to different results depending on the applied biases. In the *field emission regime* usually the emission band of the MgO is found in the spectra, in addition to a contribution, that results from plasmon excitations in the deposited metal particles. Hereby the calculation of the plasmon energy with the Mie-theory, were able to explain the observed shifts. In the *tunnel regime* the optical response changed. The spectra, acquired on single metal particles exhibit a broad emission band, that contains an internal peak structure. The peaks were found to appear with increasing bias, but did not show a clear dependence on the particle dimensions. Furthermore, fitting of this peak-structure showed, that the energy positions are independent of the actual particle material. Only the maximum position and the cut-off energy for the broad band were found as a material-dependent contribution. This light emission behavior could be explained within a model, that includes inelastic tunneling transitions in the MgO. These transition are restricted to quantized Gundlach-states. The inelastic tunneling hereby provides the energy for the plasmon excitations in the metal particle, giving rise to the broad material specific emission band. The emissions are therefore determined by an excitation contribution(inelastic tunneling), which only depends on the MgO film and a particle-dependent contribution originating from the radiative decay of particle plasmons.

Also the spatial distribution of the optical response was studied. Hereby a distinct excitation characteristic was found, where only the side or the top facets of the particle were bright in the photon-maps. This excitation behavior is explained by geometric considerations, that influence the actual electron injection into the particle. Whereas in a side-on geometry, in-plane plasmon modes are excited, the out of plane modes are obtained for tip positions above the particle.

For systems with larger particle densities the formation of "hot-spots" was observed. These positions of high-electromagnetic fields were identified in the photon-maps. Whereby its respective position on the surface strongly depends on the actual particle arrangement. Prediction for their appearance are hardly possible, since also the tip is involved in the development of this gap-modes. Further investigations of these field enhancement effects are however interesting, since photo-catalytic processes can be efficiently influenced by these fields. Artificially produced structures, that provide a large number of such sites could thus be promising for photo-catalytic applications.
In oder to prepare such structures, still many important questions have to be answered. This work provided a first attempt for a systematic investigation of those parameters, that determine the growth and the spatial arrangement of metal particles on oxides surfaces. It was possible to draw important correlations between the observed particle geometries and the interfacial properties of the metal and the oxide film. Furthermore, mechanisms of light emission could be identified for the oxide film and the metal particles.

Outlook Besides the possibility to study the same metal particles on other oxides films and to clarify the role of the dielectric substrate on the optical response, some additional perspectives shall be given here. First of all it is necessary to investigate the CaO and Li_2O films in more detail, to gain knowledge on their morphological and optical properties. Within such studies also the doping of oxide films remains an interesting way to tailor the electronic and optical properties. Hereby, other elements apart from Li are envisioned(transition metal atoms). Furthermore the preparation of MgO/CaO hetero-junctions might also used to tailor the excitonic properties and thereby be interesting for photo-catalytic applications.

According to the investigations on metal particles, new insights into the emission characteristics might be gained by providing spectrally resolved photon-maps. This will be possible in future by restricting the energy window of the photomultiplier, with the help of optical band-pass filters. This would allow to map the photon yield at the surface for different photon energies. Since the optical response of the particles was found to depend on the material constants, this could probably provide a method to distinguish different metal particles on the surface via their emission characteristics.

Already started, but not yet fully established, is the construction of a classical optical setup, which enables reflectance and luminescence measurements on a non-local scale. By the comparison of spatially averaged spectra with data obtained by PSTM, it becomes possible to study the influence of the STM-tip on the light emission in more detail. This will certainly allow additional improvements in the understanding of PSTM data.

Bibliography

[1] ANDERSON, P. W.: More is Different. In: *Science* 177 (1972), Nr. 4047, S. 393–396

[2] FREUND, H.-J.: Model Studies in Heterogeneous Catalysis. In: *Chem., A Eur. J.* 16 (2010), S. 9384 – 9397

[3] BÄUMER, M. ; FREUND, H.-J.: Metal deposits on Well-Ordered Oxide Films. In: *Prog. Surf. Sci.* 61 (1999), Nr. 7 – 8, S. 127 – 198

[4] FREUND, H.-J.: Clusters and Islands on Oxides: From Catalysis via Electronics and Magnetism to Optics. In: *Surf. Sci.* 500 (2002), Nr. 1 – 3, S. 271 – 299

[5] KREIBIG, U. ; VOLMER, M.: *Optical properties of metal clusters.* Springer, 1995

[6] MIE, G.: Beiträge zur Optik trüber Medien, speziell kolloidaler Metallösungen. In: *Ann. Phys.* 330 (1908), Nr. 3, S. 377–445

[7] WATANABE, K. ; MENZEL, D. ; NILIUS, N. ; FREUND, H.-J.: Photochemistry on Metal Nanoparticles. In: *Chem. Rev.* 106 (2006), Nr. 10, S. 4301–4320

[8] FREUND, H.-J.: Metal Oxide Surfaces: Electronic Structure and Molecular Adsorption. In: *Phys. Stat. Sol. B* 192 (1995), S. 407–440

[9] CAMPBELL, C.T.: Ultrathin metal films and particles on oxide surfaces: structural, electronic and chemisorptive properties. In: *Surface Science Reports* 27 (1997), Nr. 1–3, S. 1–111

[10] STREET, S.C. ; XU, C. ; GOODMAN, D.W.: The Physical and Chemical Properties of Ultrathin Oxide Films. In: *Ann. Rev. Phys. Chem.* 48 (1997), S. 43–68

[11] HENRY, C.R.: Surface Studies of Supported Model Catalysts. In: *Surf. Sci. Rep.* 31 (1998), Nr. 7–8, S. 231–325

[12] NIEMANTSVERDRIET, J.: Spectroscopy in Catalysis. In: *Wiley-VCH, 2000* (2000)

[13] FREUND, H.-J.: Introductory Lecture: Oxide Surfaces. In: *Farad. Diss.* 114 (1999), Nr. 1

[14] HENRICH, V.E.: The Chemical Physics of Solid Surfaces: Oxide Surfaces. In: *Elsevier, Amsterdam 2001, Edited by D.P. Woodruff* 9 (2001)

[15] ANPO, M. ; YAMADA, Y. ; KUBOKAWA, Y. ; COLUCCIA, S. ; ZECCHINA, A. ; CHE, M.: Photoluminescence Properties of MgO Powders with Coordinatively Unsaturated Surface Ions. In: *J. Chem. Soc., Faraday Trans.1* 84 (1988), S. 751

[16] STANKIC, S. ; MÜLLER, M. ; DIWALD, O. ; STERRER, M. ; KNÖZINGER, E. ; BERNARDI, J.: Size-Dependent Optical Properties of MgO Nanocubes. In: *Angew. Chem. Int. Ed.* 44 (2005), S. 4917

[17] PACCHIONI, G.: The Chemical Physics of Solid Surfaces: Oxide Surfaces. In: *Elsevier, Amsterdam 2001, Edited by D.P. Woodruff* 9 (2001)

[18] BENIA, H.M.: Spatially Resolved Optical Measurements on Supported Metal Particles and Oxide Surfaces with the STM. In: *PHD Thesis* (2008)

[19] ITO, T. ; WANG, J.X. ; LIN, C.H. ; LUNSFORD, J.H.: Oxidative Dimerization of Methane over a Lithium-Promoted Magnesium Oxide Catalyst. In: *J. Am. Chem. Soc.* 107 (1985), Nr. 18, S. 5062–5068

[20] WANG, J.X. ; LUNSFORD, J.H.: Characterization of [Li+O] Centers in Lithium-Doped Magnesium Oxide Catalysts. In: *J. Phys. Chem.* 90 (1986), Nr. 22, S. 5883–5887

[21] ERTL, G.: Reaktionen an Oberflächen: vom Atomaren zum Komplexen (Nobel-Vortrag). In: *Angew. Chem.* 120 (2008), Nr. 19, S. 3578–3590

[22] WATANABE, K. ; MENZEL, D. ; NILIUS, N. ; FREUND, H.-J.: Photochemistry on Metal Nanoparticles. In: *Chem.Rev.* 106 (2006), S. 4301 – 4320

[23] ZHANG, Q. ; TAN, Y.N. ; XIE, J. ; LEE, J.Y.: Colloidal Synthesis of Plasmonic Metallic Nanoparticles. In: *Plasmonics* 4 (2009), Nr. 1, S. 9–22

[24] KREIBIG, U. ; ZACHARIA, P.: Surface Plasma Resonances in small spherical Silver and Gold Particles. In: *Zeitschrift für Physik* 231 (1970), Nr. 2, S. 128

[25] KREIBIG, U. ; SCHMITZ, B. ; BREUER, H.D.: Separation of plasmon-polariton modes of small metal particles. In: *Phys. Rev. B* 36 (1987), Nr. 9, S. 5027–5030

[26] RAETHER, H.: *Surface Plasmons on Smooth and Rough Surfaces and on Gratings.* Bd. 111. Springer Tracts in Modern Physics, 1988

[27] POWELL, C.J. ; SWAN, J.B.: Effect of Oxidation on the Characteristic Loss Spectra of Aluminum and Magnesium. In: *Phys. Rev.* 118 (1960), Nr. 3, S. 640–643

[28] KRETSCHMANN, E. ; CALLCOTT, T.A. ; ARAKAWA, E.T.: Theory of Emission-Spectra From Metal-Films Irradiated by Low-Energy Electrons Near Normal Incidence. In: *Surf. Sci.* 91 (1988), Nr. 237

[29] MOSKOVITS, M.: Optical Constants of the Noble Metals. In: *Rev. Mod. Phys.* 957 (1985), Nr. 783

[30] GÖTZ, T. ; HOHEISEL, W. ; VOLLMER, M. ; TRÄGER, F.: Characterization of Large Supported Metal Clusters by Optical Spectroscopy. In: *Z.Phys. D* 33 (1995), Nr. 133

[31] YAMAGUCHIA, T. ; YOSHIDAA, S. ; KINBARA, A.: Optical effect of the substrate on the anomalous absorption of aggregated silver films. In: *Thin Solid Films* 21 (1974), Nr. 1, S. 173 – 187

[32] ROYER, P.: Optical absorbance of silver oblate particles: Substrate and shape effects. In: *Surf Sci* 217 (1989), Nr. 1-2, S. 384 – 402

[33] BOHREN, C.F. ; HUFFMAN, D.R.: Absorption and Scattering of Light by Small Particles. In: *Wiley, New York* (1983)

[34] ABELES, F.: Optical Properties of Solids. In: *North-Holland, Amsterdam* (1972)

[35] BOHREN, C.F. ; HUFFMAN, D.R.: *Absorption and scattering of light by small particles.* New York, Wiley-Interscience, 1983

[36] SIMONSEN, I. ; LAZZARI, R.: Granfilm software. In: *http://web.phys.ntnu.no/ingves/Software/GranFilm/Current/* (2002)

[37] SIMONSEN, I. ; LAZZARI, R.: Granfilm: a Software for Calculating Thin-Layer Dielectric Properties and Fresnel Coefficients. In: *Thin Solid Films* 419 (2002), Nr. 124

[38] DAMEN, T. C. ; SHAH, Jagdeep ; OBERLI, D. Y. ; CHEMLA, D. S. ; CUNNINGHAM, J. E. ; KUO, J. M.: Dynamics of exciton formation and relaxation in GaAs quantum wells. In: *Phys. Rev. B* 42 (1990), Oct, Nr. 12, S. 7434–7438. http://dx.doi.org/10.1103/PhysRevB.42.7434. – DOI 10.1103/PhysRevB.42.7434

[39] KITTEL, Ch.: *Introduction to solid state physics.* Wiley, New York, 1986

[40] WANNIER, GH.: The structure of electronic excitation levels in insulating crystals. In: *Phys. Rev* 52 (1937), S. 0191–0197

[41] MOTT, N. F. ; LITTLETON, M. J.: Conduction in polar crystals. I. Electrolytic conduction in solid salts. In: *Trans. Faraday Soc.* 34 (1938), S. 485 – 499

[42] MOTT, N. F.: Conduction in polar crystals. II. The conduction band and ultra-violet absorption of alkali-halide crystals. In: *Trans. Faraday Soc.* 34 (1938), S. 500 – 506

[43] FRENKEL, J.: On the Transformation of light into Heat in Solids I. In: *Phys. Rev.* 37 (1931), Nr. 1, S. 1744

[44] FRENKEL, J.: On the Transformation of Light into Heat in Solids II. In: *Phys. Rev.* 37 (1931), Nr. 10

[45] HAYNES, J. R.: Experimental Proof of the Existence of a New Electronic Complex in Silicon. In: *Phys. Rev. Lett.* 4 (1960), Apr, Nr. 7, S. 361–363. http://dx.doi.org/10.1103/PhysRevLett.4.361. – DOI 10.1103/PhysRevLett.4.361

[46] MEYER, B. K. ; ALVES, H. ; HOFMANN, D. M. ; KRIEGSEIS, W. ; FORSTER, D. ; BERTRAM, F. ; CHRISTEN, J. ; HOFFMANN, A. ; STRASSBURG, M. ; DWORZAK, M. ; HABOECK, U. ; RODINA, A. V.: Bound exciton and donor-acceptor pair recombinations in ZnO. In: *phys. stat. sol. b* 241 (2004), Nr. 2, S. 231 – 260

[47] KNÖZINGER, E. ; JACOB, K.-H. ; SINGH, S. ; HOFMANN, P.: Hydroxyl Groups as IR Active Surface Probes on MgO Crystallites. In: *Surf. Sci.* 290 (1993), Nr. 388

[48] SPOTO, G. ; GRIBOV, E. N. ; RICCHIARDI, G. ; DAMIN, A. ; SCARANO, D. ; BORDIGA, S. ; LAMBERTI, C. ; ZECCHINA, A.: Carbon Monoxide MgO from Dispersed Solids to Single Crystals: A Review and New Advances. In: *Prog. Surf. Sci.* 76 (2004), Nr. 71

[49] KIM, Y. D. ; STULTZ, J. ; GOODMAN, D. W.: Identification of Defect Sites on MgO(100) Surfaces. In: *Langmuir* 18 (2002), S. 3999

[50] STERRER, M. ; FISCHBACH, E. ; HEYDE, M. ; NILIUS, N. ; RUST, H.-P. ; RISSE, T. ; FREUND, H.-J.: Electron Paramagnetic Resonance and Scanning Tunneling Microscopy Investigations on the Formation of F^+ and F^0 Color Centers on the Surface of Thin MgO(001) Films. In: *J. Phys. Chem. B* 110 (2006), S. 8665

[51] CAULFIELD, K. J. ; COOPER, R. ; BOAS, J. F.: A Temperature Effect in the Luminescence Emission from Electron-Irradiated MgO. In: *J. Chem. Phys.* 92 (1990), S. 6441

[52] HENRICH, V. E.: The Chemical Physics of Solid Surfaces. In: *Elsevier* 9 (2001)

[53] MADELUNG, E.: Das elektrische Feld in Systemen von regelmäßig angeordneten Punktladungen. In: *Phys. Zeitschr.* 19 (1918), S. 524 – 532

[54] COX, P.A. ; WILLIAMS, A.A.: Surface excitons on ionic crystals. In: *Surface Science* 175 (1986), Nr. 2, S. L782 – L786

[55] STANKIC, S. ; BERNARDI, J. ; DIWALD, O. ; KNÖZINGER, E.: Optical Surface Properties and Morphology of MgO and CaO Nanocrystals. In: *J. Phys. Chem. B* 110 (2006), Nr. 28, S. 13866–13871

[56] COLUCCIA, S. ; DEANE, A.M. ; TENCH, A.J.: Photoluminescent spectra of surface states in alkaline earth oxides. In: *J. Chem. Soc., Faraday Trans. 1* 74 (1978), S. 2913 – 2922

[57] COLUCCIA, S. ; TENCH, A. J.: Formation of surface states on strontium oxide powders. In: *J. Chem. Soc., Faraday Trans. 1* 79 (1983), S. 1881 – 1889

[58] TREVISANUTTO, P.E. ; SUSHKO, P.V. ; SHLUGER, A.L. ; BECK, K.M. ; HENYK, M. ; JOLY, A.G. ; HESS, W.P.: A mechanism of photo-induced desorption of oxygen atoms from MgO nano-crystals. In: *Surf. Sci.* 593 (2005), Nr. 1-3, S. 210 – 220

[59] HESS, W.P. ; JOLY, A.G. ; BECK, K.M. ; HENYK, M. ; SUSHKO, P.V. ; TREVISANUTTO, P.E. ; SHLUGER, A.L.: Laser Control of Desorption through Selective Surface Excitation. In: *J. Phys. Chem. B* 109 (2005), Nr. 42, S. 19563–19578

[60] STANKIC, S. ; STERRER, M. ; HOFMANN, P. ; BERNARDI, J. ; DIWALD, O. ; KNÖZINGER, E.: Novel Optical Surface Properties of Ca2+-Doped MgO Nanocrystals. In: *Nano Lett.* 5 (2005), Nr. 10, S. 1889–1893

[61] SHLUGER, Alexander L. ; SUSHKO, Peter V. ; KANTOROVICH, Lev N.: Spectroscopy of low-coordinated surface sites: Theoretical study of MgO. In: *Phys. Rev. B* 59 (1999), Jan, Nr. 3, S. 2417–2430. `http://dx.doi.org/10.1103/PhysRevB.59.2417`. – DOI 10.1103/PhysRevB.59.2417

[62] COLUCCIA, S.: *Adsorption and Catalysis on Oxide Surfaces.* Elsevier, Amsterdam, The Netherlands, 1984

[63] SPOTO, G. ; GRIBOV, E.N. ; RICCHIARDI, G. ; DAMIN, A. ; SCARANO, D. ; BORDIGA, S. ; LAMBERTI, C. ; ZECCHINA, A.: Carbon monoxide MgO from dispersed solids to single crystals: a review and new advances. In: *Prog. Surf. Sci.* 76 (2004), Nr. 3-5, S. 71 – 146

[64] BAILLY, M.L. ; COSTENTIN, G. ; LAURON-PERNOT, H. ; KRAFFT, J.M. ; CHE, M.: Physicochemical and in Situ Photoluminescence Study of the Reversible Transformation of Oxide Ions of Low Coordination into Hydroxyl Groups upon Interaction of Water and Methanol with MgO. In: *J. Phys. Chem. B* 109 (2005), Nr. 6, S. 2404–2413

[65] BAILLY, M.L. ; COSTENTIN, G. ; KRAFFT, J.M. ; CHE, M.: Discrimination of MgO Ions by Means of an Improved In Situ Photoluminescence Cell and of Propyne as Probe Molecule. In: *Catal. Lett.* 92 (2004), Nr. 3-4, S. 101–105

[66] FUJISHIMA, A. ; HONDA, K.: Electrochemical Photolysis of Water at a Semiconductor Electrode. In: *Nature* 37 (1972), S. 238

[67] FOX, M. A. ; DULAY, M. T.: Heterogenous Photocatalysis. In: *Chem. Rev.* 93 (1993), Nr. 1, S. 341 – 357

[68] LINSEBIGLER, A. L. ; LU, G. ; YATES, J. T.: Photocatalysis on TiO_2 Surfaces: Principles, Mechanisms, and Selected Results. In: *Chem. Rev.* 95 (1995), S. 735 – 758

[69] HOFFMANN, M. R. ; MARTIN, S. T. ; CHOI, W. ; BAHNEMANNT, D. W.: Environmental Applications of Semiconductor Photocatalysis. In: *Chem. Rev.* 95 (1995), S. 69 – 96

[70] SERPONE, N. ; PELIZZETTI, E.: title. In: *Wiley Interscience: New York* (1989), S. 565

[71] KALYANASUNDARAM, K. ; GRÄTZEL, M. ; PELIZZETTI, E.: Ed. Energy Resources Through Photochemistry and Catalysis. In: *Coord. Chem. Reu.* 69 (1986), Nr. 57

[72] GRÄTZEL, M.: Ed. Energy Resources Through Photochemistry and Catalysis. In: *Academic Press: New York* 207 (1983), Nr. 139

[73] BARD, A. J.: Photoelectrochemistry and Heterogeneous Photocatalysis at Semiconductors. In: *J. Photochem.* 10 (1979), Nr. 59

[74] BARD, A. J.: Photoelectrochemistry. In: *Science* 207 (1980), Nr. 139

[75] BARD, A. J.: Design of Semiconductor Photo-Electrochemical Systems for Solar-Energy Conversion. In: *J. Phys. Chem.* 86 (1982), S. 172

[76] NAZIN, G. V. ; QIU, X. H. ; HO, W.: Atomic Engineering of Photon Emission with a Scanning Tunneling Microscope. In: *Phys. Rev. Lett.* 90 (2003), Nr. 216110-1

[77] ASAHI, R. ; MORIKAWA, T. ; OHWAKI, T. ; AOKI, K. ; TAGA, Y.: Visible-Light Photocatalysis in Nitrogen-Doped Titanium Oxides. In: *Science* 294 (2001), S. 269 – 271

[78] NAKAMURA, R. ; TANAKA, T. ; NAKATO, Y.: Mechanism for Visible Light Responses in Anodic Photocurrents at N-doped TiO_2 Film Electrodes. In: *J. Phys. Chem. B.* 108 (2004), S. 10617 – 10620

[79] IRIE, H. ; WATANABE, Y. ; HASHIMOTO, K.: Nitrogen-Concentration Dependence on Photocatalytic Activity of $TiO_{2-x}N_x$ Powders. In: *J. Phys. Chem. B.* 107 (2003), S. 5483 – 5486

[80] OREGAN, B. ; GRÄTZEL, M.: A Low-Cost, High-Efficiency Solar-Cell Based on Dye-Sensitized Colloidal TiO_2 Films. In: *Nature* 353 (1991), Nr. 6346, S. 737 – 740

[81] NAZEERUDDIN, M. K. ; KAY, A. ; RODICIO, I. ; HUMPBRY-BAKER, R. ; MÜLLER, E. ; LISKA, P. ; VLACHOPOULOS, N. ; GRÄTZEL, M.: Conversion of Light to Electricity by cis-X_2Bis(2,2'-bipyridyl-4,4'-dicarboxylate)ruthenium(II) Charge-Transfer Sensitizers $(X = Cl^-, Br^-, I^-, CN^-,$ and $SCN^-)$ on Nanocrystalline TiO_2 Electrodes. In: *J. Am. Chem. Soc.* 115 (1991), Nr. 14, S. 6382 – 6390

[82] HAGFELDT, A. ; GRÄTZEL, M.: Light-Induced Redox Reactions in Nanocrystalline Systems. In: *Chem. Rev.* 95 (1995), Nr. 1, S. 49 – 68

[83] CAMPBELL, C. T.: Ultrathin Metal Films on Oxide Surfaces: Structural, Electronic and Chemisorptive Properties. In: *Surf. Sci. Rep.* 227 (1997), S. 1 – 111

[84] FREUND, H.-J.: Adsorption of Gases on Complex Solid Surfaces. In: *Angew. Chem. Int. Ed. Engl.* 36 (1997), S. 452 – 475

[85] HEIZ, U. ; SCHNEIDER, W. D.: Nanoassembled Model Catalysts. In: *J. Phys. D: Appl. Phys.* 3 (2000), Nr. 11, S. R85–R102

[86] WESENDRUP, R. ; SCHRÖDER, D. ; SCHWARZ, H.: Catalytic PT+-Mediated Oxidation of Methane by Molecular-Oxygen in the Gas-Phase. In: *Angew. Chem., Int. Ed.* 33 (1994), Nr. 11, S. 1174–1176

[87] BOHME, D. K. ; SCHWARZ, H.: Gas-Phase Catalysis by Atomic and Cluster Metal Ions: The Ultimate Single-Site Catalysts. In: *Angew. Chem., Int. Ed.* 44 (2005), S. 2336–2354

[88] SOCACIU, L. D. ; HAGEN, J. ; BERNHARDT, T. M. ; WÖSTE, L. ; HEIZ, U. ; HÄKKINEN, H. ; LANDMAN, U.: Catalytic CO Oxidation by Free Au-2(-): Experiment and Theory. In: *J. Am. Chem. Soc.* 125 (2003), Nr. 34, S. 10437–10445

[89] WALLACE, W. T. ; WHETTEN, R. L.: Coadsorption of CO and O_2 on Selected Gold Clusters: Evidence for Efficient Room-Temperature CO_2 Generation. In: *J. Am. Chem. Soc.* 124 (2002), Nr. 25, S. 7499–7505

[90] MADEY, T. ; ZIMMERMANN, F. M. ; R. A. BARTYNSKI, Eds.: DIET-8: Proceedings of the Eighth International Workshop on Desorption Induced by Electron Transitions; San Alfonso, Long Branch, NJ, Sept 27 - Oct 1, 1999. In: *Surf.Sci.* 451 (2000), Nr. 1 – 3

[91] RASEEV, G. ; G. DUJARDIN, Eds.: DIET-9: Proceedings of the Ninth International Workshop on Desorption Induced by Electron Transitions; Aussois, France, Jun 1 – 4, 2002. In: *Surf.Sci.* 528 (2002), Nr. 1 – 3

[92] TANIMURA, K. ; H. UEBA, Eds.: DIET-10: Proceedings of the Tenth International Workshop on Desorption Induced by Electron Transitions; Susono, Japan, Nov 8 – 11, 2004. In: *Surf.Sci.* 593 (2005), Nr. 1 – 3

[93] KITTEL, C.: Quantum Theory of Solids. In: *Wiley: New York* (1963)

[94] WIECK, G. ; MOLINA, R. A. ; WEINMANN, D. ; JALABERT, R.: Lifetime of the First and Second Collective Excitations in Metallic Nanoparticles. In: *Phys.Rev.B* 72 (2005), S. 115410

[95] ZIMMERMANN, F. M. ; HO, W.: State-Resolved Studies of Photochemical Dynamics at Surfaces. In: *Surf. Sci. Rep.* 22 (1995), Nr. 4-6, S. 127–247

[96] SCHULZ, G.: Resonances in Electron-Impact on Diatomic-Molecules. In: *J. Rev. Mod. Phys.* 45 (1973), Nr. 3, S. 423–486

[97] SANCHE, L.: Low-Energy Electron Scattering From Molecules on Surfaces. In: *J. Phys. B* 23 (1990), Nr. 10, S. 1597–1624

[98] ILLENBERGER, E.: Photoionization and Photodetachment. In: *Advanced Series in Physical Chemistry; World Scientific Ed., Singapore* 10B (2000), S. 1063

[99] LISOWSKI, M. ; LOUKAKOS, P. A. ; BOVENSIEPEN, U. ; STÄHLER, J. ; GAHL, C. ; WOLF, M.: Ultra-Fast Dynamics of Electron Thermalization, Cooling and Transport Effects in Ru(001). In: *Appl. Phys. A* 78 (2004), Nr. 2, S. 165–176

[100] GRÉSILLON, S. ; AIGOUY, L. ; BOCCARA, A. C. ; RIVOAL, J. C. ; QUELIN, X. ; DESMAREST, C. ; GADENNE, P. ; SHUBIN, V. A. ; SARYCHEV, A. K. ; SHALAEV, V. M.: Experimental Observation of Localized Optical Excitations in Random Metal-Dielectric Films. In: *Phys. Rev. Lett.* 82 (1999), Nr. 22, S. 4520–4523

[101] BINNIG, G. ; ROHRER, H. ; GERBER, Ch. ; WEIBEL, E.: Surface studies by scanning tunneling microscopy. In: *Phys. Rev. Lett.* 57 (1982), Nr. 49

[102] D., Heuer ; T., Muller ; H., Pfnur ; U., Kohler: Determination of the Adsorption Site of Sulfur on RU(0001) by STM. In: *Surf. Sci.* (1993), Nr. 297

[103] M, Doering ; HP, Rust ; BG, Briner ; AM, Bradshaw: Imaging benzene on nickel and copper 110 surfaces with low temperature STM: the adsorption site. In: *Surf. Sci.* (1998), Nr. 410

[104] WIESENDANGER, R.: Scanning Probe Microscopy and Spectroscopy: Methods and Applications. In: *Cambridge University Press, Cambridge* (1994)

[105] Wiesendanger, R.: Scanning Probe Microscopy and Spectroscopy: Analytical Methods. In: *Springer-Verlag, Berlin, Heidelberg* (1998)

[106] Chen, C. J.: Introduction to Scanning Tunneling Microscopy. In: *Oxford University Press, New York, Oxford* (1993)

[107] Stipe, B. C. ; Rezaei, M. A. ; Ho, W.: Single-Molecule Vibrational Spectroscopy and Microscopy. In: *Science* 280 (1998), S. 1732

[108] Lee, H. J. ; Ho, W.: Single-Bond Formation and Characterization with a Scanning Tunneling Microscope. In: *Science* 286 (1999), S. 1719 – 1722

[109] Pascual, J. I. ; Jackiw, J. J. ; Z.Song ; Weiss, P. S. ; Conrad, H. ; Rust, H.-P.: Adsorbate-Substrate Vibrational Modes of Benzene on Ag(110) Resolved with Scanning Tunneling Spectroscopy. In: *Phys. Rev. Lett.* 86 (2001), S. 1050 – 1053

[110] Pascual, J. I. ; Lorente, N. ; Song, Z. ; Conrad, H. ; Rust, H.-P.: Selectivity in Vibrationally Mediated Single-Molecule Chemistry. In: *Nature* 423 (2003), S. 525 – 528

[111] Wiesendanger, R.: Spin Mapping at the Nanoscale and Atomic Scale. In: *Rev. Mod. Phys.* 81 (2009), Nr. 4, S. 1495 – 1550

[112] Wiesendanger, R. ; Güntherodt, H. J. ; Güntherodt, G. ; Gambino, R. J. ; Ruf, R.: Observation of Vacuum Tunneling of Spin-Polarized Electrons with the Scanning Tunneling Microscope. In: *Phys. Rev. Lett.* 65 (1990), Nr. 2, S. 247–250

[113] Wiesendanger, R. ; Shvets, I. V. ; Bürgler, D. ; Tarrach, G. ; Güntherodt, H. J. ; Coey, J. M. D. ; Gräser, S.: Topographic and Magnetic-Sensitive Scanning Tunneling Microscope Study of Magnetite. In: *Science* 255 (1992), S. 583

[114] Bode, M.: Spin-Polarized Scanning Tunnelling Microscopy. In: *Rep. Prog. Phys.* 66 (2003), Nr. 4, S. 523–582

[115] Lippmaa, M. ; Kawasaki, M. ; Ohtomo, A. ; Sato, T. ; Iwatsuki, M. ; Koinuma, H.: Observation of SrTiO step edge dynamics by real-time high-temperature STM. In: *Appl. Surf. Sci. 130* 582 (1998), Nr. 130

[116] Kambara, H. ; Matsui, T. ; Niimi, Y. ; Fukuyama, H.: Construction of a Versatile Ultralow Temperature Scanning Tunneling Microscope. In: *Rev. Sci. Inst.* 78 (2007), Nr. 7, S. 073703

[117] Moussy, N. ; Courtois, H. ; Pannetier, B.: A Very Low Temperature Scanning Tunneling Microscope for the Local Spectroscopy of Mesoscopic Structures. In: *Rev. Sci. Inst.* 72 (2001), Nr. 1, S. 128 – 131

[118] Gurney, R. W. ; Condon, E. U.: Wave Mechanics and Radioactive Disintegration. In: *Nature* 122 (1928), S. 439–439

[119] Wu, Q. H. ; Kang, J.: Applications of Fast Scanning Tunneling Microscopy: A Review. In: *Mat. Manufac. Proc.* 22 (2007), S. 22 – 27

[120] Besenbacher, F. ; Laegsgaard, E. ; Stensgaard, I.: Fast-Scanning STM Studies. In: *Mater. Today* 8 (2005), S. 26 – 30

[121] Besenbacher, F.: Dynamics and Self-Assembly of Organic Molecules on Surfaces Revealed by High-Resolution, Fast-Scanning STM. In: *J. Bio. Technol.* 118 (2005), S. 33 – 34

[122] BARDEEN, J.: Tunneling from a many particle point of view. In: *Phys. Rev. Lett.* 57 (1961), Nr. 6

[123] J. TERSOFF, D.R. H.: Theory and application for the scanning tunneling microscope. In: *Phys. Rev. Lett. 50* 1998 (1983)

[124] J. TERSOFF, D.R. H.: Theory of the scanning tunneling microscope. In: *Phys. Rev. B 31* 805 (1985)

[125] BERNDT, R. ; WIESENDANGER, R.: Scanning Probe Microscopy and Spectroscopy: Analytical methods. In: *Springer-Verlag, Berlin, Heidelberg* (1998)

[126] BERNDT, R. ; GIMZEWSKI, J.K. ; JOHANSSON, P.: Inelastic tunneling excitation of tip-induced plasmon modes on noble-metal surfaces. In: *Phys. Rev. Lett.* 67 (1991), Dec, Nr. 27, S. 3796–3799. http://dx.doi.org/10.1103/PhysRevLett.67.3796. – DOI 10.1103/PhysRevLett.67.3796

[127] NAZIN, G. V. ; QIU, X. H. ; HO., W.: Atomic Engineering of Photon Emission with a Scanning Tunneling Microscope. In: *Phys. Rev. Lett.* 90 (2003), Nr. 21, S. 216110

[128] HOFFMANN, G. ; MAROUTIAN, T. ; BERNDT, R.: Color View of Atomic Highs and Lows in Tunneling Induced Light Emission. In: *Phys. Rev. Lett.* 93 (2004), Nr. 7, S. 076102

[129] NILIUS, N. ; ERNST, N. ; FREUND, H.J.: Photon Emission Spectroscopy of Individual Oxide-Supported Silver Clusters in a Scanning Tunneling Microscope. In: *Phys. Rev. Lett.* 84 (2000), Nr. 17, S. 3994–3997

[130] GIMZEWSKI, J. K. ; REIHL, B. ; COOMBS, J. H. ; SCHLITTLER, R. R.: Photon emission with the scanning tunneling microscope. In: *Zeitschr. Phys. B - Cond. Mat.* 72 (1988), S. 497–501

[131] BERNDT, R. ; GAISCH, R. ; SCHNEIDER, W. D. ; GIMZEWSKI, J. K. ; REIHL, B. ; SCHLITTLER, R. R. ; TSCHUDY, M.: Photon emission from adsorbed C60; molecules with sub-nanometer lateral resolution. In: *Appl. Phys. A: Mat. Sci. Proc.* 57 (1993), S. 513–516

[132] DENG, W. ; FUJITA, D. ; OHGI, T. ; YOKOYAMA, S. ; KAMIKADO, K. ; MASHIKO, S.: STM-induced photon emission from self-assembled porphyrin molecules on a Cu(100) surface. In: *J. Chem. Phys.* 117 (2002), Nr. 10, S. 4995 – 5000

[133] LAMBE, John ; MCCARTHY, S. L.: Light Emission from Inelastic Electron Tunneling. In: *Phys. Rev. Lett.* 37 (1976), Oct, Nr. 14, S. 923–925. http://dx.doi.org/10.1103/PhysRevLett.37.923. – DOI 10.1103/PhysRevLett.37.923

[134] GIMZEWSKI, J: Enhanced Photon-Emission in Scanning Tunneling Microscopy. In: *Europhysics letters* 8 (1989), Nr. 5, S. 435–440

[135] JOHANSSON, P. ; MONREAL, R. ; APELL, P.: Theory for light emission from a scanning tunneling microscope. In: *Phys. Rev. B* 42 (1990), Nov, Nr. 14, S. 9210–9213. http://dx.doi.org/10.1103/PhysRevB.42.9210. – DOI 10.1103/PhysRevB.42.9210

[136] ADAMS, Arnold ; HANSMA, P. K.: Light emission from small metal particles and thin metal films excited by tunneling electrons. In: *Phys. Rev. B* 23 (1981), Apr, Nr. 8, S. 3597–3601. http://dx.doi.org/10.1103/PhysRevB.23.3597. – DOI 10.1103/PhysRevB.23.3597

[137] JOHANSSON, P.: Light emission from a scanning tunneling microscope: Fully retarded calculation. In: *Phys. Rev. B* 58 (1998), Oct, Nr. 16, S. 10823–10834. http://dx.doi.org/10.1103/PhysRevB.58.10823. – DOI 10.1103/PhysRevB.58.10823

[138] TAKEMORI, T.: Optical-Response of a Sphere Coupled to a Metal-Substrate. In: *J. Phys. Soc. Japan* 56 (1987), Nr. 4, S. 1587–1602

[139] RENAUD, G.: Oxide surfaces and metal/oxide interfaces studied by grazing incidence X-ray scattering. In: *Surf.Sci.Rep* 32 (1998), S. 1 – 90

[140] BRENNAN, S. ; EISENBERGER, E.: title. In: *Nucl. Instr. Meth. 222* 164 (1984)

[141] AKIMOTO, K. ; MIZUKI, J. ; HIROSAWA, I. ; MATSUI, J.: title. In: *Rev. Sci. Instr. 60* 2362 (1989)

[142] VLIEG, E. ; ENT, A. V. ; JONGH, A.P. de ; NEERINGS, H. ; VEEN, J.E V.: title. In: *Nucl. Instr. Meth. A 262* 522 (1987)

[143] CLAVERIE, E. ; MASSIES, J. ; PINCHAUX, R. ; SAUVAGE-SIMKIN, M. ; FROUIN, J. ; BONNET, J. ; JEDRECY, N.: title. In: *Rev. Sci. Instr. 60* 2369 (1989)

[144] FERRER, S. ; COMIN, E: title. In: *Rev. Sci. Instr. 66* 1674 (1995)

[145] FUOSSA, EH. ; ROBINSON, I.K.: title. In: *Nucl. Instr. Meth. 222* 171 (1984)

[146] RENAUD, G. ; VILLETTE, B. ; GUÉNARD, P.: title. In: *Nucl. Instr. Meth. B 95* 422 (1995)

[147] BAUDOING-SAVOIS, R. ; RENAUD, G. ; SANTIS, M. D. ; BARBIER, A. ; ROBACH, O. ; TAUNIER, P. ; JEANTET, P. ; ULRICH, O. ; ROUX, J.P. ; SAINT-LAGER, M.C. ; BARSKI, A. ; GEAYMOND, O. ; BERARD, G. ; DOLLE, P. ; NOBLET, M. ; MOUGIN, A.: A new UHV diffractometer for surface structure and real time molecular beam deposition studies with synchrotron radiations at ESRF. In: *Nucl. Instrum. Methods Phys. Res B 149* 213 (1999)

[148] COLLUCCIA, S. ; BARTON, A. ; TENCH, A. J.: Reactivity of Low-Coordination Sites on the Surface of Magnesium Oxide. In: *J. Chem. Soc. Faraday Trans. 1* 77 (1981), S. 2203–2207

[149] HATTORI, H.: Solid Base Catalysts: Generation of Basic Sites and Application to Organic Synthesis. In: *Appl. Catal. A* 222 (2001), S. 247–259

[150] BAILLY, M. L. ; CHIZALLET, C. ; COSTENTIN, G. ; KRAFFT, J. M. ; LAURON-PERNOT, H. ; CHE, M.: A Spectroscopy and Catalysis Study of The Nature of Active Sites of MgO Catalysts: Hermodynamic Bronsted Basicity versus Reactivity of Basic Sites. In: *J. Catal.* 235 (2005), S. 413

[151] VOLODIN, A. M.: Photoinduced Phenomena on The Surface of Wide-Band-Gap Oxide Catalysts. In: *Catal. Today* 58 (2000), S. 103–114

[152] YUASA, S. ; NAGAHAMA, T. ; FUKUSHIMA, A. ; SUZUKI, Y. ; ANDO, K.: Giant Room-Temperature Magnetoresistance in Single-Crystal Fe/Mgo/Fe Magnetic Tunnel Junctions. In: *Nature Materials* 3 (2004), S. 868–871

[153] MATHER, P. G. ; READ, J. C. ; BUHRMAN, R. A.: Disorder, Defects, and Band Gaps in Ultrathin (001) MgO Tunnel Barrier Layers. In: *Phys. Rev. B* 73 (2006), S. 205412

[154] YAMAMOTO, M.: Highly Spin-Polarized Tunneling in Fully Epitaxial Magnetic Tunnel Junctions with a Co-Based Full-Heusler Alloy Thin Film and a MgO Barrier. In: *Advances in Solid State Physics, Springer Berlin/Heidelberg* (2008)

[155] PACCHIONI, G.: The Chemical Physics of Solid Surfaces: Oxide Surfaces. In: *Edited by D.P. Woodruff. Elsevier, Amsterdam* (2001)

[156] HENRICH, V. E. ; DRESELHAUS, G. ; ZEIGER, H. J.: Energy-Dependent Electron-Energy-Loss Spectroscopy: Application to The Surface and Bulk Electronic Structure of MgO. In: *Phys. Rev. B* 22 (1980), S. 47644775

[157] TEGENKAMP, C. ; PFNÜR, H. ; ERNST, W. ; MALASKE, U. ; WOLLSCHLÄGER, J. ; PETERKA, D. ; SCHRÖDER, K. M. ; ZIELASEK, V. ; HENZLER, M.: Defects in Epitaxial Insulating Thin Films. In: *J. Phys. Cond. Mat.* 11 (1999), S. 9943–9954

[158] KNÖZINGER, E. ; JACOB, K.H. ; SINGH, S. ; HOFMANN, P.: Hydroxyl Groups as IR Active Surface Probes on MgO Crystallites. In: *Surf. Sci.* 290 (1993), S. 388–402

[159] SPOTO, G. ; GRIBOV, E. N. ; RICCHIARDI, G. ; DAMIN, A. ; SCARANO, D. ; BORDIGA, S. ; LAMBERTI, C. ; ZECCHINA, A.: Carbon Monoxide MgO from Dispersed Solids to Single Crystals: A Review and New Advances. In: *Prog. Surf. Sci.* 76 (2004), S. 71

[160] KIM, Y. D. ; STULTZ, J. ; GOODMAN, D. W.: Identification of Defect Sites on MgO(100) Surfaces. In: *Langmuir* 18 (2002), S. 3999

[161] STERRER, M. ; HEYDE, M. ; NOVICKI, M. ; NILIUS, N. ; RISSE, T. ; RUST, H.-P. ; PACCHIONI, G. ; FREUND, H.-J.: Identification of Color Centers on MgO(001) Thin Films with Scanning Tunneling Microscopy. In: *J. Phys. Chem. B* 110 (2006), S. 46–49

[162] CAULFIELD, K. J. ; COOPER, R. ; BOAS, J. F.: A Temperature Effect in the Luminescence Emission from Electron-Irradiated MgO. In: *J. Chem. Phys.* 92 (1990), S. 6441–6446

[163] COLLUCIA, S. ; DEAN, A. M. ; TENCH, A. J.: Photoluminescence Spectra of Surface States in Alkaline Earth Oxides. In: *J. Chem. Soc., Faraday Trans. 1* 74 (1978), S. 2913

[164] DIWALD, O. ; STERRER, M. ; KNÖZINGER, E. ; SUCHKO, P. V. ; SHLUGER, A. L.: Wavelength Selective Excitation of Surface Oxygen Anions on Highly Dispersed MgO. In: *J. Chem. Phys.* 116 (2002), S. 1707–1712

[165] WOLLSCHLÄGER, J. ; VIERNOW, J. ; TEGENKAMP, C. ; ERDÖS, D. ; SCHRÖDER, K. M. ; PFNÜR, H.: Stoichiometry and Morphology of MgO Films grown reactively on MgO. In: *Appl. Surf. Sci.* 142 (1999), S. 129–134

[166] SCHINTKE, S. ; MESSERLI, S. ; PIVETTA, M. ; PATTHEY, F. ; LIBIOULLE, L. ; STENGEL, M. ; VITA, A. D. ; SCHNEIDER, W. D.: Insulator at The Ultrathin Limit: MgO on Ag(001). In: *Phys. Rev. Lett.* 87 (2001), S. 276801

[167] VALERI, S. ; ALTIERI, S. ; PENNINO, U. del ; BONA, A. di ; LUCHES, P. ; ROTA., A.: Scanning Tunneling Microscopy of MgO Ultrathin Films on Ag(001). In: *Phys. Rev. B* 65 (2002), S. 245410

[168] MEYERHEIM, H. L. ; POPESCU, R. ; KIRSCHNER, J. ; JEDRECY, N. ; SAUVAGE-SIMKIN, M. ; HEINRICH, B. ; PINCHAUX, R.: Geometrical and Compositional Structure at Metal-Oxide Interfaces: MgO on Fe(001). In: *Phys. Rev. Lett.* 87 (2001), S. 076102

[169] WU, M-C. ; CORNEILLE, J.S. ; ESTRADA, C.A. ; HE, J-W. ; GOODMAN, D.W.: Synthesis and characterization of ultra-thin MgO films on Mo(100). In: *Chem.Phys.Lett.* 182 (1991), Nr. 5, S. 472 – 478

[170] DYNNA, M. ; VASSENT, J.L. ; MARTY, A. ; GILLES, B.: A low-energy electron diffraction investigation of the surface deformation induced by misfit dislocations in thin MgO films grown on Fe(001). In: *J.Appl.Phys.* 80 (1996), Nr. 5, S. 2650–2657

[171] VASSENT, J.L. ; DYNNA, M. ; MARTY, A. ; GILLES, B. ; PATRAT, G.: A study of growth and the relaxation of elastic strain in MgO on Fe(001). In: *J.Appl.Phys.* 80 (1996), Nr. 10, S. 5727

[172] WOLLSCHLÄGER, J. ; ERDÖS, D. ; GOLDBACH, H. ; HÖPKEN, R. ; SCHRÖDER, K. M.: Growth of NiO and MgO Films on Ag(100). In: *Thin Solid Films* 400 (2001), Nr. 1-2, S. 1–8

[173] HENZLER, M.: Growth of epitaxial monolayers. In: *Surface Science* 357-358 (1996), S. 809 – 819

[174] DYNNA, M. ; VASSENT, J. L. ; MARTY, A. ; GILLES, B.: A Low-Energy Electron Diffraction Investigation of The Surface Deformation Induced by Misfit Dislocation in Thin MgO Films Grown on Fe(001). In: *J. App. Phys.* 80 (1996), S. 2650

[175] WOLLSCHLÄGER, J. ; ERDÖS, D. ; GOLDBACH, H. ; SCHRÖDER, K. M.: Growth of NiO and MgO Films on Ag(100). In: *Thin Solid Films* 400 (2001)

[176] BENEDETTI, S. ; TORELLI, P. ; VALERI, S. ; BENIA, H.M. ; NILIUS, N. ; RENAUD, G.: Structure and morphology of thin MgO films on Mo(001). In: *Phys. Rev. B* 78 (2008), Nov, Nr. 19, S. 195411. http://dx.doi.org/10.1103/PhysRevB.78.195411. – DOI 10.1103/PhysRevB.78.195411

[177] BENEDETTI, S. ; LUCHES, P. ; LIBERATI, M. ; VALERI, S.: Chemical reactions and interdiffusion at the Fe/NiO(0 0 1) interface. In: *Surf.Sci.* 572 (2004), Nr. 2-3, S. L348 – L354

[178] HONKALA, K. ; HÄKKINEN, H.: Au Adsorption on Regular and Defected Thin MgO(100) Films Supported by Mo. In: *J. Phys. Chem. C* 111 (2007), Nr. 11, S. 4319–4327

[179] PACCHIONI, G. ; GIORDANO, L. ; BAISTROCCHI, M.: Charging of Metal Atoms on Ultrathin MgO/Mo(100) Films. In: *Phys. Rev. Lett.* 94 (2005), Nr. 22, S. 226104

[180] GONIAKOWSKI, J. ; NOGUERA, C.: Electronic States and Schottky Barrier Height at Metal/MgO(100) Interfaces. In: *Int. Sci.* 12 (2004), S. 93–103

[181] SCHINTKE, S. ; MESSERLI, S. ; PIVETTA, M. ; PATTHEY, F. ; LIBIOULLE, L. ; STENGEL, M. ; VITA, A. D. ; SCHNEIDER, W.D.: Insulator at the Ultrathin Limit: MgO on Ag(001). In: *Phys. Rev. Lett.* 87 (2001), Dec, Nr. 27, S. 276801. http://dx.doi.org/10.1103/PhysRevLett.87.276801. – DOI 10.1103/PhysRevLett.87.276801

[182] GIORDANO, L. ; CINQUINI, F. ; PACCHIONI, G.: Tuning the surface metal work function by deposition of ultrathin oxide films: Density functional calculations. In: *Phys. Rev. B* 73 (2006), Jan, Nr. 4, S. 045414. http://dx.doi.org/10.1103/PhysRevB.73.045414. – DOI 10.1103/PhysRevB.73.045414

[183] SCHINTKE, S. ; SCHNEIDER, W.D.: Insulators at the ultrathin limit: electronic structure studied by scanning tunneling microscopy and scanning tunneling spectroscopy. In: *J.Phys.: Condens.Matter* 16 (2004), Nr. 49

[184] FEENSTRA, R. M. ; THOMPSON, W. A. ; FEIN, A. P.: Real-space observation of π-bonded chains and surface disorder on Si(111)2×1. In: *Phys. Rev. Lett.* 56 (1986), Feb, Nr. 6, S. 608–611. http://dx.doi.org/10.1103/PhysRevLett.56.608. – DOI 10.1103/PhysRevLett.56.608

[185] KÖNIG, T. ; SIMON, G.H. ; RUST, H.P. ; PACCHIONI, G. ; HEYDE, M. ; FREUND, H.J.: Measuring the Charge State of Point Defects on MgO/Ag(001). In: *J.Am.Chem.Soc.* 131 (2009), S. 17544–17545

[186] IBACH, H.: Physics of Surfaces and Interfaces. In: *Springer-Verlag Berlin Heidelberg* (2006)

[187] GUNDLACH, K.H.: Zur berechnung des tunnelstroms durch eine trapezförmige potentialstufe. In: *Solid-State Electronics* 9 (1966), Nr. 10, S. 949 – 957

[188] BINNING, G. ; FRANK, K. H. ; FUCHS, H. ; GARCIA, N. ; REIHL, B. ; ROHRER, H. ; SALVAN, F. ; WILLIAMS, A. R.: Tunneling Spectroscopy and Inverse Photoemission: Image and Field States. In: *Phys. Rev. Lett.* 55 (1985), S. 991–994

[189] KOLESNYSCHENKO, O. Y. ; KOLENSISCHENKO, Y. A. ; SHKLYAREVSKII, O. I. ; KEMPEN, H. van: Field-Emission Resonance Measurements with Mechanically Controlled Break Junctions. In: *Physica B* 291 (2000), S. 246–255

[190] GOMER, R.: Field Emission and Field Ionization. In: *Harvard University Press, Cambridge, Massachusetts* (1961)

[191] RICCI, D. ; BONGIORNO, A. ; PACCHIONI, G. ; LANDMAN, U.: Bonding Trends and Dimensionality Crossover of Gold Nanoclusters on Metal-Supported MgO Thin Films. In: *Phys. Rev. Lett.* 97 (2006), Nr. 3, S. 036106

[192] STERRER, M. ; RISSE, T. ; HEYDE, M. ; RUST, H.P. ; FREUND, H.-J.: Crossover from Three-Dimensional to Two-Dimensional Geometries of Au Nanostructures on Thin MgO(001) Films: A Confirmation of Theoretical Predictions. In: *Phys. Rev. Lett.* 98 (2007), Nr. 20, S. 206103

[193] YOON, B. ; HÄKKINEN, H. ; LANDMAN, U. ; WORZ, A. S. ; ANTONIETTI, J.-M. ; ABBET, S. ; JUDAI, K. ; HEIZ, U.: Charging Effects on Bonding and Catalyzed Oxidation of CO on Au8 Clusters on MgO. In: *Science* 307 (2005), S. 403 – 407

[194] HARUTA, M. ; KOBAYASHI, T. ; SANO, H. ; YAMADA, N.: Novel Gold Catalysts for the Oxidation of Carbon Monoxide at a Temperature far Below 0°C. In: *Chem. Lett.* 16 (1987), S. 405 – 408

[195] HARUTA, M.: Size- and Support-Dependency in the Catalysis of Gold. In: *Catal. Today* 36 (1997), S. 153 – 166

[196] MCKENNA, K. P. ; SHLUGER, A. L.: Electron-Trapping Polycrystalline Materials with Negative Electron Affinity. In: *Nat. Mater.* 7 (2008), S. 859–862

[197] BENIA, H.M. ; MYRACH, P. ; NILIUS, N.: Photon emission spectroscopy of thin MgO films with the STM: from a tip-mediated to an intrinsic emission characteristic. In: *New Journal of Physics* 10 (2008), Nr. 1, S. 013010

[198] BENEDETTI, S. ; BENIA, H.M. ; NILIUS, N. ; VALERI, S. ; FREUND, H.J.: Morphology and optical properties of MgO thin films on Mo(001). In: *Chemical Physics Letters* 430 (2006), Nr. 4–6, S. 330–335

[199] SCHINTKE, S. ; MESSERLI, S. ; PIVETTA, M. ; PATTHEY, F. ; LIBIOULLE, L. ; STENGEL, M. ; VITA, A. D. ; SCHNEIDER, W.D.: Insulator at the Ultrathin Limit: MgO on Ag(001). In: *Phys. Rev. Lett.* 87 (2001), S. 276801

[200] FRITSCH, D. ; SCHMIDT, H. ; GRUNDMANN, M.: Pseudopotential band structures of rocksalt MgO, ZnO, and $Mg_{1-x}Zn_xO$. In: *Appl. Phys. Lett.* 88 (2006), S. 134104

[201] HENRICH, V. E. ; DRESSELHAUS, G. ; ZEIGER, H. J.: Energy-Dependent Electron-Energy-Loss Spectroscopy: Application to the Surface and Bulk Electronic Structure of MgO. In: *Phys. Rev. B* 22 (1980), S. 4764 – 4775

[202] MORALES, E. ; LUNSFORD, J. H.: Oxidative Dehydrogenation of Ethane over a Lithum-promoted Magnesium-Oxide Catalyst. In: *J. Catal.* 118 (1989), Nr. 1, S. 255–265

[203] ITO, T. ; LUNSFORD, J. H.: Synthesis of Ethylene and Ethane by Partial Oxidation of Methane over Lithium-doped Magnesium-Oxide. In: *Nature* 314 (1985), Nr. 6013, S. 721–722

[204] LUNSFORD, J. H.: The Catalytic Oxidative Coupling of Methane. In: *Angew. Chem. Int. Ed. Engl.* 34 (1995), Nr. 9, S. 970–980

[205] DRISCOLL, D. J. ; MARTIR, W. ; LUNSFORD, J. X. Wang J. H.: Formation of Gas-Phase Methyl Radicals over Magnesium Oxide. In: *J. Am. Chem. Soc.* 107 (1985), Nr. 1, S. 58–63

[206] FARMER, J. A. ; RUZYCKI, N. ; ZHU, J. F. ; CAMPBELL, C. T.: Lithium Adsorption on MgO(100) and its Defects: Charge Transfer, Structure, and Energetics. In: *Phys. Rev. B* 80 (2009), Nr. 3, S. 035418

[207] FARMER, J. A. ; CAMPBELL, C. T. ; XU, L. ; HENKELMAN, G.: Defect Sites and Their Distributions on MgO(100) by Li and Ca Adsorption Calorimetry. In: *J. Am. Chem. Soc.* 131 (2009), S. 3098

[208] NILIUS, N.: Properties of Oxide Thin Films and Their Adsorption Behavior Studied by Scanning Tunneling Microscopy and Conductance Spectroscopy. In: *Surf. Sci. Rep.* 64 (2009), Nr. 12, S. 595–659

[209] MYRACH, P. ; NILIUS, N. ; LEVCHENKO, S.V. ; GONCHAR, A. ; RISSE, T. ; DINSE, K.-P. ; BOATNER, L.A. ; FRANDSEN, W. ; HORN, R. ; FREUND, H.-J. ; SCHLÖGL, R. ; SCHEFFLER, M.: Temperature-Dependent Morphology, Magnetic and Optical Properties of Li-Doped MgO. In: *Chem.Cat.Chem.* (accepted)

[210] BRENIG, W. ; MENZEL, D.: Desorption Induced by Electronic Transitions, DIET II. Proceedings of the Second International Workshop. (1985)

[211] HALIM, W. S. A. ; SHALABI, A. S.: Surface Morphology and Interaction Between Water and MgO, CaO and SrO Surfaces: Periodic HF and DFT Calculations. In: *Appl. Surf. Sci.* 221 (2004), Nr. 1–4, S. 53–61

[212] LEEUW, N. H. ; WATSON, G .. ; PARKER, S. C.: Atomistic Simulation of the Effect of Dissociative Adsorption of Water on the Surface Structure and Stability of Calcium and Magnesium Oxide. In: *J. Phys. Chem.* 99 (1995), Nr. 47, S. 17219–17225

[213] NODA, K. ; UCHIDA, K. ; TANIFUJI, T. ; NASU, S.: Study of Radiation Damage in Li_2O by Means of Electron-Spin Resonance. In: *Phys. Rev. B* 24 (1981), Nr. 7, S. 3736–3742

[214] JOHNSON, C. E. ; KUMMERER, K. R. ; ROTH, E.: Ceramic Breeder Materials. In: *J. Nuclear Mater.* 155–157 (1988), Nr. Part 1, S. 188–201

[215] NODA, K. ; ISHII, Y. ; OHNO, H. ; WATANABE, H. ; MATSUI, H.: A Study of Tritium Behavior in Lithium-Oxide by Ion Conductivity Measurements. In: *Fusion Eng. Design* 8 (1989), S. 329–333

[216] FARLEY, T. W. D. ; HAYES, W. ; HULL, S. ; WARD, R. ; HUTCHINGS, M. T. ; ALBA, M.: The Dynamic Properties of Lithium Oxide Investigated by Neutron Scattering Techniques. In: *Sol. Stat. Ionics* 28–30 (1988), Nr. Part 1, S. 189 – 193

[217] ISHIIA, Y. ; MORII, Y. ; NICKLOW, R.M. ; FUNAHASHI, S.: Neutron Scattering Study of Lithium Oxide. In: *Physica B: Cond. Mat.* 213 (1995), S. 436–438

[218] NODA, K. ; ISHH, Y. ; MATSUI, H. ; WATANABE, H.: Irradiation Damage in Lithium Oxide. In: *Radiation Effects* 97 (1986), Nr. 3

[219] CHADWICK, A. V.: Electrical Conductivity Measurements of Ionic Solids. In: *Phil. Mag. A* 64 (1991), Nr. 5, S. 983–998

[220] ISHII, Y. ; MURAKAMI, J. ; ITOH, M.: Optical Spectra of Excitons in Lithium Oxide. In: *J. Phys. Soc. Japan* 68 (1999), Nr. 2, S. 696–697

[221] GRISHMANOV, V. ; TANAKA, S. ; YONEOKA, T.: Defect Luminescence in Li_2O Crystal under γ-ray Irradiation. In: *Radiat. Eff.* 143 (1997), Nr. 2, S. 203–211

[222] ASAOKA, Y. ; MORIYAMA, H. ; IWASAKI, K. ; MORITANI, K. ; ITO, Y.: In-situ Luminescence Measurement of Irradiation Defects in Lithium Oxide. In: *J. Nuclear Mater.* 183 (1991), Nr. 3, S. 174–179

[223] UCHIDA, K. ; NODA, K. ; TANIFUJI, T. ; NASU, S. ; KIRIHARA, T. ; KIKUCHI, A.: Optical Absorption Spectra of Neutron-Irradiated Li_2O. In: *phys. stat. sol (a)* 58 (1980), S. 557

[224] ITOH, M. ; MURAKAMI, J. ; ISHII, Y.: Intrinsic Luminescence from Li_2O Crystals Excited in the Exciton-Band Region. In: *phys. stat. sol. (b)* 213 (1999), S. 243

[225] SHLUGER, A. ; ITOH, N.: Models of Electronic Defects and Self-Trapped Excitons in Li_2O. In: *J. Phys.: Cond. Mat.* 2 (1990), S. 4119

[226] ERTL, G. ; KNÖZINGER, H. ; SCHUETH, F. ; WEITKAMP, J.: Handbook of Heterogenous Catalysis, 2nd Edition. In: *Wiley-VCH, Weinheim* (2008)

[227] HARUTA, M. ; TSUBOTA, S. ; KOBAYASHI, T. ; KAGEYAMA, H. ; GENET, M.J. ; DELMON, B.: Low-Temperature Oxidation of CO over Gold Supported on TiO_2, αFe_2O_3 and Co_3O_4. In: *J. Catal.* 114 (1993), Nr. 1, S. 175 – 192

[228] HARUTA, M. ; YAMADAB, N. ; KOBAYASHI, T. ; IIJIMAC, S.: Gold Catalysts Prepared by Coprecipitation for Low-Temperature Oxidation of Hydrogen and of Carbon Monoxide. In: *J. Catal.* 115 (1989), Nr. 2, S. 301 – 309

[229] HENRY, C.R.: Growth of supported Nanoparticles. In: *Surf. Sci.* 80 (2005), Nr. 92

[230] HENRY, C.R.: Morphology of Supported Nanoparticles. In: *Surf. Sci.* 80 (2005), Nr. 92

[231] GOODMAN, D.W.: MODEL CATALYSTS - FROM EXTENDED SINGLE-CRYSTALS TO SUPPORTED PARTICLES. In: *Sur. Rev. Lett.* 2 (1995), Nr. 1, S. 9 – 24

[232] CHATAIN, D. ; RIVOLLET, I. ; EUSTATHOPOULOS, N.: Thermodynamic Adhesion In Nonreactive Liquid Metal-Alumina Systems. In: *J. Chim. Phys. Phys.-Chim. Bio.* 83 (1986), Nr. 9, S. 561 – 567

[233] CHATAIN, D. ; MÉTOIS, J. J.: A New Procedure for the Determination of the Free Energies of Solid-Fluid Interfaces from the Anisotropy of Wetting of a Melt on its Solid. In: *Surf. Sci.* 291 (1993), Nr. 1 – 2, S. 1 – 13

[234] WULFF, G.: On the Question of Speed of Growth and Dissolution of Crystal Surfaces. In: *Zeitschr. Krystallographie u. Mineralogie* 34 (1901), Nr. 5/6, S. 449 – 530

[235] ZINKE-ALLMANG, Martin ; FELDMAN, Leonard C. ; GRABOW, Marcia H.: Clustering on surfaces. In: *Surf. Sci. Rep.* 16 (1992), Nr. 8, S. 377 – 463

[236] VENABLES, J.A. ; SPILLER, G.D.T. ; HANBUCKEN, M.: Nucleation and growth of thin films. In: *Rep. Prog. Phys.* 47 (1984), Nr. 4

[237] WANDER, A. ; BUSH, J. ; HARRISON, N.M.: Stability of rocksalt polar surfaces: An ab initio study of MgO(111) and NiO(111). In: *Phys.Rev. B* 68 (2003)

[238] OVERBURY, S.H. ; BERTRAND, P.A. ; SOMORJAI, G.A.: Surface composition of binary systems. Prediction of surface phase diagrams of solid solutions. In: *Chem. Rev.* 75 (1975), Nr. 5

[239] LIDE, D.R.: CRC Handbook of Chemistry and Physics, 91st Edition. (2010)

[240] NASLUZOV, V.A. ; RIVANENKOV, V.V. ; GORDOENKO, A.B. ; NEYMAN, K.M. ; BIRKENHEUER, U. ; ROSCH, N.: Au Atoms and Dimers on the MgO(100) Surface: A DFT Study of Nucleation at Defects. In: *J. Phys. Chem. B* 109 (2005), Nr. 16, S. 8080 – 8048

[241] NASLUZOV, V.A. ; RIVANENKOV, V.V. ; GORDOENKO, A.B. ; NEYMAN, K.M. ; BIRKENHEUER, U. ; ROSCH, N.: Cluster Embedding in an Elastic Polarizable Enviroment: Density Functional Study of Pd Atoms Adsorbed at Oxygen Vacancies of MgO(001). In: *J. Chem. Phys.* 115 (2001), Nr. 17, S. 8157 – 8171

[242] PACCHIONI, G. ; RÖSCH, N.: Supported Nickel and Copper Clusters on MgO(100): A First-Principles Calculation on the Metal/Oxide Interface. In: *J. Chem. Phys.* 104 (1996), Nr. 18, S. 7329 – 7337

[243] ABBET, S. ; RIEDO, E. ; BRUNE, H. ; HEIZ, U. ; FERRARI, A. M. ; GIORDANO, L. ; PACCHIONI, G.: Identification of Defect Sites on MgO(100) Thin Films by Decoration with Pd Atoms and Studying CO Adsorption Properties. In: *J. Am. Chem. Soc.* 123 (2001), Nr. 25, S. 6172 – 6178

[244] SICOLO, S. ; GIORDANO, L. ; PACCHIONI, G.: Adsorption of Late Transition Metal Atoms on MgO/Mo(100) and MgO/Ag(100) Ultrathin Films: A Comparative DFT Study. In: *J. Phys. Chem. C* 113 (2009), Nr. 38, S. 16694 – 16701

[245] BENEDETTI, S. ; MYRACH, P. ; NILIUS, N. ; VALERI, S. ; FREUND, H.J.: submitted.

[246] STERRER, M. ; HEYDE, M. ; NOVICKI, M. ; NILIUS, N. ; RISSE, T. ; RUST, H.-P. ; PACCHIONI, G. ; FREUND, H.-J.: Identification of Color Centers on MgO(001) Thin Films with Scanning Tunneling Microscopy. In: *J. Phys. Chem. B* 110 (2006), Nr. 1, S. 46 – 49

[247] BENIA, H.M. ; LIN, X. ; GAO, H.-J. ; NILIUS, N. ; FREUND, H.-J.: Nucleation an Growth of Gold on MgO Thin Films. In: *Phys. Chem. C* 111 (2007), Nr. 28, S. 10528 – 10533

[248] REHR, J. J. ; ALBERS, R. C.: Scattering-Matrix Formulation of Curved-Wave Multiple-Scattering Theory: Application to X-ray-Absorption Fine Structure. In: *Phys. Rev. B* 41 (1990), Nr. 12, S. 8139–8149

[249] FERRANDO, R. ; ROSSI, G. ; NITA, F. ; BARCARO, G. ; FORTUNELLI, A.: Interface-Stabilized Phases of Metal-on-Oxide Nanodots. In: *ACS Nano* 2 (2008), Nr. 9, S. 1849 – 1856

[250] SAO-JOAO, S. ; GIORGIO, S. ; MOTTET, C. ; GONIAKOWSKI, J. ; HENRY, C.R.: Interface Structure of Ni Nanoparticles on MgO (100): A Combined HRTEM and Molecular Dynamic Study. In: *Surf. Sci* 600 (2006), Nr. 7, S. 86 – 90

[251] OUAHAB, A. ; MOTTET, C. ; GONIAKOWSKI, J.: Atomistic Simulation of Ag Thin Films on MgO(100) Substrate: A Template Substrate for Heterogeneous Adsorption. In: *Phys. Rev. B* 72 (2005), Nr. 3, S. 035421

[252] FERRANDO, R. ; ROSSI, G. ; LEVI, A. C. ; KUNTOVÁ, Z. ; NITA, F. ; JELEA, A. ; MOTTET, C. ; BARCARO, G. ; FORTUNELLI, A. ; GONIAKOWSKI, J.: Structures of Metal Nanoparticles Adsorbed on MgO(001). I. Ag and Au. In: *J. Chem. Phys.* 130 (2009), S. 174702

[253] PACCHIONI, G.: Ab initio Theory of Point Defects in Oxide Materials: Structure, Properties, Chemical Reactivity. In: *Sol. Stat. Sci.* 2 (2000), Nr. 2, S. 161 – 179

[254] VITTO, A. D. ; PACCHIONI, G. ; DELBECQ, F. ; SAUTET, P.: Au Atoms and Dimers on the MgO(100) Surface: A DFT Study of Nucleation at Defects. In: *J. Phys. Chem B* 109 (2005), Nr. 16, S. 8040 – 8048

[255] LIBUDA, J. ; FREUND, H.-J.: Molecular Beam Experiments on Model Catalysts. In: *Surf. Sci. Rep.* 57 (2005), Nr. 7-8, S. 157 – 298

[256] SKRIVER, H. L. ; ROSENGAARD, N. M.: Surface Energy and Work Function of Elemental Metals. In: *Phys. Rev. B* 46 (1992), Nr. 11, S. 7157–7168

[257] KANTOROVICH, L. N. ; SHLUGER, A. L. ; SUSHKO, P. V. ; GUNSTER, J. ; STRACKE, P. ; GOODMAN, D. W. ; KEMPTER, V.: Mg Clusters on MgO Surfaces: Study of the Nucleation Mechanism with MIES and abinitio Calculations. In: *Faraday Diss.* 114 (1999), Nr. 3, S. 173 – 194

[258] BENIA, H.-M. ; MYRACH, P. ; GONCHAR, A. ; RISSE, T. ; NILIUS, N. ; FREUND, H.-J.: Electron Trapping in Misfit Dislocations of MgO Thin Films. In: *Phys. Rev. B* 81 (2010), Nr. 24, S. 241415

[259] MCKENNA, K. P. ; SHLUGER, A. L.: First-Principles Calculations of Defects Near a Grain Boundary in MgO. In: *Phys. Rev. B* 79 (2009), Nr. 22, S. 224116

[260] Optical Data from Sopra SA. In: *http://www.sspectra.com*

[261] NILIUS, N. ; ERNST, N. ; FREUND, H.-J.: Photon Emission Spectroscopy of Individual Oxide-Supported Silver Clusters in a Scanning Tunneling Microscope. In: *Phys. Rev. Lett.* 84 (2000), Nr. 17, S. 3994 – 3997

[262] ZHU, J. ; FARMER, J. A. ; RUZYCKI, N. ; XU, L. ; CAMPBELL, C. T. ; HENKELMAN, G.: Calcium Adsorption on MgO(100): Energetics, Structure, and Role of Defects. In: *J. Am. Chem. Soc.* 130 (2008), Nr. 7, S. 2314 – 2322

[263] BENIA, H.-M. ; NILIUS, N. ; FREUND, H.-J.: Photon Mapping of MgO Thin Films with an STM. In: *Surf. Sci.* 601 (2007), Nr. 10, S. L55 – L58

[264] MARKEL, V. A. ; SHALAEV, V. M. ; ZHANG, P. ; HUYNH, W. ; TAY, L. ; HASLETT, T. L. ; MOSKOVITS, M.: Near-field Optical Spectroscopy of Individual Surface-Plasmon Modes in Colloid Clusters. In: *Phys. Rev. B* 59 (1999), Nr. 16, S. 10903–10909

[265] OSHIMA, C. ; AIZAWA, T. ; SOUDA, R. ; ISHIZAWA, Y.: Microscopic surface phonons of MgO(100) surface. In: *Sol. Stat. Comm.* 73 (1990), Nr. 10, S. 731 – 734

[266] MOSKOVITS, M.: Surface-Enhanced Spectroscopy. In: *Rev. Mod. Phys.* 57 (1985), Nr. 3, S. 783–826

[267] XU, H. ; BJERNELD, E. J. ; KÄLL, M. ; BÖRJESSON, L.: Spectroscopy of Single Hemoglobin Molecules by Surface Enhanced Raman Scattering. In: *Phys. Rev. Lett.* 83 (1999), Nr. 21, S. 4357–4360

[268] XU, H. ; AIZPURUA, J. ; KÄLL, M. ; APELL, P.: Electromagnetic Contributions to Single-Molecule Sensitivity in Surface-Enhanced Raman Scattering. In: *Phys. Rev. E* 62 (2000), Nr. 3, S. 4318–4324

[269] HILLENBRAND, R. ; KEILMANN, F.: Optical Oscillation Modes of Plasmon Particles Observed in Direct Space by Phase-Contrast Near-Field Microscopy. In: *Appl. Phys. B* 73 (2001), S. 239 –243

Publications and Conference Contributions

Publications

S. Benedetti, N. Nilius, P. Myrach, Ilaria Valenti, H.-J. Freund, S. Valeri. Spontaneous Oxidation of Mg Atoms at defect Sites in an MgO Surface. *J. Phys. Chem. Lett.* submitted (2010)

P. Myrach, N. Nilius, S.V. Levchenko, A. Gonchar, T. Risse, K.-P. Dinse, L.A. Boatner, W. Frandsen, R. Horn, H.-J. Freund, R. Schlögl, M. Scheffler. Temperature-Dependent Morphology, Magnetic and Optical Properties of Li-Doped MgO. *Chem Cat Chem* **2**:7, 854–862 (2010)

H.-M. Benia, P. Myrach, A. Gonchar, T. Risse, N. Nilius, H.-J. Freund. Electron trapping in misfit dislocations of MgO thin films. *Phys. Rev. B* **81**:24, 241415 (2010)

X. Lin, B. Yang, H.-M. Benia, P. Myrach, M. Yulikov, A. Aumer, M.A. Brown, M. Sterrer, O. Bondarchuk, E. Kieseritzky, J. Rocker, T. Risse, H.-J. Gao, N. Nilius, H.-J. Freund. Charge-Mediated Adsorption Behavior of CO on MgO-Supported Au Clusters. *J. Am. Chem. Soc* **132**:22, 7745–7749 (2010)

H.-M. Benia, P. Myrach, N. Nilius, H.-J. Freund. Structural and electronic characterization of the MgO/Mo(001) interface using STM. *Surf. Sci* **604**:3–4, 435–441 (2010)

P. Myrach, N. Nilius, H.-J. Freund. Alkaline Earth versus Noble Metal Particles on MgO Thin Films: Growth and Optical Properties. *J. Phys. Chem. C* **113**:43, 18740–18745 (2009)

H.-J. Benia, P. Myrach, N. Nilius. Photon emission spectroscopy of thin MgO films with the STM: from a tip-mediated to an intrinsic emission characteristic. *New J. Phys.* **10**, 013010 (2008)

Conference Contributions

Polarity healing at the local scale: MgO on Au(111). P. Myrach, N. Nilius, S. Benedetti, H.-J. Freund. Frühjahrstagung der Deutschen Physikalischen Gesellschaft, 21.–26.Mar. 2010, Regensburg, Germany.

Light emission spectroscopy with the STM on noble and alkaline-earth metal particles on MgO thin films. P. Myrach, N. Nilius, H.-J. Freund. Nanostructures at Surfaces: International Conference, 20.–25.Sep. 2009, Ascona, Switzerland.

Optical properties of single alkali-earth particles on MgO films. P. Myrach, N. Nilius, H.-J. Freund. Frühjahrstagung der Deutschen Physikalischen Gesellschaft, 22.–27.Mar. 2009, Dresden, Germany.

Optical properties of single Mg particles on MgO thin films. P. Myrach, H.-M. Benia, N. Nilius, H.-J. Freund. Frühjahrstagung der Deutschen Physikalischen Gesellschaft, 25.–29.Feb. 2008, Berlin, Germany.

Curriculum Vitae

Name		Myrach
Vorname		Philipp
Anschrift		Wotanstr. 13 10365 Berlin
Geburtsdatum		29. 10. 1980
Geburtsort		Greifswald
Staatsangehörigkeit		deutsch
Schulbildung	09.1987-07.1991	Gerhart Eisler Oberschule
	09.1991-06.1999	Europaschule Deutsch-Polnisches Gymnasium Löcknitz
	07.1999	Abitur
Studium	10.2000-09.2006	Studium der Physik (Technische Universität Berlin)
	09.2006	Diplom Physiker Titel: *Dipl. Phys.*
	seit 10.2006	Promotion am Fritz-Haber Institut der Max-Planck Gesellschaft in Berlin Betreuung durch Herrn Prof. Dr. H.-J. Freund und Herrn Dr. Niklas Nilius

Danksagung

Selbstständigkeitserklärung

Hiermit erkläre ich, die vorliegende Arbeit selbstständig ohne fremde Hilfe verfasst und nur die angegebene Literatur und Hilfsmittel verwendet zu haben.

Berlin, den

Philipp Myrach